EFFECTIVE FIELD THEORY OF NUCLEAR FORCES AND THE DEUTERON

A thesis submitted to the University of Manchester
for the degree of Doctor of Philosophy
in the Faculty of Engineering and Physical Sciences

2016

By
Katharine Louise Ipson
School of Physics and Astronomy

Contents

Word Count: Insert number here

List of Tables

List of Figures

Abstract

Effective theories have applications in many areas of physics, from Newtonian mechanics through to condensed matter physics. In this thesis we discuss effective field theories in the context of constructing nucleon-nucleon interactions in a systematic and model-independent way.

We start with the examination of the spin-singlet P-wave, by using distorted-wave methods to remove the effects of long-range pion-exchange forces from the empirical ${}^1P_1$ phase shift. The divergence appearing in this channel is renormalised using a counterterm that is provided by the relevant (Weinberg) power counting. This leaves an effective interaction strength that can be analysed, and from which one can extract an approximate scale for the underlying physics. We determine this scale to be close to the Δ-resonance.

We then turn to coupled (spin-triplet) waves, focussing predominantly on the ${}^3S_1 - {}^3D_1$ wave that contains the deuteron - an important system to understand in the context of nuclear forces. Starting with the ${}^3S_1 - {}^3D_1$ scattered waves, we again remove long-range pion-exchange forces from the empirical phase shifts, and extract an effective interaction matrix. The element that suffers from a divergence can be renormalised using counterterms provided by a renormalisation group analysis. Switching to negative energies we look for the deuteron bound state, which is loosely bound and so pion physics plays an important role. Using the counterterms provided at positive energies, we extrapolate to the bound state and treat this, two-pion-exchange and recoil one-pion-exchange as a combined perturbation to the system. We then use perturbation theory techniques to calculate the first-order correction to the energy and wave function, from which we calculate some deuteron observables.

Declaration

No portion of the work referred to in this thesis has been submitted in support of an application for another degree or qualification of this or any other university or other institute of learning.

Copyright

Acknowledgements

First and foremost I would like to extend special thanks to my supervisor Prof. Mike Birse for his continued support and guidance throughout my PhD studies. I would also like to thank Dr Judith McGovern for her support at times when I needed it. I would like to thank them both for making my short stay in Seattle in my first year an enjoyable one and taking me around the city and up Mt Si.

I would also like to thank K. Helmke for her collaboration on part of the work described in Chapter 3.

Last but not least I would like to thank my parents and my fiancé James who's unwavering belief in me has helped me through the tough times.

Publications

K. L. Ipson, K. Helmke and M. C. Birse, "Effective short-range interaction for spin-singlet P-wave nucleon-nucleon scattering", Phys. Rev. C. **83** (2011)

Chapter 1

Introduction

Understanding the nature of nuclear forces, and in particular how nucleons, the collective term for neutrons and protons, bind together to form nuclei, is a long standing problem in nuclear physics. Huge progress has been made, however, since the early 1930s, when the correct composition of the nucleus was first established, after the discovery of the neutron by Chadwick in 1932 [1]. It is a testament to how complicated this area of research is that even the simplest question of how two nucleons interact is still being actively researched today.

Experimental observations over the years have revealed the various properties of the nuclear force, which we will list here (see e.g. Ref. [2] for further details). Firstly, the nuclear force is short-ranged, acting over distances of a few fm (10^{-15} m), which means that each nucleon only interacts with those in its immediate vicinity. This leads to the saturation of the nuclear force, which can be seen in binding-energy data. It is also strongly attractive at 'intermediate' distances, overcoming the coulomb repulsion that occurs between the protons, becoming strongly repulsive at 'short' distances (< 0.5 fm).

The nuclear force exhibits charge symmetry to a good approximation, implying that the force between two neutrons is the same as that between two protons, after, of course, having made corrections for the Coulomb force. This can be seen for instance in the properties of 'mirror' nuclei, and the values of nn and pp scattering lengths.

Charge independence, which implies that neutron-neutron, proton-proton, and neutron-proton forces are the same (after accounting for the Coulomb force), is not quite as well realised, as can be seen when comparing the np to nn and pp

scattering lengths.

The nuclear force is strongly spin-dependent. Evidence for this is that the deuteron (a bound state consisting of a single neutron and proton whose spins are aligned in parallel) is in a spin-triplet state, whereas no corresponding spin-singlet bound state has been observed.

There is also a spin-orbital dependence. This is supported by observations made in scattering experiments, in which one can produce beams of polarized nucleons in certain directions when scattering unpolarized nucleons at a target.

Lastly, but not least, the nuclear force has a tensor component. This is evident from the non-zero value of the electric quadrupole moment of the deuteron, implying that it is not quite spherically symmetric, which in turn is due to the admixture of a D-state component.

Apart from wanting to learn about the various characteristics exhibited by the nuclear force, researchers have also wished to understand the mechanisms that are responsible for them.

The seminal work of Yukawa in 1935 provided the first important and successful insight [3]. In his work Yukawa hypothesised that the nuclear force is mediated by the exchange of a massive particle, and thus by doing so predicted the existence of the pion.

Soon after the discovery of the pion in 1947, attempts were made to calculate two-pion exchange contributions to the nuclear force [4] [5] [6]. However, these could not produce the strength required for the spin-orbit force.

Fortunately, the situation was improved by the experimental discovery of heavy mesons in the 1960s. This inspired the construction of the one-boson exchange (OBE) models, in which different bosons are used to recreate the various characteristics of the nuclear force (see e.g. Ref. [7]). Although these models could fit the NN scattering data available at the time well, they relied on the σ-boson to create the intermediate-range attraction, which has not been observed experimentally.

Therefore, renewed effort was taken to derive the two-pion exchange part of the force (which creates this attraction) in new ways. Dispersion theory, for instance, was used by the Stony Brook [8] [9] and Paris groups [10] [11], whilst the Bonn group, for example, used field theory techniques [12].

The development of the modern high-quality phenomenological potentials in

the 1990s, was the culmination of all the hard effort over the years [1]. Examples of these include, the Nijm-I, Nijm-II and Reid93 potentials of the Nijmegen group [14], the CD-Bonn potential of the Bonn group [15], and the V_{18} potential of the Argonne group [16]. Using between 40 and 50 parameters, they all fit the NN data up to $T_{\rm lab} = 350$ MeV [17] with close to the optimal $\chi^2/N_{\rm data} = 1$. Therefore, in that sense the aim to provide a reliable input for use in calculations of few- and many-body systems has been realised.

The story does not end here, however, as these kinds of potentials do have some shortcomings. One such shortcoming, is that they do not provide a systematically improvable approach to the derivation of nuclear forces; it is hard to know which contributions are dominant over others. Also, the approach does not lend itself well to determining many-body forces consistently, or to calculate observables for processes involving electroweak probes. Furthermore, although they all include the required long-distance contribution due to one-pion exchange, for the intermediate- and short-distance regions they use different mechanisms to produce the same physical effects. This is less of a problem in the short-distance region, however, as low-energy observables are not able to probe the details of the short-distance (high-energy) physics there, so it is not crucial what kinds of forms are used to parametrise this region. Finally, as we know today that the interactions between nucleons are actually "residual" interactions governed by Quantum Chromodynamics (QCD), the theory of quarks and gluons, the fact that the potential models do not provide a clear connection to QCD is therefore also not ideal. Fortunately, the tools of effective field theories (EFTs) are able to provide an alternative way of solving these issues.

EFTs are approximate, systematically improvable, theories that are used to describe dynamics at low-energy scales in a model-independent way. Central to their effectiveness is the existence of a separation of scales between the low-energy physics of interest and the underlying or high-energy physics. This is because it allows one to expand the theory perturbatively, using the ratio of low- to high-energy scales as the expansion parameter. At low energies (as mentioned in the previous paragraph) observables simply do not resolve the details of the high-energy physics. This physics is parametrised in terms of contact interactions (it is 'integrated' out), whose corresponding values are initially unknown and have to

[1] For a more thorough description of the history of deriving NN potentials in the phenomenological approach see e.g. Refs. [12] and [13].

be obtained by fitting them to data (that is if the high-energy theory is unknown or too complicated to be solved).

As a quick aside, an early successful application of this kind of idea, that is relevant to the discussion of nuclear forces, is the 'effective range theory' (ERT) developed in the late 1940s to describe low-energy ($<\sim$ 10 MeV) NN scattering [18] [19]. The key idea is that at low enough energies only two parameters, the scattering length a, and the effective range r, as given by the following equation

$$k \cot \delta \approx -\frac{1}{a} + \frac{1}{2} r_0 k^2 \tag{1.1}$$

are needed to describe the (S-wave) scattering, and any suitable potential can be used to obtain them because the detailed shape of the potential is unimportant. The terms in the effective-range expansion (Eq. (1.1)) in fact have a one-to-one correspondence with terms in the so-called 'pionless' EFT.

To build an EFT one starts by writing down the most general Lagrangian (or Hamiltonian) that contains all the low energy degrees of freedom relevant to the system (note that identifying these is not always trivial), and whose interaction terms are governed by the same symmetry principles as the underlying theory. In this way the EFT can be regarded as a true low-energy limit of the underlying theory, so has a very clear connection to it. Unfortunately, this produces an infinite number of terms, and therefore to be practical (and renormalisable) one needs a systematic way of ordering them by their importance. To do this, one relies on the concept of counting powers of low-energy scales, known as "power counting". The series can then be organised and truncated to any given order. This produces a systematically improvable theory, more terms can always be added to achieve the desired accuracy. Also, as mentioned, EFTs are low energy theories, they are only expected be valid up to a certain energy or breakdown scale, at which point they would start to resolve the details of the high-energy of underlying physics. This is determined by the lowest scale not explicitly included in the theory.

Weinberg was the first to consider these ideas in the context of low-energy QCD [20]. His work was further developed by Gasser and Leutwyler [21] [22] producing Chiral Perturbation Theory (ChPT)[2], the effective field theory of QCD.

ChPT describes the interactions between pions and other particles, such as nucleons and photons (and other pions of course). These interactions are governed

[2]See e.g. Ref. [23] for a pedagogical introduction.

by the symmetries of the high-energy theory - QCD. The most important of which for pionic interactions is the spontaneously broken (approximate) chiral symmetry.

In the limit of massless quarks chiral symmetry is an exact symmetry. It means that the corresponding QCD Lagrangian is invariant under independent global unitary transformations of the left- and right-handed quark fields, i.e. invariant under the transformations $\psi_L \to U_L\psi_L$ and $\psi_R \to U_R\psi_R$, where $\psi = (u, d)$.

The fact that it is spontaneously broken[3] means that although it is a symmetry of the Lagrangian, as just mentioned, it is not a symmetry of the ground state. Invoking Goldstone's theorem [24] [25] implies the existence of massless Goldstone bosons for each broken generator, these are the pions. This explains why the pions are so light compared to typical hadronic scales $\sim$ 1 GeV. In ChPT therefore, the low-energy scales are given by momenta and the pion masses, ... (generically denoted Q), and the high-energy scales are given by mass of the ρ meson, the mass of the nucleon, and the factor $4\pi F_\pi$,... (denoted Λ_0) and the expansion parameter is then Q/Λ_0. The fact that the pions have mass in the real world is because the symmetry is explicitly broken due to the quark masses. However, because the quark masses are small means it still is a good approximate symmetry.

The terms in the theory are organised according to naive dimensional analysis (NDA), also known as "Weinberg power counting", which just involves counting powers of low-energy scales. ChPT works as a perturbative theory (in the meson-only and single-baryon sectors) because as the pions are Goldstone bosons, they interact weakly at low energies.

Nucleons on the other hand, interact strongly at low energies, they are not suppressed in the chiral limit ($m_\pi = 0$). This is evident from the existence of low energy bound states (such as the deuteron) and resonances, implying that it is a nonperturbative regime, and therefore perturbation theory will fail. Nevertheless the tools of chiral perturbation theory can still be used to derive nuclear forces, as is discussed in the next chapter.

Organsiation of the thesis

[3]Evidence for this is the absence of parity doublets in the hadronic spectrum.

The thesis is organised as follows. In chapter 2 we discuss some of the various effective field theory approaches used to derive nuclear forces in a model-independent and systematic way. We emphasise that there are still areas of disagreement in the field, particularly with regards to which terms should be iterated to all orders, what value the cutoff should take and the power counting that should be used for the terms in the short-distance effective interaction needed to produce renormalised, regulator-independent, results.

In chapter 3 we demonstrate the "deconstruction" method used to extract an effective residual interaction from empirical phase shifts. It is applied to NN scattering in the uncoupled channels, with the main focus on the ${}^1P_1$ channel. From the residual interaction we are able to estimate a scale for the underlying physics. In the same chapter we also discuss the method applied to the uncoupled spin-triplet channels, as a means of bridging the gap between the work in this chapter and the next.

In chapter 4 we show how the method can be adapted to "deconstruct" phase shifts in the coupled channels in order to extract a residual interaction matrix in the same spirit as for the uncoupled channels. We mainly focus on the ${}^3S_1 - {}^3D_1$ channels as they contain the deuteron, but we also present results for the ${}^3P_2 - {}^3F_2$ channels.

In chapter 5 we switch to negative energies and calculate the deuteron bound state wave functions, which are then used to further calculate various deuteron observables.

Finally, in chapter 6 we present the conclusions of the work and scope for future work.

A Note about Notations

In uncoupled channels we use u to denote the reduced radial wave function (i.e. $\psi = u/r$). It is a function of both coordinate space (r) and asymptotic momentum (p), i.e. $u = u(p, r)$, unless otherwise stated. In coupled channels we use u to denote the wave with orbital angular momentum $L = J - 1$ and w to denote the wave with $L = J + 1$. Again u and w depend on both r and p, but space constraints mean we may not write the arguments down explicitly. Phase shifts are denoted generically using the δ symbol (which is also used for the dirac-delta function) and are only dependent on p. Again the argument will

usually not be written down explicitly.

We use natural units, i.e. $\hbar = c = 1$.

Partial waves are labelled using the spectroscopic notation: ${}^{2S+1}L_J$, where S is the total Spin of the neutron-proton system, L is the total orbital angular momentum and J is the total angular momentum.

Chapter 2

Nuclear Effective Field Theories

The forces between nucleons result from residual strong interactions of QCD, the theory of quarks and gluons. Although the underlying theory - QCD - is therefore known, it is unfortunately far too complicated in the non-perturbative regime of nuclear physics to calculate nuclear forces, or properties directly from the QCD Lagrangian. While Lattice QCD is revealing promising results, it has its limitations such as requiring intensive computing power. A useful alternative is to use effective field theory[1].

Weinberg was the first to suggest that the tools of effective field theory (specifically chiral perturbation theory) could be used to derive nuclear forces [29] [30]. In this approach the nucleon-nucleon (NN) potential is defined as the sum of two-nucleon irreducible (time-ordered) diagrams. This produces an infinite number of diagrams, so to be practical they have to be ordered according to their importance, which is done using naive dimensional analysis (NDA). As a result only a finite number of diagrams will contribute to the potential at a given order. For example, taking the simplest case, at leading-order the NN potential is given by static one-pion-exchange (OPE) and energy-independent contact interactions,

$$V(\vec{q}) = -\left(\frac{g_A}{2F_\pi}\right)^2 \frac{\vec{\sigma}_1 \cdot \vec{q}\,\vec{\sigma}_2 \cdot \vec{q}}{\vec{q}^{\,2} + m_\pi^2} \boldsymbol{\tau}_1 \cdot \boldsymbol{\tau}_2 + C_S + C_T\, \vec{\sigma}_1 \cdot \vec{\sigma}_2, \tag{2.1}$$

where $\vec{q}$ denotes the nucleon momentum transfer, g_A and F_π are the nucleon axial coupling and pion decay constants, respectively, m_π is the pion mass, $\vec{\sigma}$ and $\vec{\tau}$ are the spin and isospin Pauli matrices, respectively, and $C_{S,T}$ are the low-energy-constants (LECs) corresponding to the leading, energy-independent

[1]Review articles on nuclear effective field theories include [26], [27] and [28].

contact interactions. The terms in Eq. (2.1) are generated from the lowest-order effective chiral Lagrangian, given by

$$\mathcal{L}^{(0)} = \frac{1}{2}\partial_\mu \boldsymbol{\pi}\cdot\partial^\mu\boldsymbol{\pi} - \frac{1}{2}m_\pi^2\boldsymbol{\pi}^2 + N^\dagger\left[i\partial_0\frac{g_A}{2F_\pi}\boldsymbol{\tau}\vec{\sigma}\cdot\vec{\nabla}\boldsymbol{\pi} - \frac{1}{4F_\pi^2}\boldsymbol{\tau}\cdot(\boldsymbol{\pi}\times\partial_0\boldsymbol{\pi})\right]N$$
$$-\frac{1}{2}C_S(N^\dagger N)(N^\dagger N) - \frac{1}{2}C_T(N^\dagger\vec{\sigma}N)(N^\dagger\vec{\sigma}N) + \ldots \tag{2.2}$$

where $\boldsymbol{\pi}$ and N are the pion and nucleon field operators, respectively. Note that this Lagrangian is written in the non-relativistic 'heavy-baryon' formalism, where nucleons are treated as static sources.

Ordonez et. al. were the first to use the time-ordered perturbation theory approach to derive an energy-dependent NN potential up to chiral order-Q^3, or equivalently to next-to-next-to-leading-order ($\mathrm{N^2LO}$), and further use the potential to analyse NN scattering [31] [32] [33]. Epelbaum et. al. used the method of unitary transformation to derive an equivalent energy-independent NN potential [34] [35] (see also Ref. [36]). Kaiser et. al. used an S-matrix approach to calculate the NN potential [37] (see also Ref. [38] where the Delta-resonance is included as an explicit degree of freedom). Further work has resulted in order-Q^4 ($\mathrm{N^3LO}$) potentials [39] [40] [41] [42] [43], order-Q^5 ($\mathrm{N^4LO}$) potentials [44] [45], and even contributions to the order-Q^6 ($\mathrm{N^5LO}$) NN potentials have been calculated [46].

Irrespective of how the NN potentials are constructed, in Weinberg's approach, to generate the necessary non-perturbative effects associated with nuclear forces (characterised by bound states and large scattering lengths), and to obtain scattering amplitudes, the (truncated) NN potential is iterated to all orders by inserting it into a dynamical equation, such as the Lippmann-Schwinger or Scrödinger.

This approach is undoubtedly successful, for example, in reproducing NN phase shifts (see e.g. Refs. [42], [41], [44] and [46]), and can be straightforwardly used in few- and many-body calculations, which rely on inserting a potential into a Scrödinger equation (see e.g. the review articles [28] and [47], and references therein). However, there are formal issues with this approach, which have led to much debate, see e.g. Refs. [48], [49] and [50].

One such issue is that the leading terms in the potential, OPE and the energy-independent contact interactions (see Eq. (2.1)) are both formally of order Q^0 in Weinberg counting (NDA). Although Weinberg discussed that non-relativistic loop diagrams for NN scattering are enhanced to order Q, compared to Q^2 for

relativistic loop diagrams, it still means that OPE and the contact interactions are perturbative (each extra loop in the iteration leads to an extra power of Q which is not cancelled). Therefore one needs to find low-energy scales in the NN system that promote these potentials from order Q^0 to Q^{-1}, to justify iterating them.

The scales which justify iterating the contact interactions in Eq. (2.1), are the S-wave scattering lengths, which are unnaturally large compared to the range of the nuclear potential, with $a_S \approx -23.7$ fm, and $a_T \approx 5.42$ fm ([51] [52] [53] [54] [55]). At low-energies, where pion-exchange cannot be resolved (meaning that the only degrees of freedom present are the nucleons) this treatment leads to the 'pionless' EFT, which is an expansion about the limit of infinite scattering length. It is a field-theoretic version of the effective-range-expansion (ERE). Advantages of the EFT approach over the ERE include that one can extend it to use in e.g. three-body processes (see e.g. [56] and [57]), it can be used to calculate processes systematically involving external probes (e.g. the relevant sections in the review articles of Refs. [26] and [27]), it can also be used in other areas of physics which involve unnaturally large scattering lengths, such as ultracold atoms (e.g [58] and [59]).

The question of whether pions should be treated perturbatively or not can now be addressed. Kaplan, Savage and Wise [54], [55] developed an approach that essentially extends the pionless EFT to include pions perturbatively. This approach has the advantage that scattering amplitudes can be calculated analytically, it is also consistent with chiral perturbation theory. Unfortunately it has been shown to suffer from poor convergence in the lower L channels, especially so in the ${}^3S_1$ channel [60] [61] [62] [63]. However, a perturbative treatment of pions does seem justified in partial waves with large orbital angular momentum, where OPE scattering is weak. See also Ref.[64] in which a modified KSW scheme has been presented demonstrating improved convergence [64].

The problem with the convergence can be traced to the identification of a scale in the strength of the OPE potential [65], given by

$$\lambda_{NN} = \frac{16\pi F_\pi^2}{g_A^2 M_N} \approx 290\text{MeV}. \tag{2.3}$$

This scale, whilst built out of high-energy scales, implying that to be consistent with chiral perturbation theory it should be taken as a high-energy scale itself (as done in KSW counting), is numerically small, only about $2m_\pi$. Therefore,

to improve convergence, one can choose to identify λ_{NN} as a low-energy scale, implying that OPE should be iterated. The main downside of this is that the strict connection with chiral perturbation theory is now lost.

This brings us full-circle back to Weinberg's approach. By iterating the full potential, divergences are generated at orders where there are no counterterms available to renormalise. The success of this approach, therefore, relies on keeping the cut-off finite and low (500 MeV)[2]. Also, by going to higher-orders in the NN potential, it ensures that more counterterms are available for use when renormalising. The questions of whether or not one needs to go to such higher orders, whether or not important/enhanced counterterms are being omitted, and whether the method is consistent, should be fully considered.

In Ref. [68] Nogga, Timmermans and van Kolck (NTvK) analysed the cut-off dependence (Λ range: 2 - 20 fm^{-1}) of phase shifts in various channels at leading-order (LO) in Weinberg's approach (i.e. with iterated OPE and contact interactions that scale as Q^{2L}). They that found Weinberg's power counting is consistent in spin-singlet channels (where no tensor component of OPE is present) and in spin-triplet channels where the tensor OPE force is repulsive. Regarding the attractive spin-triplet channels, they found strong cutoff dependences that could not be removed by the contact terms provided by Weinberg, which appear at orders Q^2 in the p-waves and Q^4 in the d-waves, so concluded that Weinberg's power counting is not consistent in these channels. They were able to remove the cutoff dependence, however, by the inclusion of an extra counterterm in each channel. They also recognised that for certain channels (they demonstrated the case of $^3D_2$) a particular value (or small range) of Λ could be found that described the low-energy data equally well without the need for promoted counterterms. The work of NTvK has been criticised however, see e.g. Ref. [67].

Although Weinberg's seminal papers were published over 20 years ago, there still remains disagreement within the field today over certain aspects of nuclear EFTs. These disagreements are predominantly about the power counting of the short-distance interactions, i.e. the number of counterterms required for renormalisation, what value of cutoff to use, and the treatment of higher-order pion-exchange terms, i.e. should the whole potential be iterated to all orders or not.

The Wilsonian renormalisation group (RG) [69] can be used to help resolve

[2]This is not taken to be problematic by some researchers, in fact the opposite, they advocate the use of low cut-offs [66] [67].

the first point. It is a tool that can be used specifically to determine the power counting of the terms in the effective short-range potential subject to the influence of known long-range potentials.

Developed in Manchester, the general method proceeds via the following steps:

- (i) Identify all relevant low-energy scales for the problem, particularly ones that promote terms from leading-order to Q^{-1}, since these terms should be iterated.
- (ii) Apply a floating cutoff (Λ) to the theory[3] at a scale that is less than the underlying physics Λ_0 but above the low-lying physics of interest Q, i.e. $Q < \Lambda < \Lambda_0$.
- (iii) Rescale the theory by writing all quantities with dimensions in units of Λ.
- (iv) Follow the evolution of the theory as Λ is lowered to $\Lambda \to 0$ and demand that the physics (or more specifically physical observables) is independent of Λ. Look for fixed points of the theory - described by scale-free systems.
- (v) Expand the EFT around the fixed points in powers of Λ, to obtain the power counting for the theory.

This method was first used to analyse the scale dependence of NN scattering with short-range forces only [70] [71] [72] [73]. This is relevant to low-energy NN scattering by contact forces, i.e. where pion-exchange forces are not resolved. Two fixed points were found. The first, called the trivial fixed point, is suitable for systems with weak scattering, and whose power counting matches that of Weinberg power counting. The second, called the nontrivial fixed point describes a system with a bound state at zero energy, or infinite scattering length, and whose power counting matches that of the KSW counting, with terms in a one-to-one correspondence with that of the effective-range-expansion.

The RG analysis has been further used to analyse the scale dependence of NN scattering in the presence of long-range forces. These include the Coulomb, Yukawa (central OPE) and repulsive inverse-square forces analysed in Refs. [74] and [75], the attractive inverse-square force analysed in Ref. [76] (relevant for three-body scattering), and the tensor OPE force analysed in Ref. [65][4]. Note

[3]For systems in the presence of known long-range forces this should be done in the basis of the distorted waves.

[4]Other useful references include [77], [48] and [78].

that the scaling behaviour of a short-distance interactions obtained in these analyses, and therefore their power counting, is determined by the power-law form of the wave functions near the origin, which in turn is governed by the singularity of the long-distance potentials.

As for the case of scattering involving purely short-range forces, two fixed points (trivial and nontrivial) were also found in the RG analyses of NN scattering in the presence of long-range forces.

In spin-singlet channels, only the central part of OPE is present, which has a singularity proportional to $1/r$ at the origin. Even when iterated central OPE is not strong enough to change the forms of the wave functions near the origin, these are governed by the centrifugal potential. Therefore for waves with $L \geq 1$, i.e. where the scattering is weak, the appropriate fixed point to expand around is the trivial fixed point, and so the power counting for the effective short-range interactions is that of Weinberg power counting, i.e. Q^{2L}. On the other hand, scattering in the ${}^1S_0$ channel is strong, therefore it is more appropriate to expand about the non-trivial fixed point, and therefore the power counting corresponds to a modified version of KSW.

In the spin-triplet waves, it is the $1/r^3$ singularity of tensor OPE that governs the forms of the wave functions near the origin, with (power-law) form proportional to $r^{-1/4}$ for both attractive and repulsive waves, resulting in very different power counting. The RG analysis in the spin-triplet waves [65] explains and extends the findings of NtvK in Ref. [68].

The results of the RG analyses are shown in Table 2.1, for terms up to order Q^3. Note that there are certain counterterms present (i.e. that have been promoted) that would otherwise not be there if we were using Weinberg power counting. Another important point to note, is that the power counting in the spin-triplet channels depends on the energies one is concerned with. This is exemplified in Table 2.2, which shows the critical values for the relative momenta, above which the waves penetrate the centrifugal barrier and probe the region dominated by tensor OPE. Above these momenta, OPE must be treated non-perturbatively[5]. Therefore, Weinberg power counting is expected to hold for the higher partial waves ($L \geq 3$), for the energies we are interested in.

Being able to determine the power counting of the short-distance interactions

[5]Note that the critical values for the uncoupled partial waves, were first calculated by Gao [79].

Order	
Q^{-1}	${}^1S_0$, ${}^3S_1$ C_0's , LO OPE
$Q^{-1/2}$	${}^3P_J$, ${}^3D_J$ C_0's
Q^0	${}^1S_0$ C_2
$Q^{1/2}$	${}^3S_1$ C_2
$Q^{3/2}$	${}^3P_J$, ${}^3D_J$ C_2's
Q^2	${}^1S_0$ C_4, ${}^1P_1$ C_0, NLO OPE, LO TPE
$Q^{5/2}$	${}^3S_1$ C_4
Q^3	NLO TPE

Table 2.1: "Orders of terms in the two-nucleon effective potentials for waves with $L \leq 2$. The leading coefficient in each interaction is labelled by the subscript 0, a subleading one (with one power of the energy or two derivatives) by the subscript 2, and so on." [48].

Channel	p_c / MeV
${}^3S_1 - {}^3D_1$	66, 240
${}^3P_0$	182
${}^3P_1$	365
${}^3P_2 - {}^3F_2$	470, 2010
${}^3D_2$	403
${}^3D_3 - {}^3G_3$	382, 1390
${}^3F_3$	2860
${}^3F_4 - {}^3H_4$	2330, 6730
${}^3G_4$	1870

Table 2.2: "Critical values for the relative momentum at which pairs of eigenvalues become degenerate and hence the tensor potential cannot be treated perturbatively." [65].

is essential. This is because, apart from parametrising the high-energy physics not explicitly included in the theory, they also act as counterterms to remove the dependence on regulators employed to control divergences.

The power counting results of the RG analyses are of course theoretical, therefore they need to be tested. We do not, however, follow the standard nuclear EFT practice, which assumes in advance a low-order polynomial in p^2 and then obtains the coefficients by fitting them to phase shifts. Instead we extract effective short-distance interactions directly from phase shifts using the "deconstruction" approach. The advantage of this is that we are able to see more clearly in which energy range a polynomial form might be valid. It also makes clear where the

different Nijmegen partial-wave analyses are in agreement with each other, and where they are not reliable.

This approach was first developed by Birse and McGovern in an analysis of NN scattering in the peripheral ($L \geq 2$) spin-singlet channels in Ref. [80]. The method was then extended and used to analyse NN scattering in the uncoupled spin-triplet channels [81], the $^1S_0$ channel [82], and the $^1P_1$ channel [83] (the subject of the next chapter).

The basic idea in these analyses is to use distorted-wave methods to remove the effects of known long-range forces (up to order-Q^3) from empirical phase shifts, leaving behind an effective short-range interaction (with long-range forces that start at order-Q^4). If the resulting interactions display a strong energy-dependence, then it implies that other long-range forces, that have not been accounted for, are present. Short-range forces, on the other hand, lead to smooth energy-dependences that can be expanded in a polynomial form.

Employed in all Refs. [80], [81], [82], and [83], was a radial cut-off of $R_0 = 0.1$ fm. Such a value is obviously well beyond the breakdown scale expected of the EFT. It is used, however, to minimise the artefacts of the cut-off (terms proportional to positive powers of R_0). Therefore it allows us to quantitatively estimate the strength of the missing physics. We are only allowed to do this (as emphasised in Ref. [48]) if the pre-determined power counting is adhered to, i.e. we only iterate "relevant" terms (of order Q^{-1})[6]. Higher-order terms (such as TPE), are treated in perturbation theory. If these high-order terms were iterated, by inserting them in the Schrödinger equation, then the forms of wave functions at short-distances would be altered, and therefore the power counting would no longer be consistent.

Other work that is closely related to that of the "deconstruction" approach in Refs. [80], [81], [82], [83], and in this thesis, include that of Valderrama [84] [85], and Long and Yang [86] [87] [87][7].

Whilst both Valderrama and Long and Yang iterate OPE to all orders, and treat TPE in perturbation theory, as we do, there are some differences between these approaches and that of ours. For example, Valderrama takes the standard EFT approach and fits a polynomial for the effective short-distance interaction to the phase shifts, instead of extracting an interaction directly from them. Long and

[6]However, we do still iterate OPE in channels where it is not strictly necessary to avoid having to treat OPE to fourth order in perturbation theory.

[7]See also Ref. [50].

Yang, on the other hand, work numerically in momentum space, and "promote counterterms over WPC where RG invariance requires it" [87].

There are some differences in terms of the power counting of the short-distance operators. For instance, up to order-Q^3, Valderrama proposes a total of 6 counterterms in each of the ${}^3S_1$-${}^3D_1$ and ${}^3P_2$-${}^3F_2$ channels, whereas Long and Yang suggest only 3 is needed in each of the coupled channels. Furthermore the RG analysis of [65] predicts that one extra counterterm is needed in the ${}^3S_1$ channel, compared to that of Valderrama. However, results suggest [84] that this extra term, may not be needed for renormalisability.

It should be mentioned that treating high-order terms perturbatively in this way does not necessarily translate well to being used in standard few- and many-body calculations. Iterating the whole potential to all orders, which requires a 'low' cut-off Λ (nearer the breakdown scale of the EFT), as in the Weinberg approach will likely remain the best way. However, this approach is still a useful means of analysing the formal details of the theory, and to extract a breakdown scale. One is also able to check the cut-off dependence of the theory over a wider range.

In this thesis, the "deconstruction" approach is extended further, and applied to the ${}^3S_1$-${}^3D_1$ and ${}^3P_2$-${}^3F_2$ coupled channels. The ${}^3S_1$-${}^3D_1$ coupled channel contains the deuteron, and so is especially interesting. By extracting an effective interaction matrix in each of these channels, we hope to help resolve the issue of how many counterterms are actually required in these channels for renormalisation.

Chapter 3

NN Scattering in Uncoupled Partial Waves

In this chapter we use a distorted-wave approach to analyse nucleon-nucleon (NN) scattering in the ${}^1P_1$ partial wave. The effects of one-pion exchange (OPE), two-pion exchange (TPE) and the recoil correction to OPE are removed from several Nijmegen phase shifts. After accounting for the single divergence that arises in this channel we are left with a short-range interaction that can be used to estimate the scale of the high-energy (underlying) physics.

The method is presented in a form that is relevant to general spin-singlet waves with non-zero orbital angular momentum. However, we show results for the ${}^1P_1$ channel only, as the other spin-singlet channels have already been analysed in this way by Birse and collaborators (see Refs. [80] and [82]). The work here has been published (see Ref. [83]) and was partly done in collaboration with K. Helmke.

3.1 Spin Singlet Waves: ${}^1P_1$

3.1.1 Distorted Waves

The starting point for the distorted-wave analysis of spin-singlet NN scattering for waves with $L \neq 0$, is to construct the distort-waves for the known long-range (OPE and centrifugal) potentials, denoted ψ_l, by solving the radial non-relativistic Schrödinger equation which is written as

$$\left[-\frac{\mathrm{d}^2}{\mathrm{d}r^2}-\frac{2}{r}\frac{\mathrm{d}}{\mathrm{d}r}+\frac{L(L+1)}{r^2}+U_{\pi C}(r)+U_{\pi T}(r)S_{12}\right]\psi_l(p,r)=p^2\psi_l(p,r), \quad (3.1)$$

where $U_{\pi C}(r) = M_N V_{\pi C}(r)$ and $U_{\pi T}(r) = M_N V_{\pi T}(r)$ denote central and tensor OPE reduced[1] potentials respectively, L denotes the orbital angular momentum of the two-nucleon system and S_{12} is the tensor operator defined as $S_{12} = 3(\boldsymbol{\sigma}_1 \cdot \hat{\boldsymbol{r}})(\boldsymbol{\sigma}_2 \cdot \hat{\boldsymbol{r}}) - \boldsymbol{\sigma}_1 \cdot \boldsymbol{\sigma}_2$. We also denote the radius of separation between the two nucleons by r, and the on-shell relative momentum in the centre-of-mass (COM) frame by p. The latter quantity, p, is connected to the laboratory kinetic energy, denoted T, by $T = 2p^2/M_N$. Note that in the spin-singlet waves $S_{12} = 0$ which means that there is no tensor OPE component present, only a central piece, making life a little easier for the present case. However, we will define both terms below, as knowledge of the tensor part is required in later chapters.

The central OPE potential is defined as

$$V_{\pi C}(r) = \frac{1}{3} f^2_{\pi NN} \left(\boldsymbol{\sigma}_1 \cdot \boldsymbol{\sigma}_2\right) \left[-\phi_C(m_{\pi^0}, r) \pm 2\phi_C(m_{\pi^\pm}, r)\right] \quad (3.2)$$

where

$$\phi_C(m, r) = \frac{m^2}{m_s^2}\frac{e^{-mr}}{r}, \quad (3.3)$$

and the tensor OPE potential is given by

$$V_{\pi T}(r) = \frac{1}{3} f^2_{\pi NN} \left[-\phi_T(m_{\pi^0}, r) \pm 2\phi_T(m_{\pi^\pm}, r)\right] \quad (3.4)$$

where

$$\phi_T(m, r) = \frac{m^2}{m_s^2}\frac{e^{-mr}}{r}\left(1 + \frac{3}{mr} + \frac{3}{m^2 r^2}\right). \quad (3.5)$$

These are written in essentially the same forms as those used by the Nijmegen group (see Refs. [17] and [14]). We also use the value they recommend for the πN coupling constant, given by $f^2_{\pi NN} = 0.075$. In Eqs. (3.2) and (3.4) $m_{\pi^\pm}$ and m_{π^0} denote the charged and neutral pion masses, respectively, and in Eqs. (3.3) and (3.5) m_s denotes the scalar mass, which by convention is taken to be equal to

[1] 'Reduced' here means $U = M_N V$, where V denotes the standard potential and M_N is the nucleon mass.

the charged pion mass. The plus(minus) signs in Eqs. (3.2) and (3.4) correspond to channels with total isospin $I = 1(0)$. We also have the spin factor $\boldsymbol{\sigma}_1 \cdot \boldsymbol{\sigma}_2$ defined by $\boldsymbol{\sigma}_1 \cdot \boldsymbol{\sigma}_2 = 2\left[S(S+1) - \frac{3}{2}\right]$, where S corresponds to the total spin of the system[2].

Having defined the quantities appearing in Eq. (3.1) we can proceed with the problem at hand - the construction of the distorted waves for spin-singlet NN scattering. There are two regions of coordinate space where the waves tend to known analytical forms: (i) 'near' the origin ($r \to 0$) and (ii) 'far' from the origin ($r \to \infty$). In both regions the centrifugal potential dominates over the central OPE potential, and the differential equation describing the complete problem at leading-order (Eq. (3.1)) simplifies to the standard spherical Bessel differential equation, whose general solutions are linear combinations of regular ($j_L(p,r)$) and irregular ($y_L(p,r)$) spherical Bessel functions of order L (see e.g. Ref. [88]).

For waves close to the origin we are free to choose the regular solution, and so we have

$$\psi_l(p,r) \xrightarrow{r\to 0} \frac{(pr)^L}{(2L+1)!!}. \tag{3.6}$$

This can be used to form the boundary condition required in order to numerically integrate the radial Schrödinger equation and obtain distorted waves, provided we start integrating in a region close enough to the origin where the OPE potential can be neglected.

For waves far from the origin the presence of the central OPE potential in the 'intermediate' region induces a distortion in the waves, characterised by a phase shift with respect to the undistorted, or free waves, denoted by $\delta_l(p)$. In other words, the central OPE potential induces a term proportional to the irregular spherical Bessel function ($y_L(p,r)$), and so we can write, for large r the general solution

$$\psi_l(p,r) \to A j_L(p,r) - B y_L(p,r), \tag{3.7}$$

where A and B are constants. For $r \to \infty$, the spherical Bessel functions can take their asymptotic forms, and so

[2]N.B. $S = 0(1)$ in spin-singlet(triplet) channels.

$$\psi_l(p,r) \xrightarrow{r\to\infty} \frac{A\sin\left(pr-\frac{L\pi}{2}\right)}{pr} + \frac{B\cos\left(pr-\frac{L\pi}{2}\right)}{pr} \tag{3.8}$$

$$\equiv \quad \frac{C\sin\left(pr-\frac{L\pi}{2}+\delta_l(p)\right)}{pr}. \tag{3.9}$$

Comparing Eqs. (3.8) and (3.9) one can easily show that $A = C\cos\delta_l$ and $B = C\sin\delta_l$, and therefore that $B = A\tan\delta_l$. Substituting this back in to Eq. (3.8) and reverting back to the spherical Bessel function notation, gives for large r

$$\psi_l(p,r) \to Aj_L(p,r) - A\tan\delta_l(p)y_L(p,r). \tag{3.10}$$

Calculating the logarithmic derivative of $\psi_l(p,r)$ written in this form, defined as $\frac{\psi_l'(p,r)}{\psi_l(p,r)}$, one can rearrange the resulting equation for $\tan\delta_l$, and therefore extract the phase shift due to OPE. Note that δ_l is both dependent on the central OPE potential (in this case) and on the on-shell momentum, i.e. $\delta_l = \delta_l(p)$.

To normalise the distorted waves, which is required when converting the residual K-matrix into an effective potential strength, we simply divide them by the coefficient A, which is obtained from Eq. (3.10). The result, of course, is that the coefficient of $j_L(p,r)$ is unity in the large r region. This is the correct way to normalise waves subject to standing wave boundary-conditions corresponding to the K-matrix. As a note, the equivalent standard normalisation procedure for waves subject to scattering-wave boundary conditions, is to fix the flux of incoming particles, by setting the coefficient of the incoming wave $\frac{1}{r}e^{-ipr}$ to one in the asymptotic region.

It should be mentioned that Weinberg power counting, relevant to the spin-singlet $L = 1$ channel, does not require the non-perturbative treatment of the OPE potential carried out here. It is performed, however, to remove the necessity to calculate terms to 4th order in perturbation theory [3]. We are allowed to do this because the 1/r structure of the (central) OPE potential does not change the power-law form of the wave functions near the origin, even when iterated by solving the Schrödinger equation. This means that the power counting of the terms in the short-range effective potential are unaffected.

[3] As was done in the higher spin-singlet partial waves in Ref. [80], the $^1S_0$ spin-singlet channel in Ref. [82], and certain peripheral uncoupled spin-triplet channels in Ref. [81] where treating OPE non-perturbatively cannot be justified.

3.1.2 Effective Residual Interaction

Subtracting the OPE phase shift $\delta_l(p)$ from the empirical phase shift $\delta(p)$ we can define a residual K-matrix,

$$\tilde{K}(p) = -\frac{4\pi}{M_N p} \tan\left(\delta(p) - \delta_l(p)\right). \tag{3.11}$$

This is a parameter that describes the scattering between the distorted waves of the known long-range potential (OPE in our case), produced by both short-range forces, and long-range forces that are of order Q^2 and higher (such as TPE and recoil-OPE etc.).

Assuming that the physics responsible for the additional scattering is unresolved at the energies of interest in our EFT, we choose to model it with a simple delta-shell potential,[4]

$$V_s(p,r) = \frac{\left[(2L+1)!!\right]^2}{4\pi R_0^{2L+2}} \tilde{V}(p)\delta\left(r - R_0\right) \tag{3.12}$$

with finite radius R_0 and strength $\tilde{V}(p)$. As in Refs. [82] and [80] (and [81] concerning uncoupled spin-triplet channels) we have divided out the square of the radial part of the small-r asymptotic wave function (see Eq. (3.6)). This is to ensure that the strength $\tilde{V}(p)$ is independent of the (arbitrary) radius R_0 for small R_0.

Given that the scattering in spin-singlet channels with $L > 0$ is weak, i.e. there are no bound states or resonances, their effective theories are based on expansions around trivial fixed points. This means that in the distorted-wave Born approximation (DWBA), $\tilde{K}(p)$ can be equated to the matrix element of $V_s(p,r)$, leading to the following expression for the residual scattering strength after the removal of OPE,

$$\tilde{V}^{(2)}(p) = \frac{R_0^{2L}}{\left[(2L+1)!!\psi_l(p,R_0)\right]^2} \tilde{K}(p), \tag{3.13}$$

where the superscript (2) implies that long-range forces of chiral order Q^2 and above are still present. Note that the orders at which the (short-range) contact interactions start depends on the specific partial wave in question, as discussed in the previous chapter. In spin-singlet channels, relevant here, they start at order

[4]Note that a delta-function (centered at $r = 0$) cannot be used here because partial waves with non-zero angular momentum vanish at the origin.

Q^{2L}.

After the removal of OPE, the most important of the remaining known long-range forces are TPE at order $Q^{2,3}$ and recoil-OPE at order Q^2. The matrix elements of which can be subtracted perturbatively from $\tilde{K}(p)$ using the DWBA to give a residual scattering strength whose long-range effects start at order Q^4,

$$\tilde{V}^{(4)}(p) = \frac{R_0^{2L}}{\left[(2L+1)!!\psi_l(p,R_0)\right]^2}\left(\tilde{K}(p) - \left\langle \psi_l(p)|V_{1\pi}^{(2)} + V_{2\pi}^{(2,3)}|\psi_l(p)\right\rangle\right). \quad (3.14)$$

The forms of the TPE potentials that we use are given in Refs. [37] and [89]. In the subleading (order Q^3) part of the TPE potential there appear three low-energy constants (originating from the order Q^2 πN Lagrangian) that are not fixed by chiral symmetry. The values we take are from an analysis by the Nijmegen group [90]: $c_1 = -0.76$ GeV^{-1}, $c_3 = -4.78$ GeV^{-1} and $c_4 = 3.96$ GeV^{-1}.

The recoil correction to OPE is, for a general wave, written as [91]

$$V_{1\pi}^{(2)}(r) = -\frac{p^2}{2M_N^2}\left[V_{\pi C}(r) + V_{\pi T}(r)\right], \quad (3.15)$$

where $V_{\pi C}(r)$ and $V_{\pi T}(r)$ are defined in Eqs. (3.2) and (3.4) respectively. Of course there is no contribution from $V_{\pi T}(r)$ in the spin-singlet channels.

Now, contrary to the higher spin-singlet waves analysed in Ref. [80], the matrix elements of TPE between $^1P_1$ distorted waves in Eq. (3.14) are divergent. To identify the divergences consider the following relation which defines how the matrix elements are evaluated in terms of radial integrals,

$$\langle\psi_l(p)|V(r)|\psi_l(p)\rangle = 4\pi\int_0^\infty V(r)\psi_l^2(p)r^2dr. \quad (3.16)$$

The two most singular terms are found in the order Q^3 part of the TPE potential and are proportional to $1/r^6$ and $1/r^5$. In the RHS of Eq. (3.16) these are multiplied by a factor of r^2 and the square of the $^1P_1$ wave function, which behaves like $\psi_l \propto r$ near the origin (see Eq. (3.6)). After integrating, this results in terms that are proportional to $1/r$ and $\ln r$. These are the terms responsible for the divergence in the matrix elements, and must be made finite. This is done simply by applying a cut-off to the lower limit of the integral in Eq. (3.16) at R_0, the same as the radius used to regulate the effective short-range interaction. However, this

leaves a residual interaction strength that has a strong dependence on R_0. Fortunately, Weinberg power counting provides an energy-independent counterterm at order Q^2 that can be used to remove this dependence. Practically speaking, the TPE matrix elements can be renormalised by subtracting their values at some low energy (we used 5 MeV)[5].

After having subtracted the effects of long-range forces up to chiral order Q^3 from the empirical phase shifts, and subsequently regularised and renormalised the residual scattering strength, what remains should be an effective interaction strength that has a smooth energy dependence and converges as the radial cutoff is lowered. A suitable polynomial in p^2 may then be fitted, whose coefficients can be used to estimate the scale of the underlying physics. This scale governs the convergence of expansion of our EFT. The results are presented in the next section.

3.1.3 Results and Discussion

Starting with Fig. 3.1, we show the phase shift due to iterated OPE in the $^1P_1$ channel as a function of laboratory kinetic energy. This is compared to the $^1P_1$ phase shifts from four different Nijmegen analyses: the 1993 Nijmegen partial-wave analysis (PWA93) and the Nijmegen I, Nijmegen II and Reid 93 high-quality potentials (see Refs. [17], [14] and [92]). The potentials were fit to the same NN scattering data as the 1993 partial-wave analysis, and all fit the data with similarly good values of chi-squared, therefore they can be regarded as alternative PWAs whose differences give some measure of the systematic uncertainties involved.

One can see in the plot in Fig. 3.1 that at low enough energies iterated OPE is sufficient to describe the scattering data. As the energy increases, however, this is no longer the case. This is because at higher energies the nucleons interact at closer distances, overcoming the centrifugal barrier, and other processes (such as TPE) begin to contribute.

In Fig. 3.2 we show the effective short-range potential $\tilde{V}^{(2)}(p)$ after the removal of iterated OPE as a function of laboratory kinetic energy, using a cut-off radius of $R_0 = 0.1$ fm. It should be noted that such a cut-off is well outside the validity range of the EFT, but using a 'small' value ensures that any remaining cut-off

[5]In theory any value of energy can be chosen at which to subtract the TPE matrix elements, as the divergence in the $^1P_1$ channel is a constant, i.e. independent of energy. However, a low value is preferable as we are building an effective field theory based on an expansion in powers of energy, therefore any extra finite terms we may be subtracting will be small.

dependent artefacts in the effective short-range potential (that are proportional to positive powers of R_0) are insignificant. We show results for the four Nijmegen PWAs mentioned above hence the four curves. It is clear from the plot that there is significant energy dependence present at low energies, as is the case in the higher spin-singlet partial waves in Ref. [80]. This indicates that there are still important long-range forces participating in the interaction. Of course there are noteable differences in the curves below energies of about 50 MeV, highlighting the fact that this region is not well constrained by the data. This is because, as can be seen in the previous plot, OPE is the dominant interaction in the low energy region, and by this stage in the analysis OPE has been subtracted out from the data.

In Fig. 3.3 we show the **unrenormalised** effective short-range potential after the perturbative removal of order-$Q^{2,3}$ TPE and order-Q^2 recoil OPE potentials using the DWBA. Results are shown for the following cut-off radii: $R_0 = 0.8$ fm (short-dashed), 0.4 fm, 0.2 fm, 0.1 fm and 0.05 fm (solid). This figure shows the strong dependence of the short-range effective interaction on the cut-off radius R_0 that occurs in this channel before the single energy-independent Q^2 counterterm has been used to renormalise.

By including this counterterm we obtain the **renormalised** results in Fig. 3.4. The curves in this figure show that even the slightly 'ad hoc'renormalisation procedure that was performed here (simply by subtracting the values of the matrix elements of the TPE potential at T =5 MeV) has been able to remove the strong dependence on R_0 that was seen in Fig. 3.3, particularly at low energies. As $R_0 \to 0$ the renormalised effective short-range potential converges to a cut-off independent form.

Finally we show in Fig. 3.5 the (renormalised) effective short-range potential $\tilde{V}^{(4)}(p)$ after the perturbative removal of both the order-$Q^{2,3}$ TPE and order-Q^2 recoil OPE potentials using the DWBA for four Nijmegen PWAs, using a radial cut-off of $R_0 = 0.1$ fm. After removing OPE and TPE up to order Q^3, we obtain a smoothly energy-dependent residual interaction from about 70 MeV upwards, this implies that all important long-range forces have been removed, and what is left can be represented by contact interactions. The prominant downwards curvature at low energies that was present in Fig. 3.2 has been substantially reduced, and what curvature remains is within the uncertainties of the four Nijmegen fits. Although again it should be stressed that this region is not well constrained by

the data so no definite conclusions can be made.

To extract a scale for the short-distance physics from $\tilde{V}^{(4)}(p)$ we made a least-squares fit of a quadratic polynomial in p^2, in the energy range: $T = 100 - 200$ MeV. Polynomials of higher orders were also investigated, but the data appeared to be too 'inaccurate' to stabilise the values of the coefficients. The energy range was chosen to avoid both the low-energy region where the Nijmegen fits become unreliable, and the high-energy region where the EFT may no longer be valid. Writing the polynomial as

$$\tilde{V}^{(4)}(p) = a_0 + a_1 p^2 + a_2 p^4, \tag{3.17}$$

we obtain the following coefficients: $a_0 = 0.28$ fm^4, $a_1 = -0.20$ fm^6 and $a_2 = 0.0056$ fm^8. As the uncertainties on the Nijmegen phase shifts that are used to determine the effective potential are unknown, it is difficult to assign definite errors to these coefficients and therefore determine their reliability to calculate an expansion scale. However, simple estimates indicate that a_0 and a_1 are reasonably accurate, whereas a_2 is not. Unfortunately, due to our rather unrefined method of renormalisation, we cannot use a_0 to determine an estimate for the scale of the short-distance physics. This leaves us with the coefficient a_1 from which to extract a scale.

Assuming a "natural" theory, a_1 should be related to the scale of the short-distance physics Λ_0 by $a_1 = \hat{a}_1/{\Lambda_0}^6$, where $\hat{a}_1$ is dimensionless and of order unity. Setting $\hat{a}_1 = -1$ gives us a value for the scale of approximately 260 MeV [6]. This low value indicates the presence of additional low-energy physics that has not been accounted for in our EFT, such as the Δ-resonance, the lowest baryon resonance. With a mass of about 1230 MeV, less than 300 MeV above the nucleon, it is one of the lowest-energy excitations not included in our EFT. Therefore, including it as an explicit degree of freedom (as done in Refs. [38] and [93]) could produce a more 'natural' short-range effective potential.

[6] This is close to the scale estimated for the $^1S_0$ channel in Ref. [82].

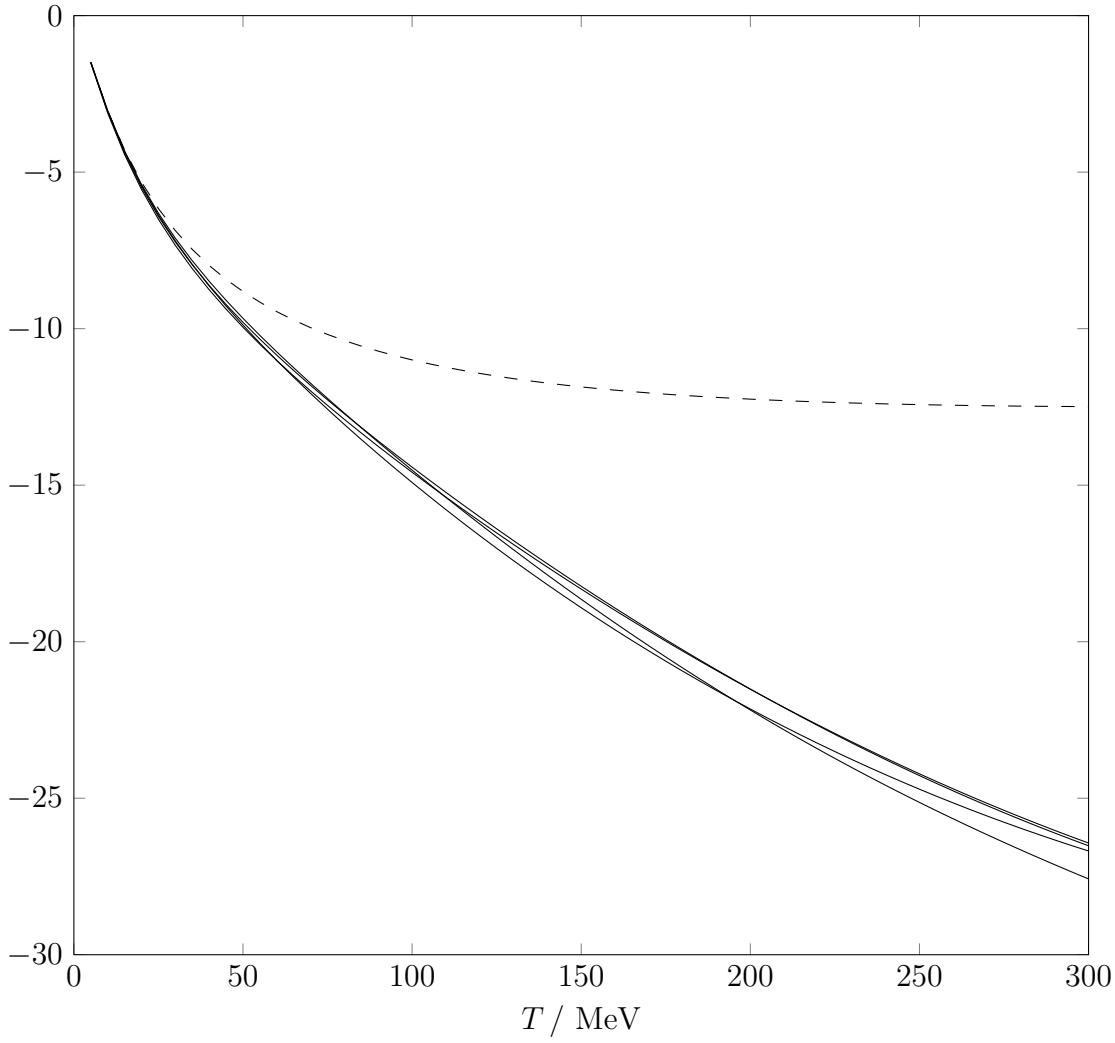

Figure 3.1: The phase shifts in the ${}^1P_1$ channel (in degrees): the dashed curve is the phase shift due to iterated OPE, while the solid curves correspond to four different Nijmegen PWAs. T is the lab kinetic energy.

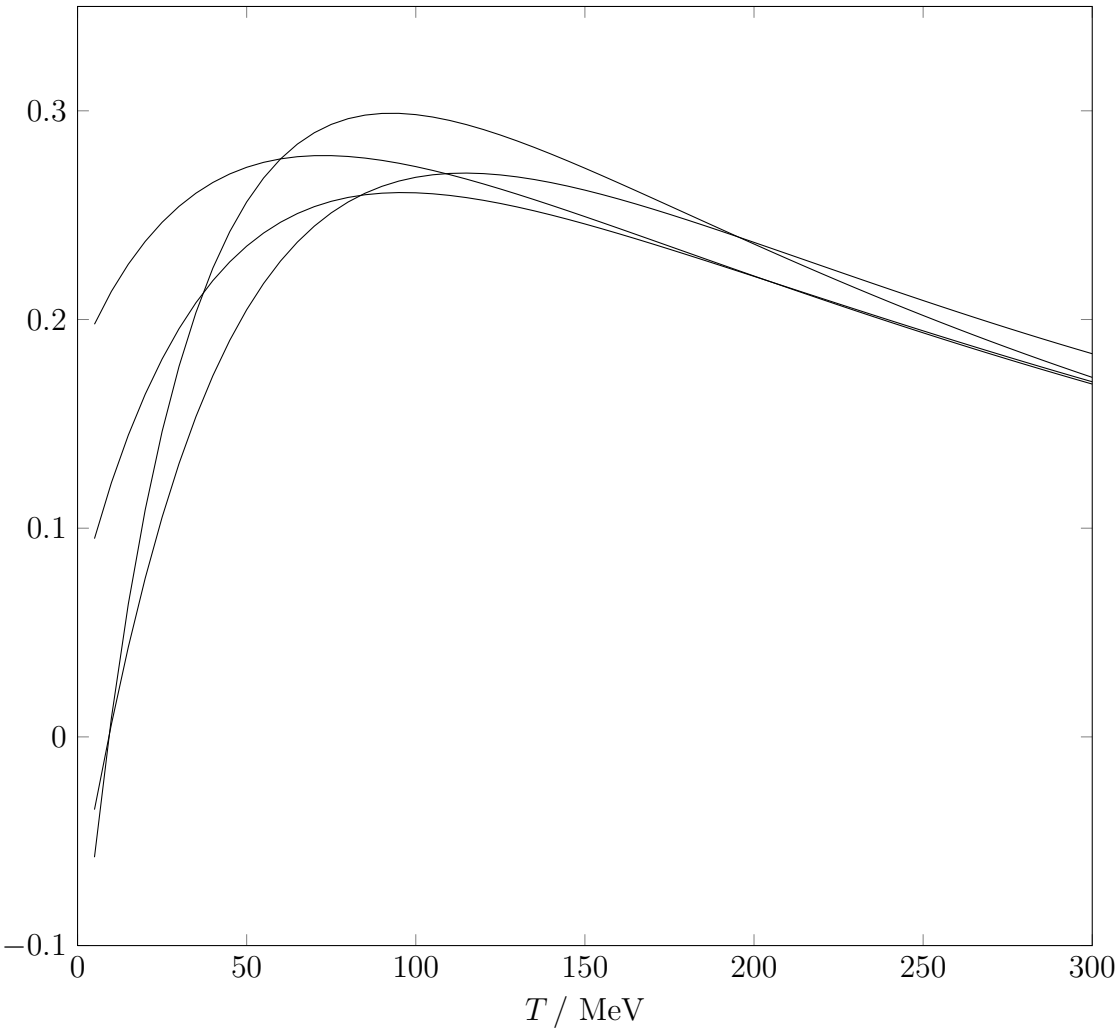

Figure 3.2: The short-range effective potential $\tilde{V}^{(2)}(p)$ (in fm^4) after the removal of OPE, using a delta-shell radius of $R_0 = 0.1$fm. The four curves correspond to the different Nijmegen PWAs.

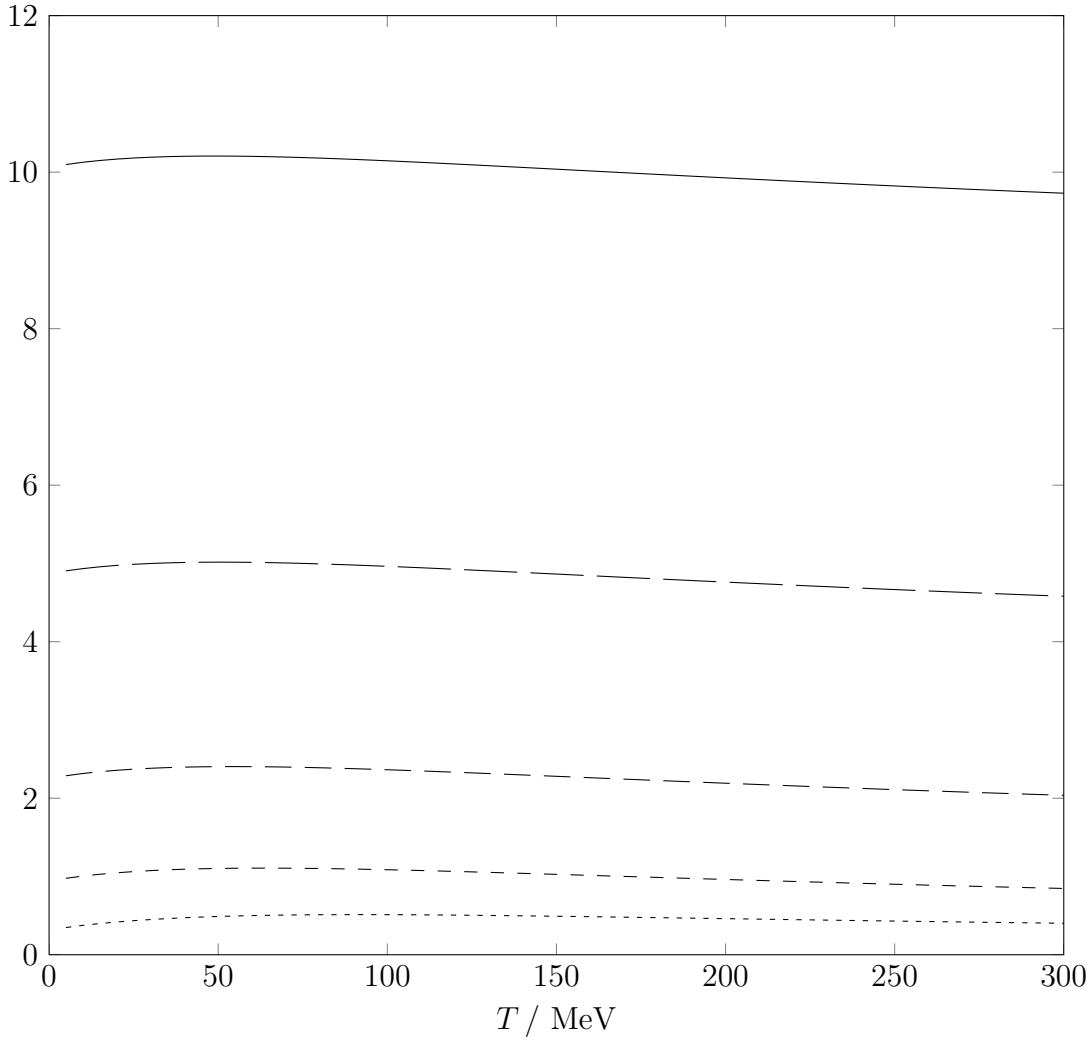

Figure 3.3: The unrenormalised short-range effective potential $\tilde{V}^{(4)}(p)$ (in fm^4) extracted from PWA93 phase shifts. The curves correspond to cut-off radii $R_0 = 0.8$ (short-dashed), 0.4, 0.2, 0.1 and 0.05 fm (solid).

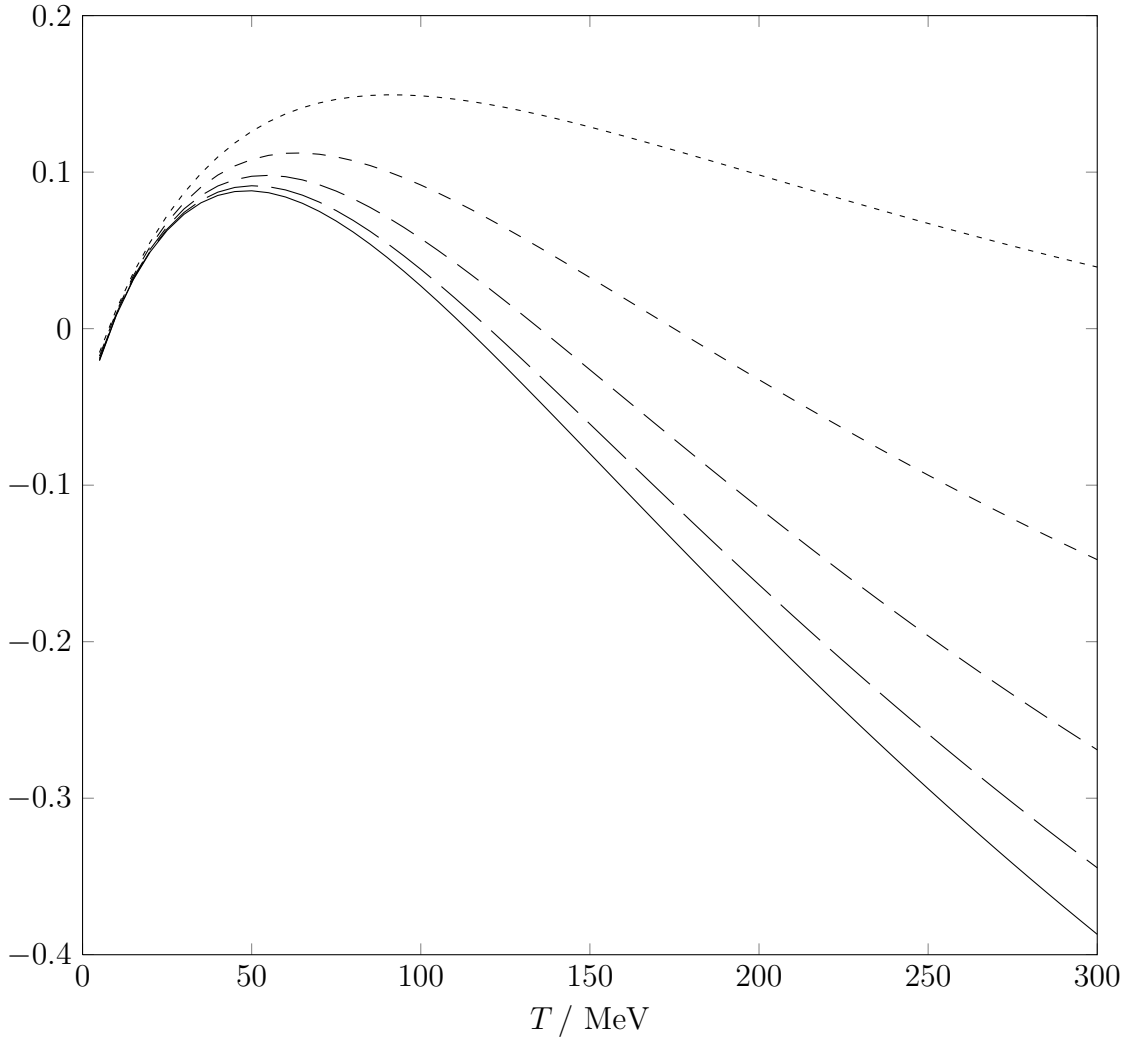

Figure 3.4: The renormalised short-range effective potential $\tilde{V}^{(4)}(p)$ (in fm^4) extracted from PWA93 phase shifts. The curves correspond to cut-off radii $R_0 = 0.8$ (short-dashed), 0.4, 0.2, 0.1 and 0.05 fm (solid).

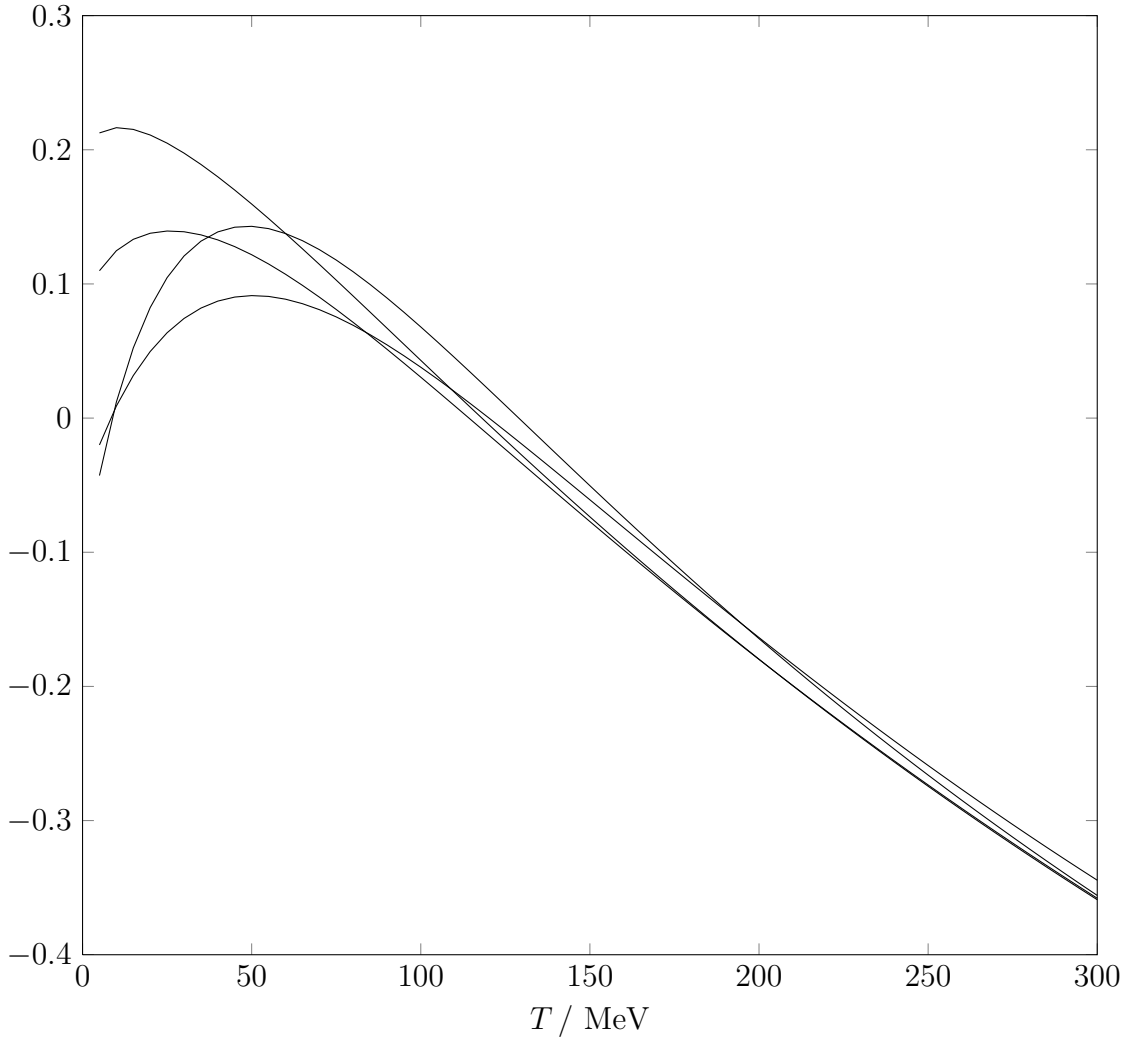

Figure 3.5: The renormalised short-range effective potential $\tilde{V}^{(4)}(p)$ (in fm^4), using four different Nijmegen PWAs and a cut-off radius of 0.1fm.

J	Even Parity	Odd Parity
0	–	$^3P_0$
1	$^3S_1 - {}^3D_1$	$^3P_1$
2	$^3D_2$	$^3P_2 - {}^3F_2$
3	$^3D_3 - {}^3G_3$	$^3F_3$
4	$^3G_4$	$^3F_4 - {}^3H_4$

Table 3.1: Classification of spin-triplet states by their total angular momentum and parity [94].

3.2 Spin Triplet Waves

In section 3.1 we presented how to build an effective field theory for NN scattering using distorted-wave methods in the ($L \neq 0$) spin-singlet ($S = 0$) channels, with specific focus on the $L = 1$ channel. These channels are "limited" in the sense that they only experience the central part of the OPE interaction. We are therefore also interested in investigating the spin-triplet ($S = 1$) channels, where the tensor part of the OPE force also plays a role.

The tensor force couples together spin-triplet states whose total angular momentum $J = L \pm 1$ (the $^3P_0$ state, however, is an exception to this rule as it is uncoupled). States with $J = L$ are decoupled from the pair as they have opposite parity,[7] see Table 3.1.

In Ref. [81] Birse examined the uncoupled spin-triplet states given in Table 3.1, therefore in this thesis we focus solely on the coupled channels. Although we only examine the $^3S_1 - {}^3D_1$ and $^3P_2 - {}^3F_2$ coupled channels, the same methods can be used to examine the more peripheral coupled waves as well.

Before we look into the coupled waves, however, we will first mention here some of the key aspects of Ref. [81]. We will also refer to some of the relevant results in Ref. [65] which provide some of the formal implications to the work in Ref. [81]. This will hopefully bridge the gap between the uncoupled spin-singlet states of the previous section and the coupled spin-triplet states of the next chapters, which may be helpful to the reader.

The starting point for the analysis of the uncoupled spin-triplet waves is the same as that used for the spin-singlet states, i.e. it is the construction of the distorted waves. These are obtained by solving the radial Schödinger equation

[7] Parity is given by $(-1)^L$.

given in Eq. (3.1), only this time, of course, the tensor potential term is non-zero.[8]

In Eq. (3.1) the most singular term that appears now is in the tensor OPE potential and goes like $1/r^3$. It is this term that therefore (predominantly) governs the forms of the wave functions as $r \to 0$, not the $1/r^2$ centrifugal barrier. So in this region the spin-triplet waves are very different from the spin-singlet waves, at least for the waves which are able to penetrate the centrifugal barrier.

In Ref. [81] Birse obtained analytical solutions for the distorted waves at small r by first examining Eq. (3.1) in the chiral limit ($m_\pi = 0$) and at zero energy, to give

$$\left[\frac{\mathrm{d}^2}{\mathrm{d}r^2} + \frac{2}{r}\frac{\mathrm{d}}{\mathrm{d}r} - \frac{L(L+1)}{r^2} - \frac{\beta_{LJ}}{r^3}\right]\psi_0(r) = 0, \tag{3.18}$$

where the length scale, β_{LJ} is defined as

$$\beta_{LJ} = \frac{S_{12}(\tau_1.\tau_2)}{\lambda_\pi} = \begin{cases} -4/\lambda_\pi, & L = 1,\ J = 0, \\ +2/\lambda_\pi, & L = J \text{ odd}, \\ -6/\lambda_\pi, & L = J \text{ even}, \end{cases} \tag{3.19}$$

and where

$$\lambda_\pi = \frac{m_\pi^2}{f_{\pi NN}^2 M_N}, \tag{3.20}$$

which in the chiral limit is given as

$$\lambda_\pi = \frac{16\pi F_\pi^2}{g_A^2 M_N}, \tag{3.21}$$

where g_A is the nucleon axial coupling constant and F_π is the pion decay constant.

Then by simultaneously defining a new variable $x = \sqrt{|\beta_{LJ}|/r}$ and the function $\phi(x) = x^{-1}\psi_0(|\beta_{LJ}|/x^2)$, Birse obtained the following equation

$$\left[\frac{\mathrm{d}^2}{\mathrm{d}x^2} + \frac{1}{x}\frac{\mathrm{d}}{\mathrm{d}x} - \frac{(2L+1)^2}{x^2} \pm 4\right]\phi(x) = 0, \tag{3.22}$$

whose solutions are the well-known Bessel functions, of order $2L + 1$. Note that in Eq. (3.22) the plus(minus) sign corresponds to waves with even(odd) J, and it originates from the factor $-\beta_{LJ}/|\beta_{LJ}|$ (see Eq. (3.19))..

This implies therefore that the solutions for the attractive tensor potentials

[8] In the uncoupled spin-triplet states, S_{12} is $+2$ in the $L = J$ waves, and -4 in the $^3P_0$ wave.

in Eq. (3.18) have the forms

$$\psi_0(r) = A\sqrt{\frac{|\beta_{LJ}|}{r}}\left[\sin\alpha J_{2L+1}\left(2\sqrt{\frac{|\beta_{LJ}|}{r}}\right) + \cos\alpha Y_{2L+1}\left(2\sqrt{\frac{|\beta_{LJ}|}{r}}\right)\right], \quad (3.23)$$

and the solutions for the repulsive tensor potentials are given by

$$\psi_0(r) = A\sqrt{\frac{|\beta_{LJ}|}{r}}K_{2L+1}\left(2\sqrt{\frac{|\beta_{LJ}|}{r}}\right), \quad (3.24)$$

where J_{2L+1}, Y_{2L+1} denote the regular and irregular Bessel functions respectively, and K_{2L+1} denotes the modified Bessel function of the second kind. As one can see, these solutions are obviously very different from the power-law forms of the spin-singlet waves for small r (see Eq. (3.6)), which result from the pure centrifugal potential.

Note that the attractive solutions in Eq. (3.23) are dependent on a free (energy-independent) parameter, denoted α. As mentioned by Birse in Ref. [81] (see also Ref. [65]), this parameter fixes the phase of the oscillations of the waves at small distances, thus specifying a self-adjoint extension of the original Hamiltonian. It is required because both Bessel functions in Eq. (3.23) provide equally good solutions for an attractive tensor potential as $r \to 0$, and therefore so does their linear combination.

Like α, the leading, energy-independent term in the short-range effective potential also fixes the phase of the solutions at small distances, so there is a redundancy between the two. The energy-dependent higher-order terms in the effective potential, however, completely describe the energy dependence resulting from short-range (high-energy) physics [65].

There are certain values of α that are better suited for different circumstances. For instance, a value of $\alpha = 0$ is suitable to channels with weak scattering, and allows the short-range effective potential alone to describe the short-distance physics. This particular value of α switches off the regular Bessel function in Eq. (3.23), which results in solutions to Eq. (3.18) that are proportional to r^L for large r. Conversely, a value of $\alpha = \pi/2$ switches off the irregular Bessel function in Eq. (3.23), leaving solutions that are proportional to $r^{-(L+1)}$ for large r, and are large at small values of r, which is relevant to NN interactions that result in bound states or resonances.

Now, by solving the Schrödinger equation with the OPE potential as in Eq. (3.1), we are implicitly treating OPE non-perturbatively by iterating it to all orders. In the spin-triplet channels where this treatment is necessary, it needs to be justified by identifying an additional low-energy scale so that OPE is promoted to order Q^{-1}. However, in the other spin-triplet channels where OPE could be treated perturbatively, this is just done as a useful alternative to performing perturbation theory to fourth order.

In Ref. [65], Birse identified the additional low-energy scale just mentioned as the scale of the OPE potential, λ_π defined in Eqs. (3.20) and (3.21). Note that even though in Eq. (3.21), λ_π is constructed from high-energy scales, its actual numerical value is rather small, approximately 290 MeV. Therefore treating this scale as a low-energy scale is not unreasonable, although the concrete connection to ChPT is lost.

To determine which spin-triplet waves require the non-perturbative treatment of OPE, Birse calculated, in Ref. [65], the values for the critical momentum for each specific partial-wave of interest above which the perturbative treatment of OPE (in the chiral limit[9]) breaks down (see also Ref. [79]), these are given in Table 2.2. For momenta above these critical values the waves are able to overcome the centrifugal barrier and resolve the region dominated by the $1/r^3$ part of the tensor OPE potential. The values in Table 2.2 indicate that for waves with $L \leq 2$ OPE should be treated non-perturbatively for the energies of interest here, however, for waves with $L \geq 3$ OPE can be treated perturbatively. This agrees with conclusions drawn from the wave function plots in Fig. 1 of Ref. [81].

As the form of the long-range potentials govern the form of the wave functions near the origin (see Eqs. (3.23), (3.24) and (3.6)), they therefore also affect the resulting power counting of the short-range effective potentials. For the spin-triplet waves where OPE can be treated perturbatively the power counting of the short-range interactions start at order-Q^{2L} (this is just the power counting due to naive dimensional analysis. i.e. Weinberg power counting), resulting from the wave functions due to the centrifugal potential that are proportional to r^L as $r \to 0$, like that for the spin-singlet waves. On the other hand, waves which are dominated by the $1/r^3$ part of the tensor potential near the origin, tend to the

[9]Values for the critical momenta for finite m_π will be higher (though still of order m_π) [65].

form of a sinusoidal(exponential) function of $2\sqrt{|\beta_{LJ}/r|}$ multiplied by $r^{-1/4}$ for the attractive(repulsive) potentials (see Eqs. (3.23) and (3.24)), resulting in very different power counting from that due to the centrifugal potential.

In Ref. [65] Birse performed an RG analysis of the short-range effective potential in the presence of the tensor OPE potential. As discussed in that paper it is the power-law dependence of r of the DWs that governs the RG flow of the effective short-range interactions, therefore the power counting for the attractive and repulsive tensor potentials is in fact the same. In the spin-triplet waves with $L \leq 2$, expanding around the trivial fixed point, relevant to waves with no low-energy bound states or resonances, results in terms in the short-distance potential that appear at orders $Q^{-1/2}$, $Q^{3/2}$, $Q^{7/2}$,$\cdots$. This provides a quantitative form for the "new" power counting that was found to be necessary in certain spin-triplet waves by the numerical work of Ref. [68]. As argued by the authors of Ref. [67], however, this does depend on the chosen value for the cut-off.

The residual scattering strength after the removal of leading-order OPE is obtained in the same way for the uncoupled spin-triplet waves examined by Birse in Ref. [81] as the spin-singlet waves analysed in Refs. [80] and [83], the only difference being the form of the short-distance wave function that is divided out in the definition of the δ-shell potential. Slightly more care has to be taken when calculating this quantity in the attractive spin-triplet waves especially, where the nodes of the wave functions should be avoided. After removing the effects of leading-order OPE this leads to a residual scattering strength whose long-range forces now start at chiral-order Q^2. There may still be, however, short-range forces present that arise at lower-orders than this (as discussed above) depending on the wave under examination.

Again, the removal of the next important long-range forces, TPE and recoil-OPE, is similar to that done in the spin-singlet channels. The most interesting difference is due to the divergences that arise which must be regularised and then renormalised, more similar to the $^1P_1$ channel in Ref. [83] only here there are divergences that are energy-dependent. To do this Birse fitted a quadratic of the form

$$\tilde{V}^{(7/2)}(p) = C_0 + C_2 p^2 + C_4 p^4, \tag{3.25}$$

in the energy-range 100 - 200 MeV, which after subtracting should leave a residual interaction that only involves terms that are order Q^4 or more.

The results presented in Figs. 2 - 7 in Ref. [81] suggest that for the P and D spin-triplet waves after the removal of the effects of long-range forces up to and including order-Q^3 the resulting residual short-distance interactions can be fitted well by the three contact terms that are provided by the "new" power counting. In addition, for the F and G waves, as far as the uncertainties in the plots allow conclusions to be drawn, it appears that Weinberg power counting is suitable, at least for the energies considered.

Chapter 4

NN Scattering in Coupled Partial Waves

In chapter 3 we used effective field theory techniques to analyse nucleon-nucleon scattering in the uncoupled channels, specifically the ${}^1P_1$ channel. We now turn our attention to nucleon-nucleon scattering in channels coupled via the tensor OPE interaction. Our focus is particularly aimed at the ${}^3S_1 - {}^3D_1$ channel, because this contains the deuteron − the simplest stable system bound by nuclear forces, consisting of a proton and a neutron.

As in the spin-singlet and spin-triplet uncoupled channels, the starting point for a distorted-wave analysis of NN scattering in coupled waves is to construct distorted-waves of the known long-range (OPE) potential. In coupled channels with total angular momentum J this is done by solving the following pair of radial Schrödinger equations:

$$\left(\frac{\mathrm{d}^2}{\mathrm{d}r^2} + p^2 - U_{\pi C}(r) + \frac{2(J-1)}{2J+1}U_{\pi T}(r) - \frac{J(J-1)}{r^2}\right)u_l(r)$$

$$= \frac{6\sqrt{J(J+1)}}{2J+1}U_{\pi T}(r)w_l(r) \qquad (4.1)$$

$$\left(\frac{\mathrm{d}^2}{\mathrm{d}r^2} + p^2 - U_{\pi_C}(r) + \frac{2(J+2)}{2J+1}U_{\pi_T}(r) - \frac{(J+1)(J+2)}{r^2}\right)w_l(r)$$

$$= \frac{6\sqrt{J(J+1)}}{2J+1}U_{\pi_T}(r)\,u_l(r), \qquad (4.2)$$

where u_l and w_l denote distorted-waves[1] with total orbital angular momentum $L = J-1$ and $L = J+1$ respectively, p denotes the asymptotic momentum in the centre-of-mass frame, and $U_{\pi_C}(r)$ and $U_{\pi_T}(r)$ denote central and tensor OPE reduced potentials,[2] respectively. The centrifugal potentials are written in their less familiar form using total angular momentum J instead of total orbital angular momentum L, for obvious reasons.

The various factors multiplying $U_{\pi_T}(r)$ result from the tensor operator S_{12} (defined in the previous chapter) acting on normalized spin-angle wave functions for (spin-triplet) states with $L = J \pm 1$ [95]:

$$S_{12}\Phi_{L=J-1} = -\frac{2(J-1)}{2J+1}\Phi_{L=J-1} + \frac{6\sqrt{J(J+1)}}{2J+1}\Phi_{L=J+1}$$

$$S_{12}\Phi_{L=J+1} = -\frac{2(J+2)}{2J+1}\Phi_{L=J+1} + \frac{6\sqrt{J(J+1)}}{2J+1}\Phi_{L=J-1}. \qquad (4.3)$$

The S_{12} tensor operator only couples waves together that differ in angular momentum by a factor of two. So for the deuteron, for example, which is predominantly a $L = 0$ state, the S_{12} operator induces a contribution from the $L = 2$ state. This can be seen, in a simplistic way, by writing S_{12} in the following form

$$\begin{aligned} S_{12} &= 3(\boldsymbol{\sigma}_1 \cdot \hat{\boldsymbol{r}})(\boldsymbol{\sigma}_2 \cdot \hat{\boldsymbol{r}}) - \boldsymbol{\sigma}_1 \cdot \boldsymbol{\sigma}_2 \\ &= \left(3\hat{r}^i\hat{r}^j - \delta^{ij}\right)\sigma_i\sigma_j, \end{aligned} \qquad (4.4)$$

and examining $3\hat{r}^i\hat{r}^j - \delta^{ij}$ (a rank 2 tensor that is traceless and symmetric under

[1] u_l and w_l are actually 'reduced' wave functions, i.e. they are related to 'standard' wave functions by dividing them by r.

[2] See Eqs. (3.2) and (3.4) for their definitions.

the interchange $i \leftrightarrow j$) under specific combinations of i and j. The easiest combination to look at is $i = j = 3$ which gives, remembering that $\hat{z} = \hat{r}^3 = \cos\theta$ in spherical polar coordinates,

$$\begin{aligned} 3\hat{r}^3\hat{r}^3 - \delta^{33} &= 3\cos^2\theta - 1 \\ &= \sqrt{\frac{16\pi}{5}} Y_{2,0}(\theta,\phi), \end{aligned} \tag{4.5}$$

where $Y_{2,0}(\theta,\phi)$ is the standard spherical harmonic of the form $Y_{l,m}(\theta,\phi)$. Similarly, setting for example, $i = 1$ and $j = 3$, and remembering that $\hat{x} = \hat{r}^1 = \sin\theta\cos\phi$ gives

$$\begin{aligned} 3\hat{r}^1\hat{r}^3 - \delta^{13} &= 3\sin\theta\cos\theta\cos\phi \\ &= \sqrt{\frac{18\pi}{5}} \left(Y_{2,-1}(\theta,\phi) - Y_{2,1}(\theta,\phi)\right). \end{aligned} \tag{4.6}$$

The crucial point is that both examples are given in terms of spherical harmonics of the type $Y_{2,m}(\theta,\phi)$.

4.1 Spin Triplet Waves: ${}^3S_1 - {}^3D_1$

Having set up the equations for general angular momentum J, we concentrate on the ${}^3S_1 - {}^3D_1$ waves, postponing the discussion of the ${}^3P_2 - {}^3F_2$ waves to a later section of the thesis.

4.1.1 Distorted Eigen Waves

Setting $J = 1$ Eqs. (4.1) and (4.2) become

$$\left(\frac{\mathrm{d}^2}{\mathrm{d}r^2} + p^2 - U_{\pi C}(r)\right) u_l(r) = 2\sqrt{2} U_{\pi T}(r) w_l(r) \tag{4.7}$$

and

$$\left(\frac{\mathrm{d}^2}{\mathrm{d}r^2} + p^2 - U_{\pi C}(r) + 2U_{\pi T}(r) - \frac{6}{r^2}\right) w_l(r) = 2\sqrt{2} U_{\pi T}(r) u_l(r), \tag{4.8}$$

where u_l and w_l now denote the S and D partial waves, respectively.

Now, with any discussion concerning the construction of distorted-waves, there are two regions of coordinate space to consider: (i) near the origin ($r \to 0$) and (ii) in the asymptotic limit ($r \to \infty$), we shall discuss each in turn.

Starting close to the origin, we can expand the OPE central and tensor potentials about $r = 0$, remembering that the ${}^3S_1 - {}^3D_1$ waves have total isospin $I = 0$, giving,

$$\begin{aligned} U_{\pi C}(r) &= -\frac{2m^2 R}{3}\frac{e^{-mr}}{r} \\ &= -\frac{2m^2 R}{3r} + \frac{2m^3 R}{3} - \frac{m^4 R r}{3} + \cdots \end{aligned} \tag{4.9}$$

and

$$\begin{aligned} U_{\pi T}(r) &= -\frac{2m^2 R}{3}\frac{e^{-mr}}{r}\left(1 + \frac{3}{mr} + \frac{3}{m^2 r^2}\right) \\ &= -\frac{2R}{r^3} + \frac{m^2 R}{3r} - \frac{m^4 R r}{12} + \cdots, \end{aligned} \tag{4.10}$$

where we have ignored the differences due to charged and neutral pion masses, by taking their average value m (note that the differences can of course be reintroduced at a later point in the calculation) and have defined the length scale[3]

$$R = \frac{3 f_{\pi NN}^2 M}{2 m_s^2}. \tag{4.11}$$

From Eqs. (4.9) and (4.10) we can see that, as expected, the most singular term appears in the tensor OPE potential and goes like $1/r^3$. This is the term that remains if we choose to work in the chiral limit, i.e. setting $m = 0$. Close to the origin this term is dominant and governs the forms of the wave functions here. This is unlike for the spin-singlet channels, where in the small-r region the centrifugal barrier dominated over the central OPE potential, and so the waves there tended to the forms $\propto (pr)^L$ as $r \to 0$. By keeping only this $(1/r^3)$ part of the OPE potential, ignoring the energy term, p^2, and the centrifugal potential

[3]Valderrama and Arriola [96] use $R = \dfrac{3 g_A^2 M}{32\pi f_\pi^2}$ which is related to Eq. (4.11) via the Goldberger-Treiman relation.

in the D-wave, the Schrödinger equations (Eqs. (4.7) and (4.8)) can be cast into a matrix equation which can be diagonalised into an attractive-repulsive (A-R) basis by performing a unitary transformation using the operator $\hat{U}$ [96] [97],

$$\hat{U} = \frac{1}{\sqrt{3}} \begin{pmatrix} \sqrt{2} & 1 \\ -1 & \sqrt{2} \end{pmatrix}. \tag{4.12}$$

giving:

$$\begin{pmatrix} -\frac{\mathrm{d}^2}{\mathrm{d}r^2} - \frac{4R}{r^3} & 0 \\ 0 & -\frac{\mathrm{d}^2}{\mathrm{d}r^2} + \frac{8R}{r^3} \end{pmatrix} \begin{pmatrix} u_A(r) \\ u_R(r) \end{pmatrix} = \begin{pmatrix} 0 \\ 0 \end{pmatrix} \tag{4.13}$$

where we have used:

$$\begin{pmatrix} u_A(r) \\ u_R(r) \end{pmatrix} = \frac{1}{\sqrt{3}} \begin{pmatrix} \sqrt{2} & 1 \\ -1 & \sqrt{2} \end{pmatrix} \begin{pmatrix} u_l(r) \\ w_l(r) \end{pmatrix}. \tag{4.14}$$

In Eqs. (4.13) and (4.14), $u_A(r)$ and $u_R(r)$ denote solutions to the attractive $\left(-\frac{4R}{r^3}\right)$ and repulsive $\left(+\frac{8R}{r^3}\right)$ potentials , respectively. Importantly, written in this basis Eq. (4.13) shows clearly that the waves decouple in the region where the $1/r^3$ part of the tensor OPE potential dominates (i.e. the off-diagonal elements are zero). Also, by looking at the inverse of Eq. (4.14), it can be shown that for purely attractive waves $u_l/w_l = \sqrt{2}$ and for purely repulsive waves $u_l/w_l = -1/\sqrt{2}$.

In theory, one could use the forms of the wave functions given in Ref. [81], for the uncoupled spin-triplet waves, to describe waves in the small-r region, however, in practice, it would seem that one has to be very close (impractically so) to the origin to enter a region where the coupling due to the centrifugal barrier[4] can be neglected.

Instead we use forms for the waves derived by Valderrama and Arriola [96]. They derive the waves by writing u_l and w_l as a power series expansion in r, inserting them into the coupled radial Schödinger equations (with the potentials also written as a power series in r, truncated to the desired order) and essentially reading off the various unknown coefficients at each order.

[4]In the attractive-repulsive basis of Eq. (4.13), if we had included the centrifugal potential when performing the unitary transformation, its terms would have appeared in the off-diagonal elements, thus coupling the waves in that basis. As we know, in the usual S-D basis it is the tensor OPE potential that couples the waves.

More explicitly, one writes the solutions in the forms

$$\begin{aligned} u_l(r) &= u_0 \left(\frac{r}{R}\right)^{a_1} e^{a_0\sqrt{\frac{R}{r}}} f(r) \\ w_l(r) &= w_0 \left(\frac{r}{R}\right)^{a_2} e^{a_0\sqrt{\frac{R}{r}}} g(r), \end{aligned} \tag{4.15}$$

where $f(r) = \sum_{n=0}^{\infty} A_n \left(\frac{r}{R}\right)^{n/2}$ and $g(r) = \sum_{n=0}^{\infty} B_n \left(\frac{r}{R}\right)^{n/2}$.

Consider first the simplest scenario where we derive the wave functions for just the $1/r^3$ part of the OPE potential.[5] By inserting the forms for u_l and w_l given in Eq. (4.15) into Eqs. (4.7) and (4.8), one gets for the $n = 0$ equations:

$$\begin{aligned} \frac{1}{4}a_0^2 u_0 + 4\sqrt{2}w_0 &= 0 \\ \frac{1}{4}a_0^2 w_0 - 4w_0 + 4\sqrt{2}u_0 &= 0, \end{aligned} \tag{4.16}$$

where we have set $a_1 = a_2$ to be able to match coefficients of the same order of r, and arbitrarily set the normalisation of the waves to have $A_0 = B_0 = 1$ (note that $A_n = B_n$ if one includes only the $1/r^3$ term in the potential).

The $n = 0$ equations have, using the notation given in Ref. [96], four values for a_0, corresponding to attractive

$$\begin{aligned} &\text{(1A):}\ \ a_0 = -4i,\ \ w_0 = \frac{u_0}{\sqrt{2}} \\ &\text{(2A):}\ \ a_0 = +4i,\ \ w_0 = \frac{u_0}{\sqrt{2}} \end{aligned} \tag{4.17}$$

and repulsive solutions

$$\begin{aligned} &\text{(1R):}\ \ a_0 = +4\sqrt{2},\ \ w_0 = -\sqrt{2}u_0 \\ &\text{(2R):}\ \ a_0 = -4\sqrt{2},\ \ w_0 = -\sqrt{2}u_0. \end{aligned} \tag{4.18}$$

[5] Ignoring potential terms that are order r^{-2}, r^{-1}, ..., and the p^2 term, which is classed as order r^0.

The $n = 1$ equations are

$$\begin{aligned} \frac{1}{4}a_0^2 u_0 A_1 + 4\sqrt{2} w_0 B_1 - \left(a_0 a_1 - \frac{3}{4}a_0\right) u_0 A_0 = 0 \\ \frac{1}{4}a_0^2 w_0 B_1 - 4 w_0 B_1 + 4\sqrt{2} u_0 A_1 - \left(a_0 a_2 - \frac{3}{4}a_0\right) w_0 B_0 = 0, \end{aligned} \tag{4.19}$$

which require setting $a_1 = a_2 = 3/4$ and $A_1 = B_1$ for compatibility with the $n = 0$ pair of equations.

To determine the values for A_1 and B_1, we need to look at the $n = 2$ pairs of equations. This interesting feature, that to determine the coefficients at a particular order, say n, one has to go to an order $n + 1$, was mentioned by Valderrama and Arriola in Ref. [96] who state that it is due to the coupled nature of the problem, which means one has the freedom to solve either for u or for w to a given order in the expansion. Back to the problem at hand, the $n = 2$ equations (for the $1/r^3$ potential only) are

$$\begin{aligned} \frac{1}{4}a_0^2 u_0 A_2 + 4\sqrt{2} w_0 B_2 - \frac{1}{2}a_0 u_0 A_1 - a_1 (a_1 - 1) u_0 A_0 = 0 \\ \frac{1}{4}a_0^2 w_0 B_2 - 4 w_0 B_2 + 4\sqrt{2} u_0 A_2 - \frac{1}{2}a_0 w_0 B_1 - a_2 (a_2 - 1) w_0 B_0 = 0. \end{aligned} \tag{4.20}$$

To determine A_1 and B_1 from these we need to remove the other unknown coefficients, A_2 and B_2, from the picture. This is done by using the $n = 0$ equations to form terms in the above that are proportional to $B_2 - A_2$ in the first equation and $A_2 - B_2$ in the second equation, one can then simply add the two equations together and rearrange for $A_1 = B_1$. The process continues in the same fashion to obtain higher order coefficients, and the end result is a power series form for the equations given in Ref. [81].

However, the goal was to improve upon these solutions, which means including higher order terms in the expanded potentials (Eqs. (4.9) and (4.10)), the centrifugal potential term and the p^2 term. Each extra term included effectively generates a new set of coefficients, although the method, as described above, is unchanged. The first extra term to be included is the order-$1/r^2$ centrifugal potential piece which appears in the $n \geq 2$ equations, order-$1/r$ terms appear in the $n \geq 4$ equations, and so on.

Once the coefficients have been obtained to the desired order, the short-distance wave functions can be written as a combination of attractive and repulsive parts (c.f. the inverse of Eq. (4.14)), which we write in the form[6]:

$$\begin{pmatrix} u_l(r) \\ w_l(r) \end{pmatrix} = \begin{pmatrix} \sqrt{2}F_A(r) & -F_R(r) \\ G_A(r) & \sqrt{2}G_R(r) \end{pmatrix} \begin{pmatrix} C_A \\ C_{2R} \end{pmatrix}, \tag{4.21}$$

where

$$\begin{aligned} F_A(r) &= \frac{2}{\sqrt{3}} \left(\frac{r}{R}\right)^{3/4} [f_{1A}^{Re}(r)\cos(4\sqrt{R/r} - \psi) + f_{1A}^{Im}(r)\sin(4\sqrt{R/r} - \psi)] \\ G_A(r) &= \frac{2}{\sqrt{3}} \left(\frac{r}{R}\right)^{3/4} [g_{1A}^{Re}(r)\cos(4\sqrt{R/r} - \psi) + g_{1A}^{Im}(r)\sin(4\sqrt{R/r} - \psi)] \\ F_R(r) &= \frac{1}{\sqrt{3}} \left(\frac{r}{R}\right)^{3/4} f_{2R}(r) e^{-4\sqrt{2}\sqrt{R/r}} \\ G_R(r) &= \frac{1}{\sqrt{3}} \left(\frac{r}{R}\right)^{3/4} g_{2R}(r) e^{-4\sqrt{2}\sqrt{R/r}}. \end{aligned} \tag{4.22}$$

In Eq. (4.21), C_A and C_{2R} are just constants multiplying the attractive and repulsive solutions (though only the ratio of these matters). The coefficients of the various power series functions, f_{1A}, g_{1A}, f_{2R} and g_{2R}, in Eq. (4.22), are presented in Appendix C. We have also used $C_{1A} = C_A e^{i\psi}$ and $C_{2A} = C_A e^{-i\psi}$ and written $f_{1A} = f_{1A}^{Re} + i f_{1A}^{Im}$ and $g_{1A} = g_{1A}^{Re} + i g_{1A}^{Im}$. Finally, ψ is the short-distance phase parameter. It is an energy-independent parameter that fixes the phase of the oscillations in the short-distance wave functions. As such, it plays a similar role to that of the leading energy-independent term in the effective short-range potential, leading to a redundancy between the two. Higher (energy-dependent) terms in the effective potential, however, purely represent the short-range physics that cause them. As discussed by Birse in Ref. [81] regarding uncoupled spin-triplet waves, one can set ψ to zero, but only for waves with weak scattering, therefore removing the redundancy, and letting the effective potential solely represent the short-range physics. The ${}^3S_1 - {}^3D_1$ waves scatter strongly, therefore a non-zero value is taken. By including ψ in this manner it is equivalent to treating the leading term in the effective potential non-perturbatively.

[6]Note that we have discarded the (1R) solution (see Eq. (4.18)) on grounds of normalisability of the wave function at $r = 0$.

Now that we have a handle on the forms of the $S-D$ channel wave functions at small distances, we are now in the position to discuss the large r region. We have to choose between different parametrisations for the coupled-channel scattering matrix, S. Two popular parametrisations are the 'eigenphase' parametrisation of Blatt and Biedenharn (BB)[7] [98]

$$S = \begin{pmatrix} \cos\epsilon_J & -\sin\epsilon_J \\ \sin\epsilon_J & \cos\epsilon_J \end{pmatrix} \begin{pmatrix} e^{2i\delta_{J-1}} & 0 \\ 0 & e^{2i\delta_{J+1}} \end{pmatrix} \begin{pmatrix} \cos\epsilon_J & \sin\epsilon_J \\ -\sin\epsilon_J & \cos\epsilon_J \end{pmatrix}, \tag{4.23}$$

and the 'nuclear-bar' parametrisation of Stapp, Ypsilantis and Metropolis (SYM) [99]

$$S = \begin{pmatrix} e^{i\bar{\delta}_{J-1}} & 0 \\ 0 & e^{i\bar{\delta}_{J+1}} \end{pmatrix} \begin{pmatrix} \cos 2\bar{\epsilon}_J & i\sin 2\bar{\epsilon}_J \\ i\sin 2\bar{\epsilon}_J & \cos 2\bar{\epsilon}_J \end{pmatrix} \begin{pmatrix} e^{i\bar{\delta}_{J-1}} & 0 \\ 0 & e^{i\bar{\delta}_{J+1}} \end{pmatrix}. \tag{4.24}$$

These two parametrisations satisfy the constraints that the scattering matrix must be unitary (in elastic scattering) and symmetric. As we know, it is the tensor OPE force that couples the S and D waves together. The eigenphase parametrisation corresponds to having an unchanged ratio of S:D waves before and after the collision. There are two such states, denoted α and β. The α and β waves correspond to predominantly S-type and D-type, respectively.

Now, as mentioned by SYM [99], the bar parametrisation could be regarded as being more "natural" in the sense that the mixing angle truly represents the amount of mixing between the waves. This is because for the bar waves, the incoming wave is in a single channel and the admixture of the second channel appearing in the outgoing waves is determined solely by the mixing parameter. This is not true for the eigenphase parametrisation. The mixing angle in this representation can become large when the phase shifts become small. Nevertheless, we choose to work in the eigenphase parametrisation, mainly because it makes life easier to calculate a residual interaction matrix. If desired one can convert between the eigen and bar representations, using the following formulas

[7]Note: Strictly speaking one should not use J to label the phase shifts and mixing angles in the eigen parametrisation, only for energies tending to zero is this correct.

$$\delta_{J+1} + \delta_{J-1} = \bar{\delta}_{J+1} + \bar{\delta}_{J-1}$$

$$\sin(\bar{\delta}_{J-1} - \bar{\delta}_{J+1}) = \frac{\tan(2\bar{\epsilon}_J)}{\tan(2\epsilon_J)}$$

$$\sin(\delta_{J-1} - \delta_{J+1}) = \frac{\sin(2\bar{\epsilon}_J)}{\sin(2\epsilon_J)}, \tag{4.25}$$

where the barred-parameters correspond to, not surprisingly, the bar phase shifts and mixing angle.

Working in the eigenphase (or simply eigen) basis of BB, we build, what we now call, distorted eigen waves of the long-range OPE potential, by constructing two independent pairs of solutions, $(u_{l,1},\ w_{l,1})$ and $(u_{l,2},\ w_{l,2})$, of the coupled radial Schrödinger equations describing nucleon-nucleon scattering at leading-order. These are then used to form linear combinations that generate the two pairs of eigen waves: $(u_{l,\alpha},\ w_{l,\alpha})$ and $(u_{l,\beta},\ w_{l,\beta})$.

To start with let us write down the forms of the eigen waves (for general waves with total angular momentum J) in the limit $r \to \infty$ as [98]

$$\begin{aligned}
u_{J,\alpha}(r) &\to \cos\epsilon_j \sin(pr - \frac{1}{2}(J-1)\pi + \delta_{J,\alpha}) \\
w_{J,\alpha}(r) &\to \sin\epsilon_j \sin(pr - \frac{1}{2}(J+1)\pi + \delta_{J,\alpha}) \\
u_{J,\beta}(r) &\to -\sin\epsilon_j \sin(pr - \frac{1}{2}(J-1)\pi + \delta_{J,\beta}) \\
w_{J,\beta}(r) &\to \cos\epsilon_j \sin(pr - \frac{1}{2}(J+1)\pi + \delta_{J,\beta}),
\end{aligned} \tag{4.26}$$

where one can see that each pair of eigen waves has the same phase shift. With these in mind, we build our eigen solutions from two independent pairs of solutions by writing, for the u eigen wave,

$$\begin{aligned}
Cu_{l,1} + Du_{l,2} &= \frac{CA_1 \sin(pr - \frac{1}{2}(J-1)\pi + \delta_{u_1})}{p} + \frac{DA_2 \sin(pr - \frac{1}{2}(J-1)\pi + \delta_{u_2})}{p} \\
&= \frac{E \sin(pr - \frac{1}{2}(J-1)\pi + \delta)}{p}
\end{aligned} \tag{4.27}$$

and for the w eigen wave,

$$Cw_{l,1} + Dw_{l,2} = \frac{CB_1 \sin(pr - \frac{1}{2}(J+1)\pi + \delta_{w_1})}{p} + \frac{DB_2 \sin(pr - \frac{1}{2}(J+1)\pi + \delta_{w_2})}{p}$$
$$= \frac{F \sin(pr - \frac{1}{2}(J+1)\pi + \delta)}{p}, \tag{4.28}$$

where C, D, E and F are amplitudes we want to find out, δ is the eigen phase (α or β), A_1, B_1, A_2 and B_2 are the amplitudes of the two pairs of independent solutions and δ_{u_1}, δ_{w_1}, δ_{u_2} and δ_{w_2} are their phase shifts. The parameters mentioned here that are related to the independent solutions are known prior to the construction of the eigen waves, and are obtained by comparing the distorted waves with the free ones in the asymptotic region, as was done in the previous chapter for the ${}^1P_1$ wave.

Before showing how to determine the amplitudes C and D, it should be mentioned that we actually only require the ratio $\frac{C}{D}$. This is because if we know $\frac{C}{D}$ we can set, for instance, $D = 1$ and obtain a value for C, we can then use normalization constraints to determine the correct values of C and D.

Dividing Eq. (4.27) through by D and rearranging one can write

$$\frac{C}{D} = \frac{\frac{E}{D} \sin(pr - \frac{1}{2}(J-1)\pi + \delta) - A_2 \sin(pr - \frac{1}{2}(J-1)\pi + \delta_{u_2})}{A_1 \sin(pr - \frac{1}{2}(J-1)\pi + \delta_{u_1})}. \tag{4.29}$$

Also, using the equations given in Appendix A, we can write for the u-waves

$$E \sin(\delta - \delta_{u_1}) = DA_2 \sin(\delta_{u_2} - \delta_{u_1}), \tag{4.30}$$

and for the w-waves

$$F \sin(\delta - \delta_{w_1}) = DB_2 \sin(\delta_{w_2} - \delta_{w_1}). \tag{4.31}$$

Inserting Eq. (4.30) into Eq. (4.29) we can remove the factor E/D. Now, it is not clear that the resulting equation for $\frac{C}{D}$ is independent of pr. However, ensuring that the phase shifts and amplitudes are extracted in the asymptotic region, this must be the case. This is shown by invoking two trigonometric identities in succession ((i) $\sin x \sin y = \frac{1}{2}(\cos(x-y) - \cos(x+y))$ and (ii) $\cos x - \cos y = -2 \sin \frac{1}{2}(x+y) \sin \frac{1}{2}(x-y)$) which are used to remove all factors of pr, giving

$$\frac{C}{D} = \frac{A_2 \sin(\delta - \delta_{u_2})}{A_1 \sin(\delta_{u_1} - \delta)}. \tag{4.32}$$

The same can be done for the w-waves (using Eqs. (4.28) and (4.31)), giving

$$\frac{C}{D} = \frac{B_2 \sin(\delta - \delta_{w_2})}{B_1 \sin(\delta_{w_1} - \delta)}. \tag{4.33}$$

The two equations are combined to give

$$A_2 B_1 \sin(\delta - \delta_{u_2}) \sin(\delta_{w_1} - \delta) = A_1 B_2 \sin(\delta - \delta_{w_2}) \sin(\delta_{u_1} - \delta), \tag{4.34}$$

which can be written as the following quadratic in $\tan\delta$ by using $\sin(A - B) = -\sin A \cos B - \cos A \sin B$ and dividing through by $\cos^2\delta$:

$$\begin{aligned} \tan^2\delta \left[A_1 B_2 \cos\delta_{w_2} \cos\delta_{u_1} - A_2 B_1 \cos\delta_{u_2} \cos\delta_{w_1}\right] \; + \\ \tan\delta \left[A_2 B_1 \sin(\delta_{w_1} + \delta_{u_2}) - A_1 B_2 \sin(\delta_{u_1} + \delta_{w_2})\right] \; + \\ \left[A_1 B_2 \sin\delta_{w_2} \sin\delta_{u_1} - A_2 B_1 \sin\delta_{u_2} \sin\delta_{w_1}\right] \; = \; 0. \end{aligned} \tag{4.35}$$

The two solutions to this quadratic equation give us the eigen phase shifts we require: $\delta_{\alpha,l}$ and $\delta_{\beta,l}$. Dividing Eq. (4.30) by Eq. (4.31) and equating the result to the relevant ratio of waves in Eq. (4.26) , the mixing angle ϵ_J is given by

$$\begin{aligned} \frac{E}{F} \; &= \; \frac{A_2 \sin(\delta_{u_2} - \delta_{u_1}) \sin(\delta - \delta_{w_1})}{B_2 \sin(\delta_{w_2} - \delta_{w_1}) \sin(\delta - \delta_{u_1})} \\ &= \; \cot\epsilon_J \text{ if } \delta \; = \; \delta_\alpha \\ &= \; -\tan\epsilon_J \text{ if } \delta \; = \; \delta_\beta. \end{aligned} \tag{4.36}$$

At this point we do not know which eigen wave corresponds to $L = J + 1$ or $L = J - 1$, since we are free to interchange α and β (as long a we simultaneously set $\epsilon_J \to \epsilon_J + \frac{\pi}{2}$). In the limit where the interaction energy tends to zero the states α and β becomes eigenstates, due to the effects of the centrifugal barrier. Remembering the forms of the eigen waves $r \to \infty$ (see Eq. (4.26)) we see that the two eigenstates correspond to choosing $\epsilon_J \to 0$ or $\epsilon_J \to \frac{\pi}{2}$. Following Blatt and Biedenharn [98], we choose α to correspond to waves that are predominantly

$L = J - 1$ and β to correspond to waves that are predominantly $L = J + 1$. This means that in the limit where the energy tends to zero we choose $\epsilon_J \to 0$ rather than $\epsilon_J \to \frac{\pi}{2}$.

One should note that, in practice, the actual order of implementation of these equations to determine the eigen solutions numerically is different to that given here (it sort of works in reverse). More specifically, after generating two independent pairs of solutions by choosing different combinations of the ratio C_A/C_{2R} and integrating in the direction away from the origin, eigen phases are extracted directly using Eq. (4.35), while the mixing angle is determined from Eq. (4.36). Then either C or D is set to 1 and the remaining unknown coefficient is determined from Eq. (4.32) or Eq. (4.33). The waves are then normalised by dividing through by $\sqrt{E^2 + F^2}$. Only once the correct values of C and D are obtained can the distorted eigen waves be built. In other words, the eigen phase shifts are extracted before the distorted eigen waves are even constructed, i.e. they are not extracted from the distorted eigen waves themselves.

Finally, the short-distance phase parameter ψ (see Eq. (4.22)) is determined by fixing the eigen phase shift corresponding to the S-wave ($\delta_{\alpha,l}$) to the $^3S_1$ np scattering length at zero energy, a, which is defined from the first term in the effective-range-expansion,

$$a = -\frac{\tan(\delta)}{p}. \tag{4.37}$$

Once ψ has been determined, the resulting eigen phase shifts can be subtracted from the empirical phase shifts and used to build a residual interaction matrix.

4.1.2 Effective Residual Interaction Matrix

Instead of extracting a single residual interaction strength as done for the uncoupled $^1P_1$ partial wave in the previous chapter, because we are dealing with coupled waves we aim to extract a residual interaction matrix. This interaction matrix can then be used as an input to determine deuteron wave functions and observables (as shown in the next chapter).

To obtain a coupled-channel form for Eq. (3.13) we use a method described by Rodberg and Thaler [100]. Before applying the method to the coupled waves, we demonstrate it first in a simpler scenario by using it to derive Eq. (3.13) for uncoupled, spin-singlet waves with $L > 0$.

One starts by writing down two radial Schrödinger equations. The first is written as

$$\left(-\frac{\mathrm{d}^2}{\mathrm{d}r^2}+\frac{L(L+1)}{r^2}+MV_l(r)\right)u_l(p,r)=p^2u_l(p,r), \tag{4.38}$$

which describes the scattering of two nucleons, interacting through a long-range potential, $V_l(r)$, and, for spin-singlet waves where $V_{\pi T}(r)=0$, is identical to Eq. (3.1) (though in Eq. (4.38) we have used the 'reduced' wave function notation where u_l is related to ψ_l by $\psi_l=u_l/r$). The potential, $V_l(r)$, although described as long-range, must fall off faster than the centrifugal potential as $r\to\infty$. In the context of our demonstration, we define $V_l(r)=V_{\pi C}(r)$ and therefore this requirement is satisfied. The solution $u_l(p,r)$ is the so-called 'comparison' solution for the method.

We write the second Schrödinger equation as

$$\left(-\frac{\mathrm{d}^2}{\mathrm{d}r^2}+\frac{L(L+1)}{r^2}+M\left[V_l(r)+V_s(p,r)\right]\right)u(p,r)=p^2u(p,r). \tag{4.39}$$

It describes the scattering for the full problem, where our potential is now a sum of two parts, long and short: $V(p,r)=V_l(r)+V_s(p,r)$, where $V_s(p,r)$ is defined in Eq. (3.12). Again the potential must fall off faster than r^{-2} as $r\to\infty$.

Now the essence of the method is to construct a Wronskian defined as $W(u_l,u)=u_lu'-uu'_l$, where the prime ($'$) denotes the derivative with respect to the radial coordinate. Multiplying Eq. (4.38) by $u(p,r)$ and Eq. (4.39) by $u_l(p,r)$, and subtracting the latter from the former, one obtains, after integrating,

$$\begin{aligned}W(u_l(p,r),u(p,r))&=\left[u_l(p,r)u'(p,r)-u(p,r)u'_l(p,r)\right]\Big|_{r=0}^{r=\infty}\\&=M\int_0^\infty u_l(p,r)V_s(p,r)u(p,r)\,\mathrm{d}r.\end{aligned} \tag{4.40}$$

Notice that already the RHS of Eq. (4.40) is close to the form that we want, i.e. it is nearly (barring the $u(p,r)$) equivalent to a matrix element of a short-range potential between distorted waves of the long-range potential.

Regarding the LHS, in uncoupled spin-singlet waves the Wronskian can be

evaluated with ease. For the lower limit, we are free to choose the regular solution over the irregular solution for $u_l(p,r)$, which has a radial dependence which goes like r^{L+1} for $r \to 0$. This automatically means that the Wronskian evaluated in the lower limit is zero, as both $u_l(p,r)$ and $u'_l(p,r)$ are zero at $r = 0$.

Turning to the upper limit, particular choices of normalisation for $u_l(p,r)$ and $u(p,r)$ result in different forms for the result. For instance, choosing the normalisations for the two solutions as

$$u_l(p,r) \xrightarrow{r\to\infty} e^{i\delta_l} \sin(pr - \frac{L\pi}{2} + \delta_l) \tag{4.41}$$

and

$$u(p,r) \xrightarrow{r\to\infty} e^{i\delta} \sin(pr - \frac{L\pi}{2} + \delta), \tag{4.42}$$

results in a residual T-matrix form:

$$T_s(p) = e^{2i\delta_l} e^{i\delta_s} \sin(\delta_s) = -\frac{M}{p} \int_0^\infty u_l(p,r) V_s(p,r) u(p,r)\, \mathrm{d}r, \tag{4.43}$$

where we have defined $\delta_s = \delta - \delta_l$, corresponding to the phase shift resulting from the extra potential, $V_s(p,r)$.

Alternatively, one can define the normalisations as

$$u_l(p,r) \xrightarrow{r\to\infty} \frac{1}{p} \sin(pr - \frac{L\pi}{2} + \delta_l) \tag{4.44}$$

and

$$u(p,r) \xrightarrow{r\to\infty} \frac{1}{p} \sin(pr - \frac{L\pi}{2} + \delta) \tag{4.45}$$

corresponding to standing-wave boundary conditions. This results in the following:

$$\sin(\delta_s) = -Mp \int_0^\infty u_l(p,r) V_s(p,r) u(p,r)\, \mathrm{d}r. \tag{4.46}$$

Now this is not quite in the correct form to compare with Eq. (3.13) because of the presence of $u(p,r)$ on the RHS. At this point we leave the method described by Rodberg and Thaler and proceed with the goal to replace $u(p,r)$ with $u_l(p,r)$, by using the distorted-wave Born approximation.

With this in mind we write in the limit $r \to \infty$

$$\begin{aligned} u(p,r) &\to \frac{1}{p}\sin(pr - \frac{L\pi}{2} + \delta) \\ &\to \frac{1}{p}\sin(pr - \frac{L\pi}{2} + \delta_l + \delta_s) \\ &\to \frac{1}{p}\sin(pr - \frac{L\pi}{2} + \delta_l)\cos(\delta_s) + \frac{1}{p}\cos(pr - \frac{L\pi}{2} + \delta_l)\sin(\delta_s). \end{aligned} \tag{4.47}$$

Ignoring the term on the right-hand-side which involves $\sin(\delta_s)$ (since multiplying $V_s(p,r)$ by $\sin(\delta_s)$ is second-order in the approximation) we can write

$$u(p,r) \to u_l(p,r)\cos(\delta_s), \tag{4.48}$$

which inserting into the Eq. (4.46) and dividing through by $\cos(\delta_s)$ results in a residual K-matrix structure

$$K_s(p) = -\frac{1}{Mp}\tan(\delta_s) = \int_0^\infty u_l(p,r)V_s(p,r)u_l(p,r)\,\mathrm{d}r. \tag{4.49}$$

After using the definition in Eq. (3.12) for $V_s(p,r)$, Eq. (4.49) and Eq. (3.13) are directly related to one another (up to a factor of 4π).

We are now in the position to apply the method to the more complex problem of coupled partial waves.

The radial coupled Schrödinger equation in matrix form, whose solutions are the distorted waves of the long range potential that act as the comparison solutions, is:

$$\begin{pmatrix} -\frac{1}{M}\frac{\mathrm{d}^2}{\mathrm{d}r^2} + V_{SS} & V_{SD} \\ V_{DS} & -\frac{1}{M}\frac{d^2}{dr^2} + V_{DD} + \frac{6}{Mr^2} \end{pmatrix} \begin{pmatrix} u_l \\ w_l \end{pmatrix} = \frac{p^2}{M}\begin{pmatrix} u_l \\ w_l \end{pmatrix} \tag{4.50}$$

where we have used the following definitions:

$$
\begin{aligned}
V_{SS}(r) &= \frac{U_{\pi C}(r)}{M} \\
V_{SD}(r) &= \frac{2\sqrt{2}U_{\pi T}(r)}{M} \\
V_{DD}(r) &= \frac{U_{\pi C}(r) - 2U_{\pi T}(r)}{M}.
\end{aligned} \tag{4.51}
$$

Similarly, the radial coupled Schrödinger equation in matrix form for the full problem is given by:

$$
\begin{pmatrix}
-\frac{1}{M}\frac{\mathrm{d}^2}{\mathrm{d}r^2} + V_{SS} + V_{SS}^s & V_{SD} + V_{SD}^s \\
V_{DS} + V_{DS}^s & -\frac{1}{M}\frac{d^2}{dr^2} + V_{DD} + V_{DD}^s + \frac{6}{Mr^2}
\end{pmatrix}
\begin{pmatrix} u \\ w \end{pmatrix}
= \frac{p^2}{M}
\begin{pmatrix} u \\ w \end{pmatrix}, \tag{4.52}
$$

where $V_{SS}^s(p,r)$, $V_{SD}^s(p,r)$, $V_{DS}^s(p,r)$ and $V_{DD}^s(p,r)$ denote the various short-ranged potentials parametrising the additional scattering between the distorted waves.

Eqs. (4.50) and (4.52) can be written in more compact forms as

$$
-\frac{1}{M}\underline{\mathbf{u}}_l'' + \frac{1}{M}\frac{\mathbf{L}(\mathbf{L}+\mathbf{1})}{r^2}\underline{\mathbf{u}}_l + \mathbf{V}\underline{\mathbf{u}}_l = \frac{p^2}{M}\underline{\mathbf{u}}_l \tag{4.53}
$$

and

$$
-\frac{1}{M}\underline{\mathbf{u}}'' + \frac{1}{M}\frac{\mathbf{L}(\mathbf{L}+\mathbf{1})}{r^2}\underline{\mathbf{u}} + \mathbf{V}\underline{\mathbf{u}} + \mathbf{V^s}\underline{\mathbf{u}} = \frac{p^2}{M}\underline{\mathbf{u}}, \tag{4.54}
$$

where we have defined the following matrices for the waves as

$$
\underline{\mathbf{u}}_l = \begin{pmatrix} u_l \\ w_l \end{pmatrix} = \begin{pmatrix} u_{l,\alpha} & u_{l,\beta} \\ w_{l,\alpha} & w_{l,\beta} \end{pmatrix} \begin{pmatrix} C_\alpha \\ C_\beta \end{pmatrix} = \mathbf{u}_l\underline{\mathbf{C}} \tag{4.55}
$$

and

$$
\underline{\mathbf{u}} = \begin{pmatrix} u \\ w \end{pmatrix} = \begin{pmatrix} u_\alpha & u_\beta \\ w_\alpha & w_\beta \end{pmatrix} \begin{pmatrix} D_\alpha \\ D_\beta \end{pmatrix} = \mathbf{u}\underline{\mathbf{D}}, \tag{4.56}
$$

the following matrices for the scattering potentials as

$$\mathbf{V}(\mathbf{r}) = \begin{pmatrix} V_{SS}(r) & V_{SD}(r) \\ V_{DS}(r) & V_{DD}(r) \end{pmatrix} \tag{4.57}$$

and

$$\mathbf{V^s}(\mathbf{p},\mathbf{r}) = \begin{pmatrix} V^s_{SS}(p,r) & V^s_{SD}(p,r) \\ V^s_{DS}(p,r) & V^s_{DD}(p,r) \end{pmatrix} \tag{4.58}$$

and the matrix for the centrifugal potentials as

$$\mathbf{L} = \mathbf{L}(J) = \begin{pmatrix} J-1 & 0 \\ 0 & J+1 \end{pmatrix}, \tag{4.59}$$

where $J = 1$ for the $S - D$ waves.

Following the method demonstrated above for uncoupled spin-singlet waves, we proceed here by constructing a Wronskian of matrices, which is defined as $\mathbf{W}(\underline{\mathbf{u}}_l, \underline{\mathbf{u}}) = \underline{\mathbf{u}}_l^\top \underline{\mathbf{u}}' - \underline{\mathbf{u}}_l'^\top \underline{\mathbf{u}}$, where we have assumed that the wave functions have a normalisation that corresponds to standing wave boundary conditions, i.e. they are real and of the form given in Eq. (4.26) for $r \to \infty$. Taking the transpose of Eq. (4.56), multiplying it on the right by $\underline{\mathbf{u}}$, and subtracting from it Eq. (4.55) multiplied on the left by $\underline{\mathbf{u}}_l^\top$, one gets, after integrating from $r = 0$ to $r = \infty$

$$\frac{1}{M}\left(\underline{\mathbf{u}}_l^\top \underline{\mathbf{u}}' - \underline{\mathbf{u}}_l'^\top \underline{\mathbf{u}}\right)\Big|_{r=0}^{r=\infty} = \int_0^\infty \underline{\mathbf{u}}_l^\top \mathbf{V}^s \underline{\mathbf{u}}\, \mathrm{d}r, \tag{4.60}$$

where we have used $[\mathbf{L}(\mathbf{L}+\mathbf{1})]^\top = \mathbf{L}(\mathbf{L}+\mathbf{1})$ and $\mathbf{V}^\top = \mathbf{V}$. By inserting Eqs. (4.55) and (4.56) into Eq. (4.60), it can be simplified to

$$\frac{1}{M}\left(\mathbf{u}_l^\top \mathbf{u}' - \mathbf{u}_l'^\top \mathbf{u}\right)\Big|_{r=0}^{r=\infty} = \int_0^\infty \mathbf{u}_l^\top \mathbf{V}^s \mathbf{u}\, \mathrm{d}r, \tag{4.61}$$

where we have replaced $\underline{\mathbf{u}}_l$ with $\mathbf{u}_l$ and $\underline{\mathbf{u}}$ with $\mathbf{u}$. Written in this form we now evaluate the left-hand-side of Eq. (4.61) in the limits $r = 0$ and $r = \infty$.

To show that the lower limit ($r = 0$) is zero, we write

$$\begin{aligned} \mathbf{u}_l(p,r) &= \begin{pmatrix} u_{l,\alpha}(p,r) & u_{l,\beta}(p,r) \\ w_{l,\alpha}(p,r) & w_{l,\beta}(p,r) \end{pmatrix} \\ &\xrightarrow{r\to 0} \begin{pmatrix} \sqrt{2}F_A(p,r) & -F_R(p,r) \\ G_A(p,r) & \sqrt{2}G_R(p,r) \end{pmatrix} \begin{pmatrix} C_{A\alpha}(p) & C_{A\beta}(p) \\ C_{R\alpha}(p) & C_{R\beta}(p) \end{pmatrix} \end{aligned} \tag{4.62}$$

and

$$\begin{aligned}\mathbf{u}(p,r) &= \begin{pmatrix} u_\alpha(p,r) & u_\beta(p,r) \\ w_\alpha(p,r) & w_\beta(p,r) \end{pmatrix} \\ &\xrightarrow{r\to 0} \begin{pmatrix} \sqrt{2}F_A(p,r) & -F_R(p,r) \\ G_A(p,r) & \sqrt{2}G_R(p,r) \end{pmatrix} \begin{pmatrix} D_{A\alpha}(p) & D_{A\beta}(p) \\ D_{R\alpha}(p) & D_{R\beta}(p) \end{pmatrix}, \end{aligned} \tag{4.63}$$

where we have used the form of the short-distance wave functions in Eq. (4.21), and defined for the distorted waves of the known long-range potential the following pairs of coefficients,

(i) for the alpha-waves:

$$\begin{pmatrix} C_{A\alpha} \\ C_{R\alpha} \end{pmatrix} = C_\alpha \begin{pmatrix} C_{A_1} \\ C_{2R_1} \end{pmatrix} + D_\alpha \begin{pmatrix} C_{A_2} \\ C_{2R_2} \end{pmatrix} \tag{4.64}$$

(i) for the beta-waves:

$$\begin{pmatrix} C_{A\beta} \\ C_{R\beta} \end{pmatrix} = C_\beta \begin{pmatrix} C_{A_1} \\ C_{2R_1} \end{pmatrix} + D_\beta \begin{pmatrix} C_{A_2} \\ C_{2R_2} \end{pmatrix}, \tag{4.65}$$

where the subscripts (1 and 2) correspond to the two pairs of independent solutions that are used to construct our distorted eigen waves. Notice that Eqs. (4.62) and (4.63) have the same structure and differ only by their respective sets of coefficients. This is because within the delta-shell radius R_0 only leading-order OPE is present. The shorter-range potentials (such as TPE, etc.) arise at higher orders in the chiral power counting and are therefore treated as perturbations. This means that their singularities are smeared out (regularised) by the delta-shell potential. So, inserting Eqs. (4.62) and (4.63) into Eq. (4.61) and using the fact that $F_A \to G_A$ and $F_R \to G_R$ as $r \to 0$, we can show that the lower limit is zero.

For the upper limit ($r = \infty$), we write the eigen waves in the forms (c.f. Eq. (4.26))

$\mathbf{u}_l(p,r) \xrightarrow{r\to\infty}$

$$\frac{1}{p} \begin{pmatrix} \cos\epsilon_l \sin(pr + \delta_{\alpha,l}) & -\sin\epsilon_l \sin(pr + \delta_{\beta,l}) \\ \sin\epsilon_l \sin(pr - \pi + \delta_{\alpha,l}) & \cos\epsilon_l \sin(pr - \pi + \delta_{\beta,l}) \end{pmatrix} \tag{4.66}$$

and

$$\mathbf{u}(p,r) \xrightarrow{r\to\infty} \frac{1}{p}\begin{pmatrix} \cos\epsilon\sin(pr+\delta_\alpha) & -\sin\epsilon\sin(pr+\delta_\beta) \\ \sin\epsilon\sin(pr-\pi+\delta_\alpha) & \cos\epsilon\sin(pr-\pi+\delta_\beta)\end{pmatrix}. \tag{4.67}$$

Inserting these into Eq. (4.61) gives:

$$\int_0^\infty \mathbf{u}_l^\top\, \mathbf{V}^s\mathbf{u}\, \mathrm{d}r = -\frac{1}{Mp}\begin{pmatrix} \cos(\Delta\epsilon)\sin(\Delta_{\alpha\alpha}) & -\sin(\Delta\epsilon)\sin(\Delta_{\beta\alpha}) \\ \sin(\Delta\epsilon)\sin(\Delta_{\alpha\beta}) & \cos(\Delta\epsilon)\sin(\Delta_{\beta\beta})\end{pmatrix} \tag{4.68}$$

where we have made the following definitions: $\Delta\epsilon = \epsilon - \epsilon_l$, $\Delta_{\alpha\alpha} = \delta_\alpha - \delta_{\alpha,l}$, $\Delta_{\alpha\beta} = \delta_\alpha - \delta_{\beta,l}$, $\Delta_{\beta\alpha} = \delta_\beta - \delta_{\alpha,l}$ and $\Delta_{\beta\beta} = \delta_\beta - \delta_{\beta,l}$. Note that if one normalises the wave functions in a similar form to Eqs. (4.41) and (4.42) in the uncoupled case, i.e. including exponential phase factors explicitly, a connection can be made between the resulting Wronskian in the limit $r \to \infty$ and the residual scattering matrix $\tilde{S}$, thus providing a check that everything is in order (See Appendix B).

Now we apply the distorted-wave Born approximation to replace $\mathbf{u}$ on the RHS of $\mathbf{V}^s(p,r)$ in Eq. (4.68) with $\mathbf{u}_l$. As in the uncoupled spin-singlet method above, we examine the waves in the large-r region and look for small quantities that when multiplied by $\mathbf{V}^s(p,r)$ are classed as second order (or higher) in the approximation and so are discarded. Therefore, inserting $\epsilon = \Delta\epsilon + \epsilon_l$, $\delta_\alpha = \Delta_{\alpha\alpha} + \delta_{\alpha,l}$ and $\delta_\beta = \Delta_{\beta\beta} + \delta_{\beta,l}$ into Eq. (4.67), and using

$$\begin{aligned}
\cos(\Delta\epsilon+\epsilon_l) &= \cos\Delta\epsilon\cos\epsilon_l - \cancel{\sin\Delta\epsilon\sin\epsilon_l} \\
\sin(\Delta\epsilon+\epsilon_l) &= \cancel{\sin\Delta\epsilon\cos\epsilon_l} + \cos\Delta\epsilon\sin\epsilon_l \\
\sin(pr+\Delta+\delta_l) &= \sin(pr+\delta_l)\cos\Delta + \cancel{\cos(pr+\delta_l)\sin\Delta} \\
\sin(pr-\pi+\Delta+\delta_l) &= \sin(pr-\pi+\delta_l)\cos\Delta + \cancel{\cos(pr-\pi+\delta_l)\sin\Delta},
\end{aligned} \tag{4.69}$$

discarding the 'slashed' terms (since $\sin x \approx x$ if x is 'small'), gives

$$\mathbf{u} \to \cos\Delta\epsilon\,\mathbf{u}_l\begin{pmatrix}\cos\Delta_{\alpha\alpha} & 0 \\ 0 & \cos\Delta_{\beta\beta}\end{pmatrix}. \tag{4.70}$$

This can be inserted into Eq. (4.68) and after rearranging gives,

$$\int_0^\infty \mathbf{u}_l^\top(p,r)\ \mathbf{V}^s(p,r)\mathbf{u}_l(p,r)\ \mathrm{d}r = \\ -\frac{1}{Mp}\begin{pmatrix} \tan\Delta_{\alpha\alpha}(p) & -\dfrac{\tan\Delta\epsilon(p)\sin\Delta_{\beta\alpha}(p)}{\cos\Delta_{\beta\beta}(p)} \\ \dfrac{\tan\Delta\epsilon(p)\sin\Delta_{\alpha\beta}(p)}{\cos\Delta_{\alpha\alpha}(p)} & \tan\Delta_{\beta\beta}(p) \end{pmatrix}. \tag{4.71}$$

At this point we want to define the effective short-range potential matrix $\mathbf{V}^s(p,r)$ in Eq. (4.71) in such a way that its corresponding residual strength matrix is independent of R_0 for small R_0. In the previous chapter concerning the ${}^1P_1$ wave (and in the uncoupled channels of Refs. [80] and [81] R_0 dependence is removed by dividing out the asymptotic (small-r) form of the radial wave functions in the definition of the effective potential. For the coupled channels we take a similar approach.

To see how the R_0 dependence can be removed from the matrices involved in Eq. (4.71), it is helpful to replace $\mathbf{u_l}(p,r)$ with its small-r form given in Eq. (4.62), which written as $\mathbf{u}_l(p,r) \to \mathbf{F}(p,r)\mathbf{C}(p)$ gives,

$$\mathbf{u}_l^\top(p,r)\ \mathbf{V}^s(p,r)\ \mathbf{u}_l(p,r) \to \\ \left[\mathbf{C}^\top(p)\mathbf{F}^\top(p,r)\right]\mathbf{V}^s(p,r)\left[\mathbf{F}(p,r)\mathbf{C}(p)\right] \tag{4.72}$$

In this form, the R_0 dependence can be 'divided out' by inserting an identity matrix on either side of $\mathbf{V}^s(p,r)$, written as $\mathbf{1} = (\mathbf{F_0}^\top)^{-1}\mathbf{F_0}^\top$ on the LHS, and $\mathbf{1} = \mathbf{F_0}\mathbf{F_0}^{-1}$ on the RHS, where $\mathbf{F_0} = \mathbf{F}(0,R_0)$. Equivalently, they can be used in the definition of the effective potential matrix, which we choose to represent by a delta-shell potential, by writing

$$\begin{aligned}\mathbf{V}^s(p,r) &= \left[(\mathbf{F_0}^\top)^{-1}\mathbf{F_0}^\top\right]\tilde{\mathbf{V}}(p)\left[\mathbf{F_0}\mathbf{F_0}^{-1}\right]\delta\left(r-R_0\right) \\ &= \left(\mathbf{F_0}^\top\right)^{-1}\ \tilde{\mathbf{V}}_{(AR)}(p)\,\mathbf{F_0}^{-1}\,\delta\left(r-R_0\right)\end{aligned} \tag{4.73}$$

where $\tilde{\mathbf{V}}$ is the residual strength matrix in the S-D basis, and we have absorbed the matrices that are directly on either side of it by defining a residual strength matrix in the attractive-repulsive (A-R) basis,

$$\tilde{\mathbf{V}}_{(AR)}(p) = \begin{pmatrix} \tilde{V}_{AA}(p) & \tilde{V}_{AR}(p) \\ \tilde{V}_{RA}(p) & \tilde{V}_{RR}(p) \end{pmatrix} = \mathbf{F_0}^\top \tilde{\mathbf{V}}(p) \mathbf{F_0}. \tag{4.74}$$

Note that, unlike for the ${}^1P_1$ channel, the particular value one can take for the radius of the delta-shell, R_0, in the ${}^3S_1 - {}^3D_1$ waves is rather restricted, although, as before a small value is preferable in order to reduce contributions from cut-off artefacts. These restrictions are elaborated on in the next section.

Using the form for $\mathbf{V}^s(p,r)$ given in Eq. (4.73), Eq. (4.71) becomes, after evaluating the integral and rearranging,

$$\tilde{\mathbf{V}}^{(2)}_{(AR)}(p) = \mathbf{F_0}^\top \left(\mathbf{u}_l^\top\right)^{-1}(p,R_0)\, \tilde{\mathbf{K}}(p)\, \left(\mathbf{u}_l\right)^{-1}(p,R_0)\, \mathbf{F_0}, \tag{4.75}$$

where the superscript (2) implies that long-range forces of order Q^2 and higher are present, and we have used $\tilde{\mathbf{K}}(p)$ to denote the matrix in the RHS of Eq. (4.71).

Finally, we can use the DWBA to subtract the effects of order $Q^{2,3}$ TPE and order Q^2 recoil OPE perturbatively from $\tilde{\mathbf{K}}(p)$, to obtain a residual interaction matrix whose long-range scattering starts at order Q^4

$$\begin{aligned} \tilde{\mathbf{V}}^{(4)}_{(AR)}(p) = \mathbf{F_0}^\top \left(\mathbf{u}_l^\top\right)^{-1}(p,R_0) \times \\ \left(\tilde{\mathbf{K}}(p) - \left\langle \mathbf{u}_l^\top(p) | \mathbf{V}^{(2)}_{1\pi} + \mathbf{V}^{(2,3)}_{2\pi} | \mathbf{u}_l(p) \right\rangle\right)\, \left(\mathbf{u}_l\right)^{-1}(p,R_0)\, \mathbf{F_0}, \end{aligned} \tag{4.76}$$

where the TPE and recoil OPE potentials are now written as matrices, denoted $\mathbf{V}^{(2,3)}_{2\pi}$ and $\mathbf{V}^{(2)}_{1\pi}$ respectively. Now, similar to the ${}^1P_1$ channel, due to the combination of the forms of the wave functions near the origin and the singularities of the potentials, the matrix elements in Eq. (4.76) contain divergences. These must first be made finite, which is done by applying a radial cut-off, R_0, at the same radius as our delta-shell potential matrix in Eq. (4.73), and then second be renormalised by the counterterms that are available for this channel. We are then able to extract a momentum scale that controls the expansion of our EFT.

4.1.3 Choice of Matching Radius and Delta-Shell Radius

There are two radii in the small-r region that are important in a DW analysis of NN scattering, and we shall discuss each in turn. The first, which we denote R_m, is the radius at which one chooses to match the analytical wave function to the

numerical wave function, in order to integrate the radial Schödinger equations and therefore generate numerical solutions (our distorted waves) in regions for which analytical solutions are not possible. To ensure that the corresponding phase shifts and amplitudes extracted at large r are independent of R_m, as they should be, one needs to ensure that the matching point is small enough that the analytical solution is valid. In the ${}^3S_1 - {}^3D_1$ waves (and the ${}^3P_2 - {}^3F_2$ waves in the next section), this has proved rather unexpectedly challenging, at least for the solutions that start off as either purely attractive or with an attractive component.

We demonstrate this in Figs. 4.1 and 4.2, which show the dependence of wave functions at $r = 30$fm starting out as purely repulsive and attractive respectively on the matching radius R_m (at some arbitrary lab kinetic energy $T = 100$ MeV).[8] The different curves correspond to the maximum order of (r/R) included in the short-distance wave functions, defined in Eqs. (4.21) and (4.22). Fig. 4.1 shows that the initially-repulsive wave at $r = 30$fm is, for the most part, independent of R_m. Indeed the "worst" curve ($n = 7/2$) only varies at the 0.01% level over the range shown in the plot, and by including more terms in the short-distance wave functions, the variation is substantially reduced.

Unfortunately, the situation is not quite so satisfactory for the initially-attractive waves in Fig. 4.2. They suffer from large oscillations, especially in between 0.1 and 0.2 fm. As the short-distance wave functions are based on an expansion in powers of r, one would ideally use as small a value of r as possible to ensure an accurate starting point. However, as the plot shows, that would lead to an unacceptable level of dependence on the matching radius. On a more positive note, the addition of more terms in the wave functions does make an improvement in the lower r region of the plot, although it seems to get worse before it gets better, highlighting the poor convergence.

For the ${}^3S_1 - {}^3D_1$ waves, we therefore use short-distance wave functions with terms up to order $n = 11/2$ (although in principle it might be worth including even more terms) and a matching radius of $R_m = 0.3$ fm, a value which is not 'too' large and is on a maxima of an oscillation.

The second radius to discuss is the radius of the delta-shell, denoted R_0. As already mentioned a small value of R_0 is preferred to ensure that cut-off artefacts

[8] We extract our phase shifts and amplitudes at $r = 30$fm as it is large enough that it is well outside the range of the OPE potentials.

are diminished.

Also, in the definitions of the residual strength matrices $\tilde{\mathbf{V}}^{(2)}_{(AR)}(p)$ and $\tilde{\mathbf{V}}^{(4)}_{(AR)}(p)$, defined in Eqs. (4.75) and (4.76) respectively, we can write, for the matrices on the LHS for example, that for small R_0

$$\mathbf{F_0}^{\top}\left(\mathbf{u}_l^{\top}\right)^{-1}(p,R_0) \to \mathbf{F_0}^{\top}\left(\mathbf{F}^{\top}\right)^{-1}(p,R_0)\left(\mathbf{C}^{\top}\right)^{-1}(p). \tag{4.77}$$

Now, to remove the R_0 dependence we are relying on the fact that $\mathbf{F_0}^{\top}\left(\mathbf{F}^{\top}\right)^{-1}(p,R_0) \to \mathbf{1}$ for $R_0, p \to 0$, i.e. that this combination of matrices tends to the identity matrix for decreasing energy and distance, which on the surface one would have thought must be the case. However, writing out $\mathbf{F_0}^{\top}\left(\mathbf{F}^{\top}\right)^{-1}(p,R_0)$ explicitly and performing the matrix multiplication we get,

$$\mathbf{F_0}^{\top}\left(\mathbf{F}^{\top}\right)^{-1}(p,R_0) = \begin{pmatrix} \dfrac{2F_A(0)G_R(p)+G_A(0)F_R(p)}{2F_A(p)G_R(p)+G_A(p)F_R(p)} & \dfrac{-\sqrt{2}\left[F_A(0)G_A(p)-G_A(0)F_A(p)\right]}{2F_A(p)G_R(p)+G_A(p)F_R(p)} \\ \dfrac{-\sqrt{2}\left[F_R(0)G_R(p)-G_R(0)F_R(p)\right]}{2F_A(p)G_R(p)+G_A(p)F_R(p)} & \dfrac{F_R(0)G_A(p)+2G_R(0)F_A(p)}{2F_A(p)G_R(p)+G_A(p)F_R(p)} \end{pmatrix}, \tag{4.78}$$

where we have assumed that the RHS of the equation is evaluated at R_0. The diagonal elements and the lower off-diagonal element in this matrix behave as expected and tend to 1 and 0 respectively. However, the upper off-diagonal element, is more problematic. This is because as $R_0 \to 0$ the repulsive functions in the denominator (exponentially) reduce more rapidly than the numerator (which only involves attractive functions) is able to, and therefore this element blows up rather than vanishes. This behaviour is depicted in Fig. 4.3 (see also Fig. 4.13 showing the (less severe) case for the ${}^3P_2 - {}^3F_2$ waves). The 'spikes' in Fig. 4.3 are due to the presence of nodes in the attractive functions, and therefore R_0 should be chosen to avoid them. There is a reasonable region of stability between approximately $R_0 = 0.2$ and 0.4 fm, we therefore choose R_0 to be in this region, and show results for $R_0 = 0.3$ fm.

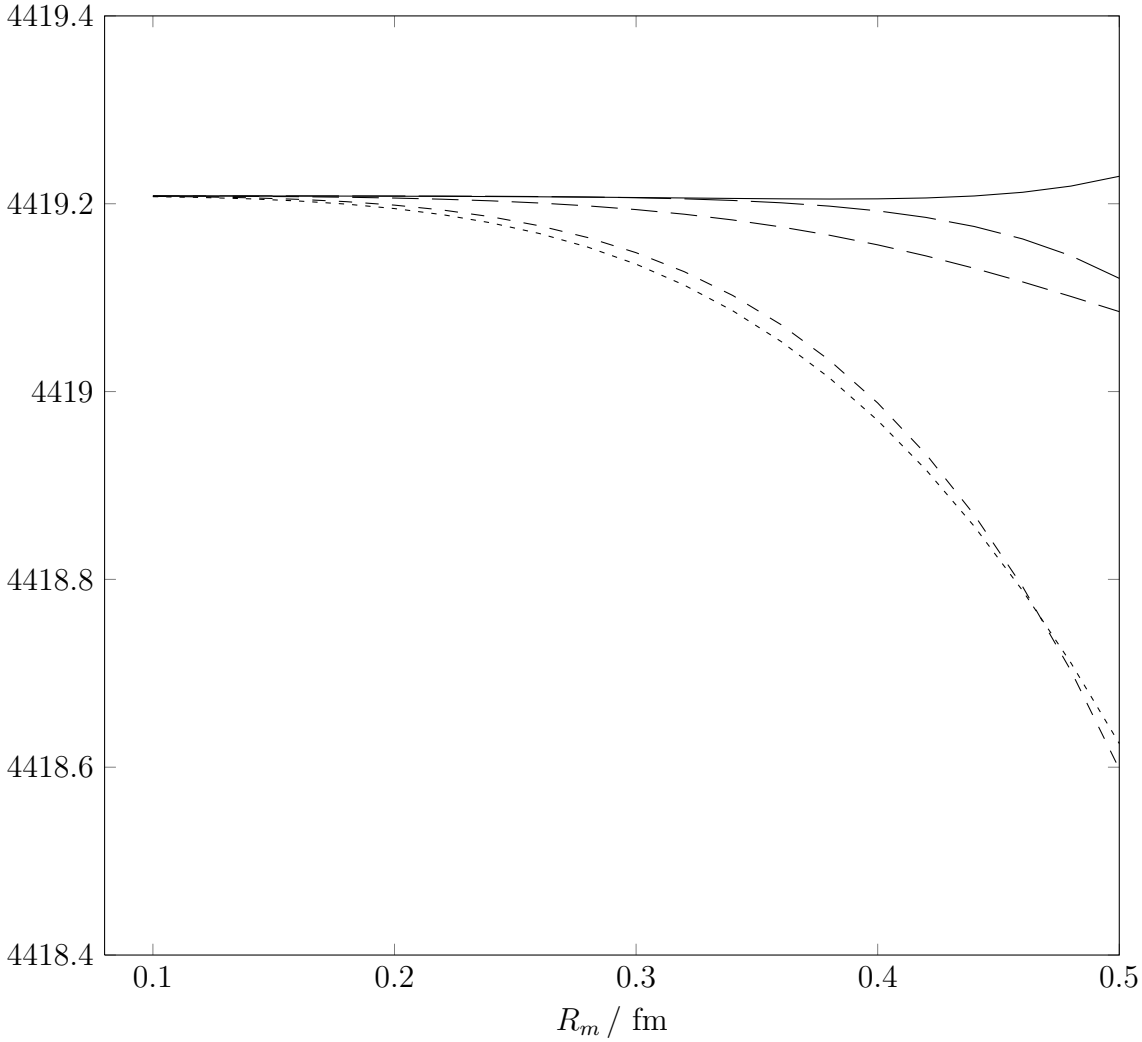

Figure 4.1: ${}^3S_1 - {}^3D_1$: dependence of the "repulsive" S-wave function, $u_1(p, r)$ at $r = 30$fm on the matching radius ($T = 100$ MeV). The different curves correspond to the maximum order n of (r/R) included in the short-distance wave functions. We show results for $n = 7/2$ (short-dashed), 8/2, 9/2, 10/2 and 11/2 (solid).

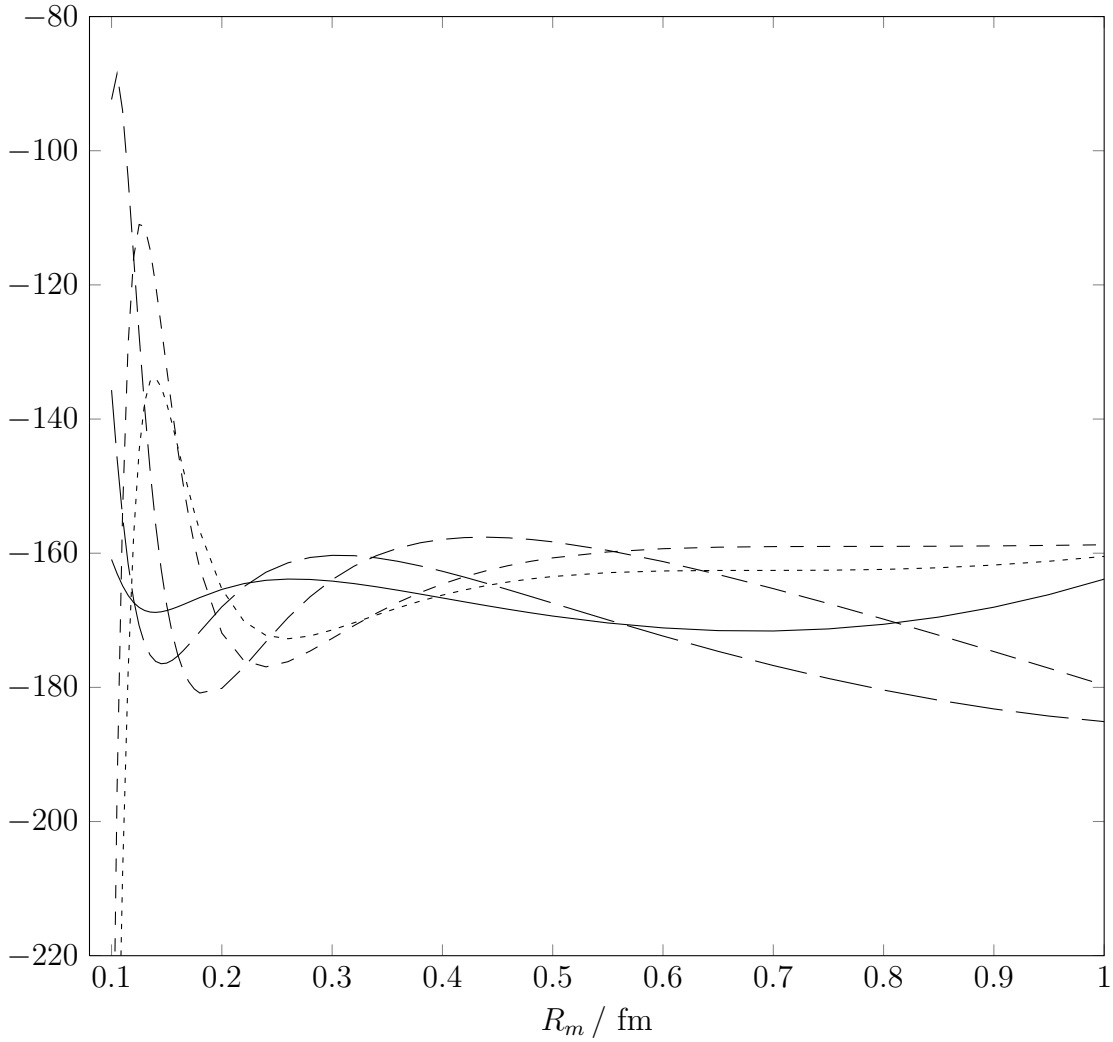

Figure 4.2: ${}^3S_1 - {}^3D_1$: dependence of the "attractive" S-wave function, $u_2(p, r)$ at $r = 30$fm on the matching radius ($T = 100$ MeV). The different curves correspond to the maximum order n of (r/R) included in the short-distance wave functions. We show results for $n = 7/2$ (short-dashed), 8/2, 9/2, 10/2 and 11/2 (solid).

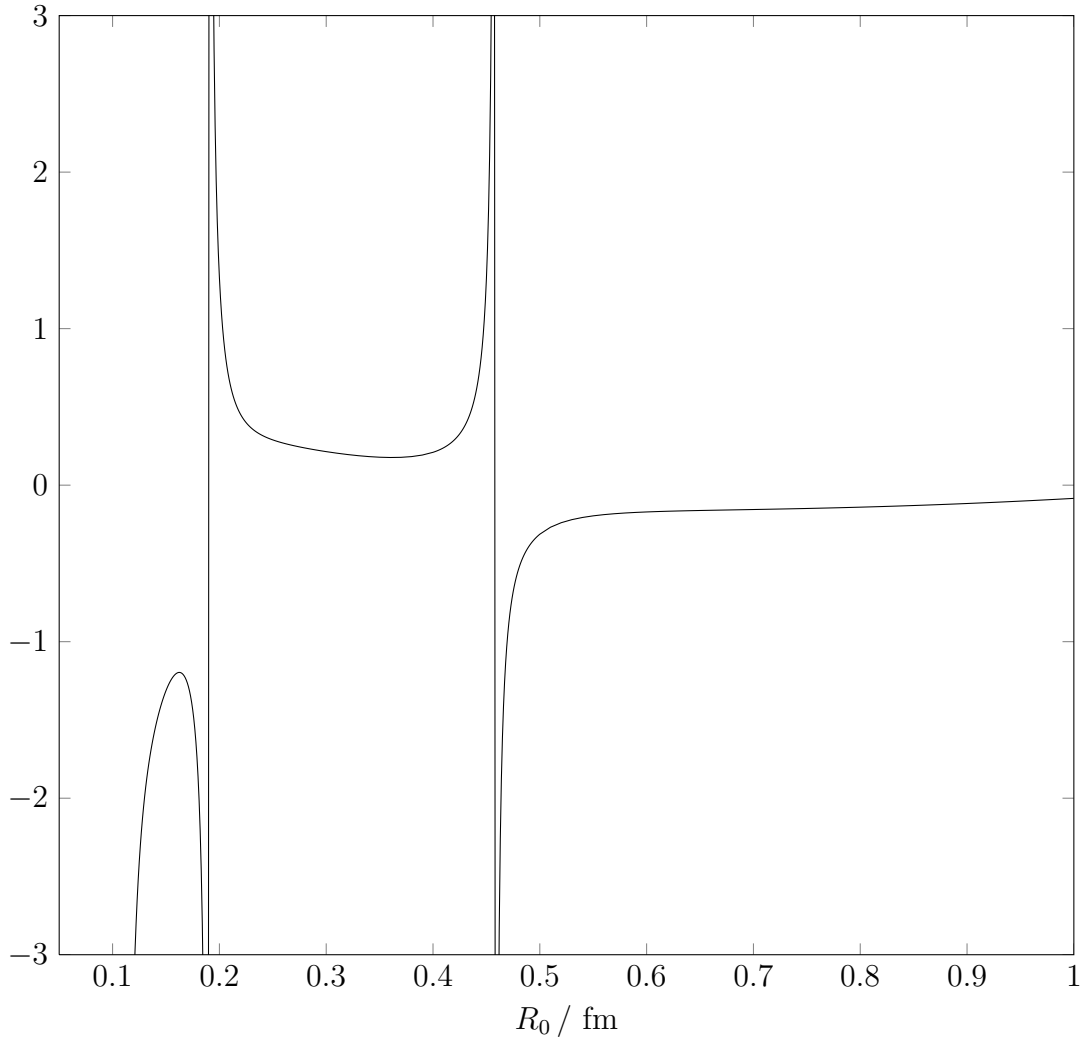

Figure 4.3: The variation of the upper off-diagonal element in the matrix $\mathbf{F_0}^\top \left(\mathbf{F}^\top\right)^{-1}(p, R_0)$ (see Eq. (4.78)) as a function of R_0 ($T = 5$ MeV).

	a
PWA	5.420(1)
NijmI	5.418
NijmII	5.420
Reid93	5.422

Table 4.1: $^3S_1$ scattering length (in units of fm) for four different Nijmegen analyses [101].

4.1.4 Results and Discussion

The results of the analysis for the $^3S_1$-$^3D_1$ coupled waves are presented in Figs. 4.4 - 4.12. Note that in generating the results we chose to fit to the $a(^3S_1) = 5.420$ fm scattering length (see Table. 4.1). We also took into account the different pion masses. We did not however, remove the effects due to the $\pi\gamma$ exchange, unlike what was done in the uncoupled spin-triplet waves in Ref. [81]. Although I gather from discussions with Prof. Birse that this term had negligible effects.

In plots 4.4, 4.5 and 4.6 we present the $^3S_1$, $3D_1$ eigen phase shifts and mixing parameter ϵ_1, respectively. The solid curves are from the Nijmegen analyses, and the dashed lines are due to iterated OPE and the energy-independent contact interaction (iterated also, by fitting the short-distance phase parameter to the scattering length mentioned above). As expected, in all plots the two types of curves agree at low energies and diverge as different long-range forces (such as TPE) come into play at higher energies.

In Figs. 4.7 - 4.9 and 4.10 - 4.12 we display the various elements of the residual strength matrix after the removal of OPE (using Eq. (4.75)) and after the removal of all long-range forces up to order Q^3 (using Eq. (4.76)), respectively. Note that these are unrenormalised results.

Comparing Figs. 4.7 and 4.10, it is clear to see that the strong energy-dependence present in Fig. 4.7 where only OPE has been subtracted, has disappeared from the plot in Fig. 4.10, leaving behind a smooth linear divergence. After subtracting a quadratic fit from the results in Fig. 4.10 the renormalised results looked similar to that of the results in Fig. 7 (b) in Ref. [81], the only major difference being a strong downward trend below about 20 MeV consistent with all Nijmegen curves, possibly suggesting that other long-range forces are still at work. We also subtracted a linear fit, the result looking more like a parabola, although the scale of the plot was still very small (the range of the plot was -0.02

to 0.07 fm^0, whereas the range of the plot for the quadratic subtraction was -0.05 to 0.01 fm^0). In any case, it looks like only two counterterms are needed to produce renormalised and finite results for the $^3S_1$ wave, in agreement with that of Valderrama [84], unlike what Birse expects from the RG in [65].

The results for the other elements are harder to interpret. For example, it looks possible that for the off-diagonal elements in Figs. 4.8 and 4.11 there is a single energy-independent counterterm. The results of Figs. 4.9 and 4.12 are slightly more alarming, however, they are very small so may not be reliable. These Figs. also show the downward trend mentioned above, it is not clear what is causing this.

However, on a positive note, to the order that we are working in the DWBA, the off-diagonal elements in the RHS of Eq. (4.71) are equal, i.e. the matrix is symmetric and therefore Hermitian. This can be seen by considering that if the extra scattering is weak $\delta_\alpha \approx \delta_{\alpha,l}$ and $\delta_\beta \approx \delta_{\beta,l}$ implying that $\cos(\Delta_{\alpha\alpha})$ and $\cos(\Delta_{\beta\beta}) \to 1$ and $\sin(\Delta_{\beta\alpha}) = -\sin(\Delta_{\alpha\beta})$. The fact that our off-diagonal elements agree with each other shows that to a good approximation that this is indeed the case.

Finally, to extract a breakdown scale, we use the coefficient of the quadratic term (obtained from a quartic fit - as this provided more stable coefficients). This is because the intercept and slope are regulator dependent, so we cannot extract a scale from these. To provide a measure of the error, we fit the coefficient for PWA93 and Nijm1 in the 100 - 200 MeV energy range, and the PWA93 again but in the energy range 50 - 250 MeV. Respectively, we obtain values of approximately 431, 441 and 443 MeV. This indicates good convergence of the EFT. It is slightly higher than the value (of approximately 340 MeV) predicted by Valderrama in Ref. [84].

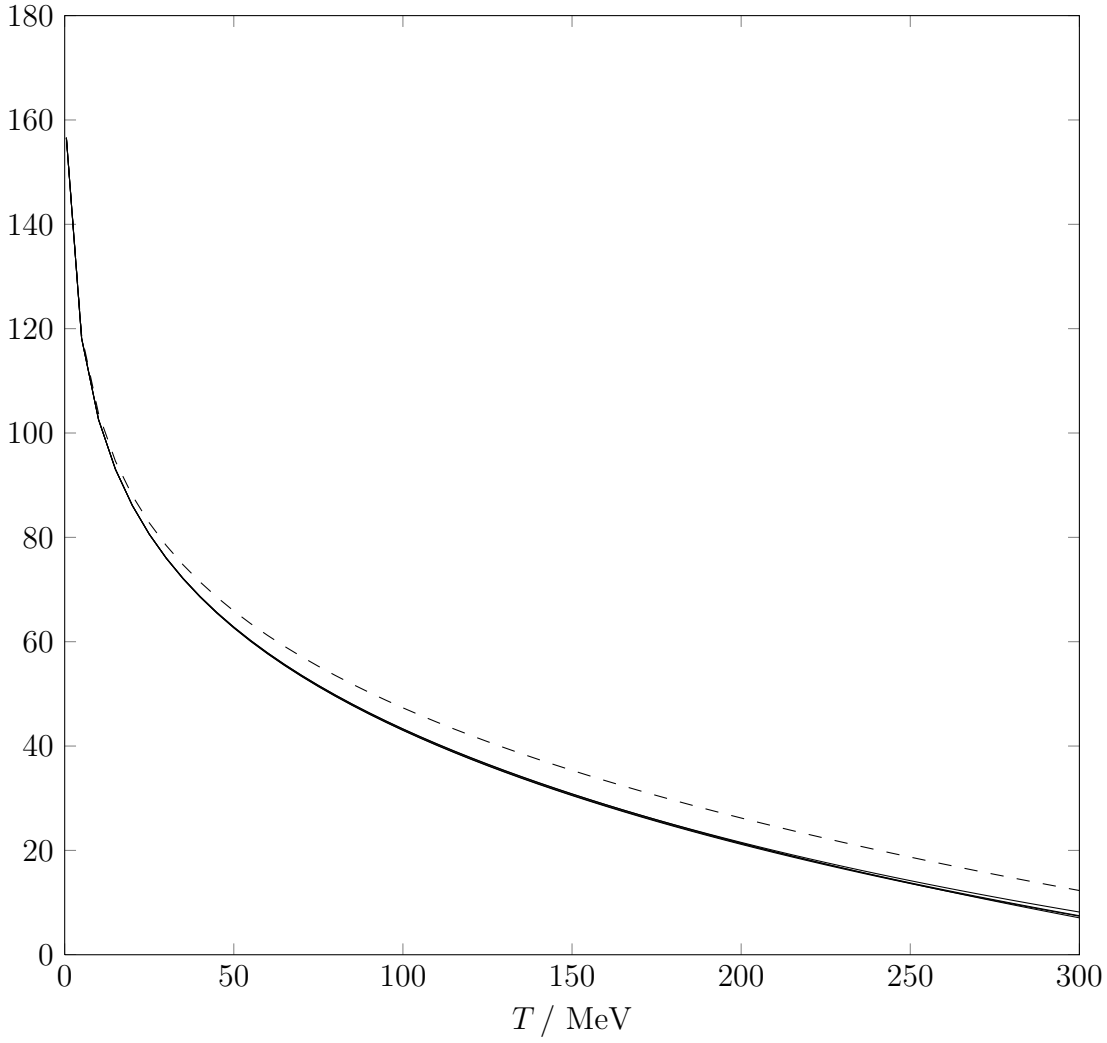

Figure 4.4: Eigen phase shifts in the $^3S_1$ channel (in degrees): the dashed curve is due to iterated OPE with a scattering length fixed at 5.42 fm, while the solid curves correspond to four different Nijmegen analyses. T is the lab kinetic energy.

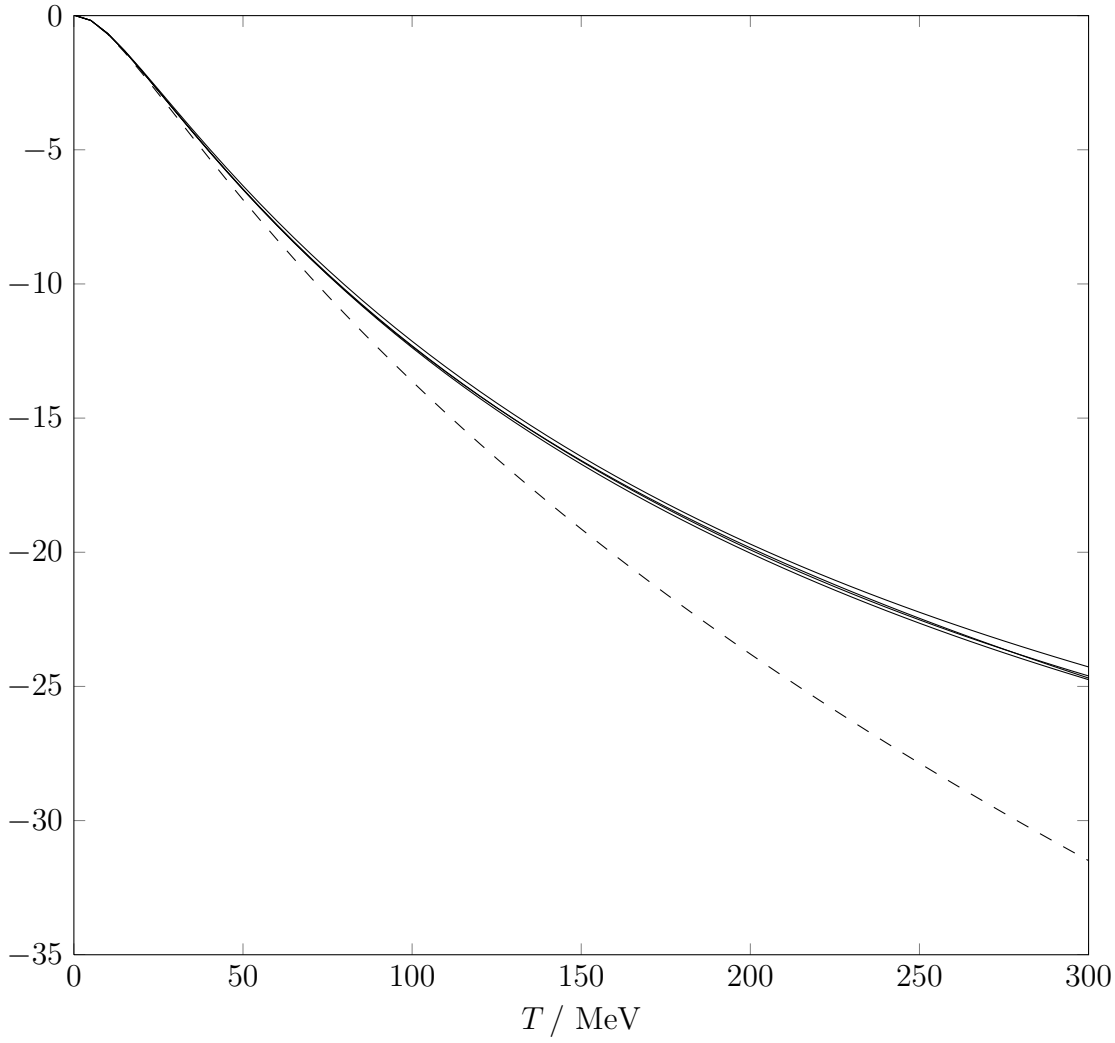

Figure 4.5: Eigen phase shifts in the ${}^3D_1$ channel (in degrees). See the caption to Fig. 4.4 for further details.

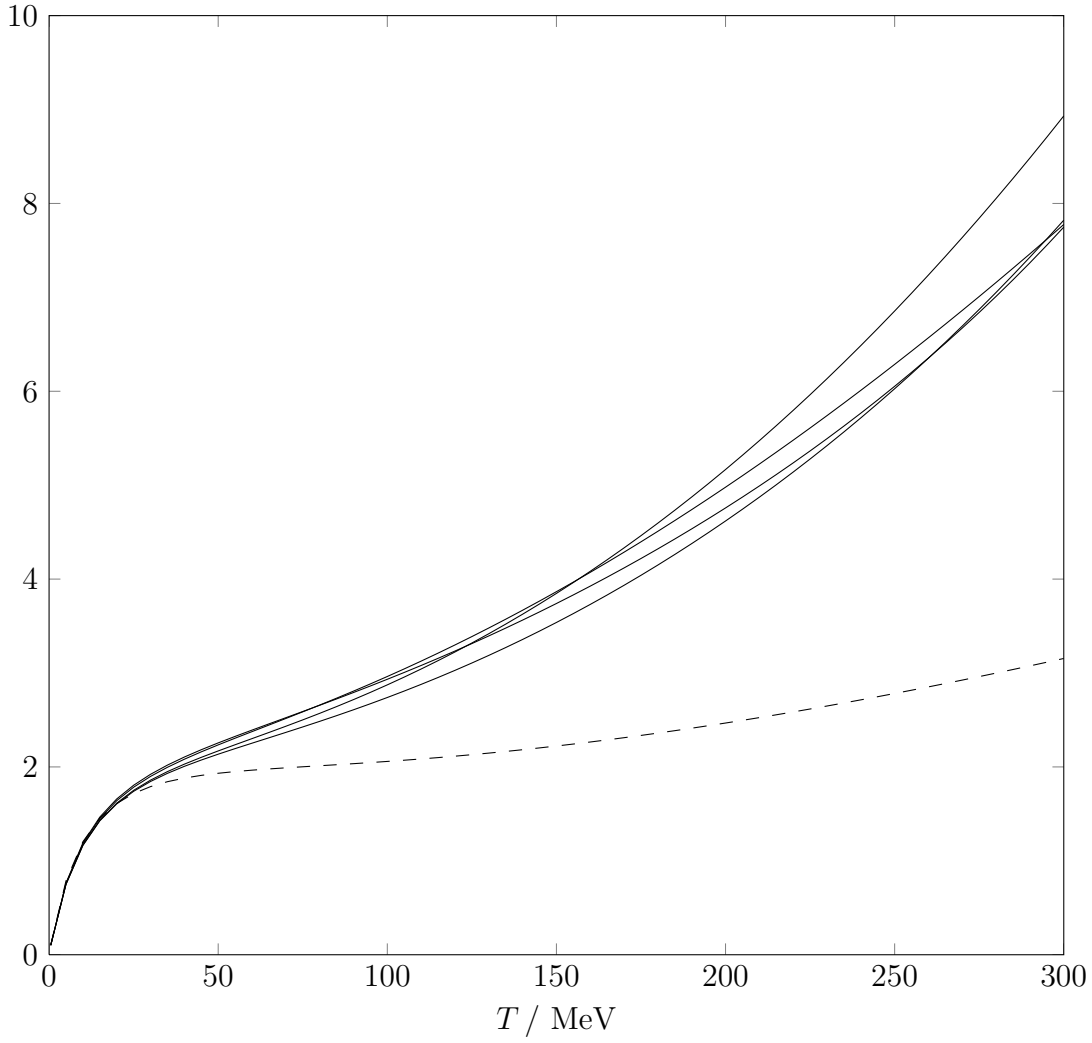

Figure 4.6: Mixing angle ϵ_1 in the eigen-basis (in degrees). See the caption to Fig. 4.4 for further details.

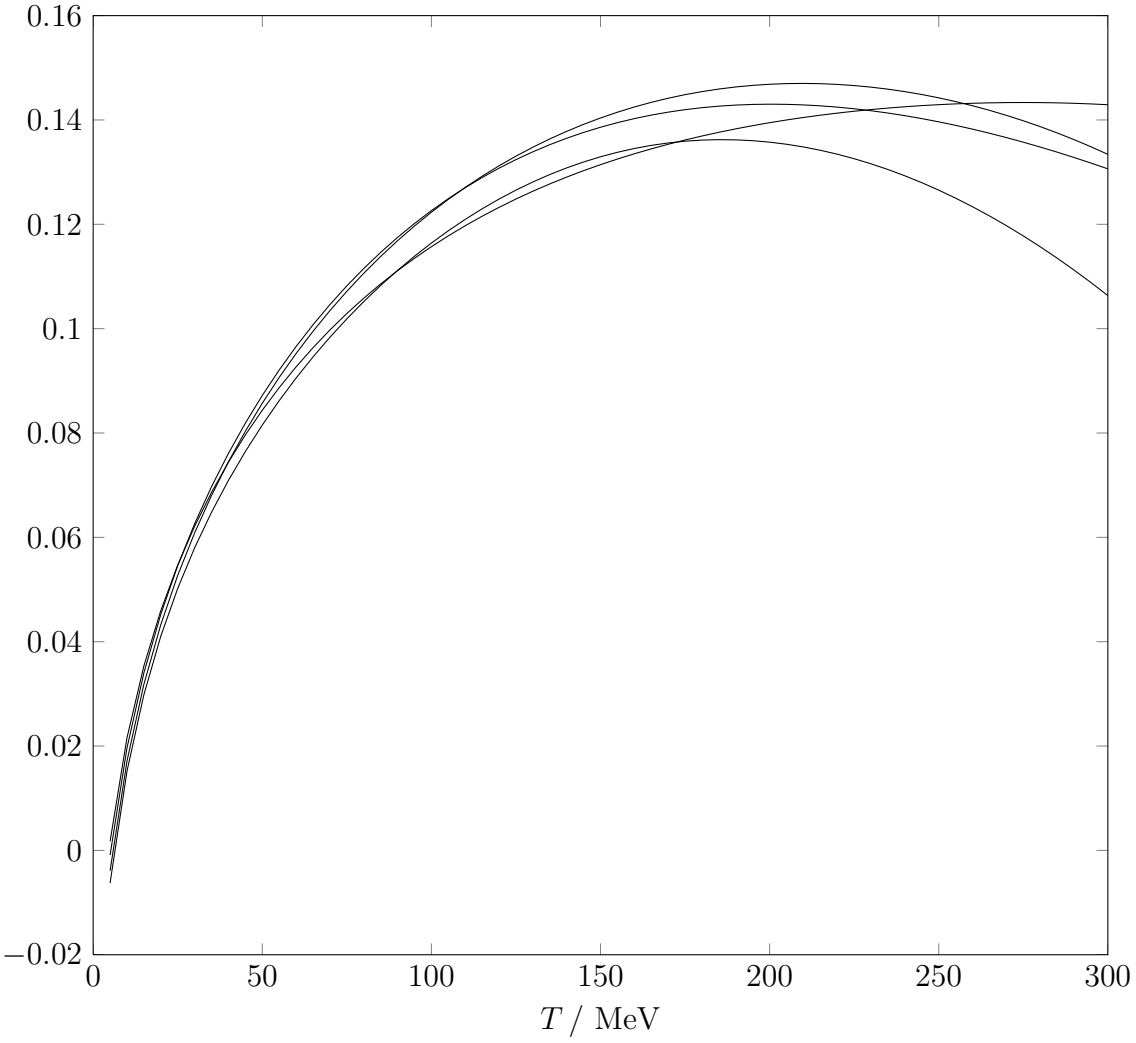

Figure 4.7: The residual interaction matrix element $\tilde{V}^{(2)}_{AA}(p)$, in fm^0, in the $^3S_1 - {}^3D_1$ channels, after the removal of iterated OPE from four different Nijmegen phase shifts as a function of lab kinetic energy. We have used $a(^3S_1) = 5.420$ fm, and $R_0 = 0.3$ fm.

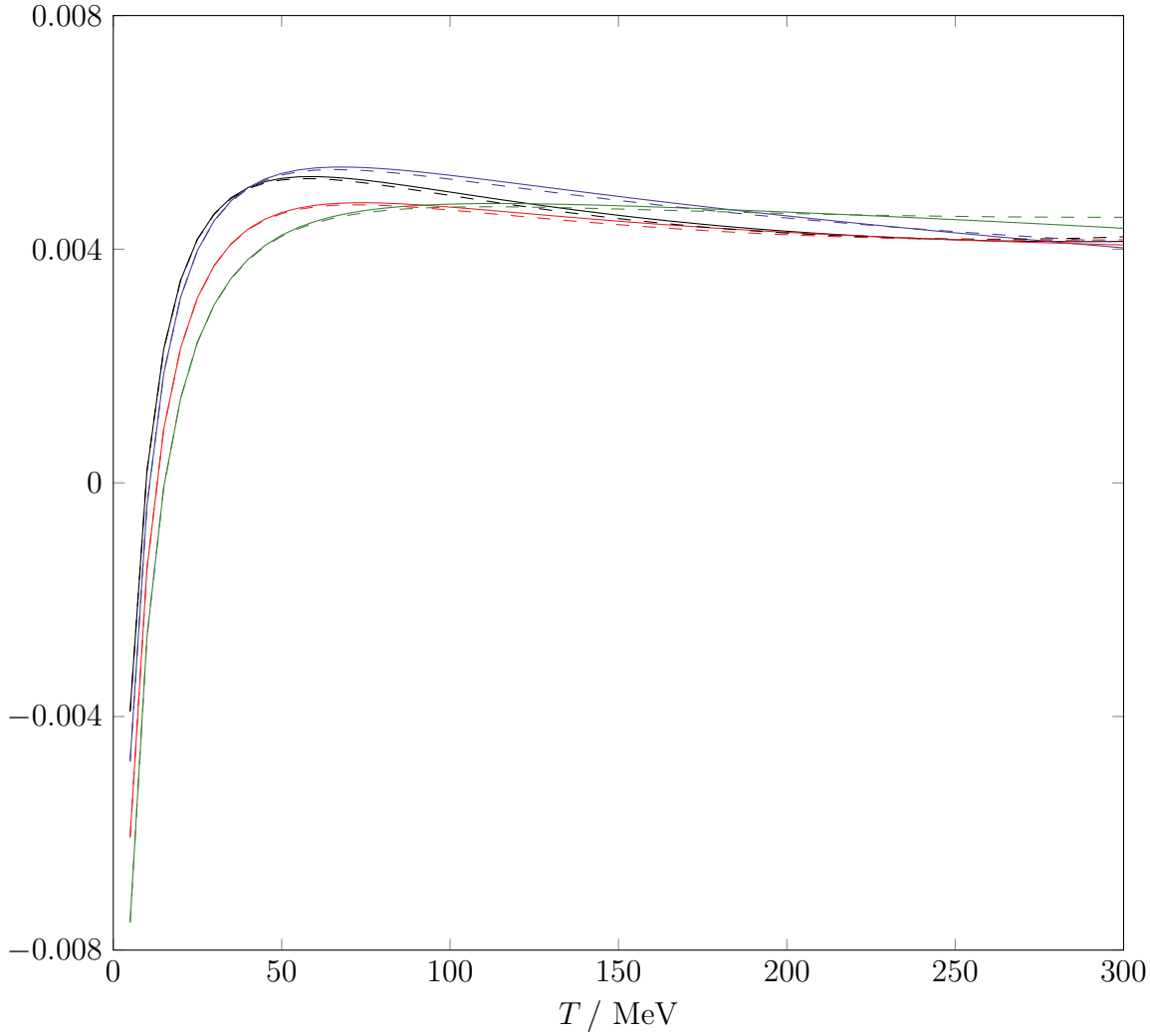

Figure 4.8: The residual interaction matrix elements $\tilde{V}^{(2)}_{AR}(p)$ (solid) and $\tilde{V}^{(2)}_{RA}(p)$ (dashed) in the ${}^3S_1 - {}^3D_1$ channels. See the caption to Fig. 4.7 for further details.

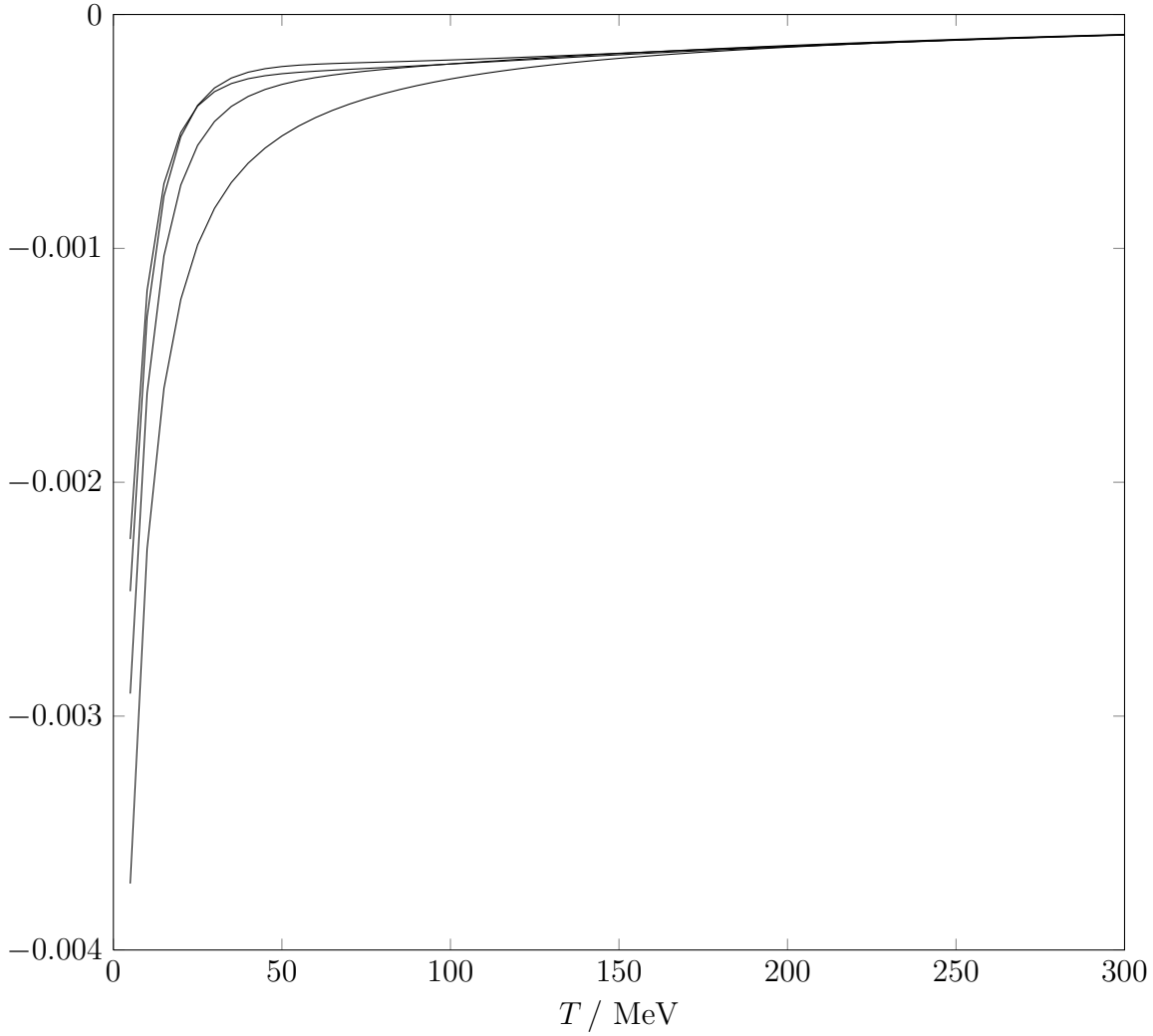

Figure 4.9: The residual interaction matrix element $\tilde{V}^{(2)}_{RR}(p)$ in the ${}^3S_1 - {}^3D_1$ channels. See the caption to Fig. 4.7 for further details.

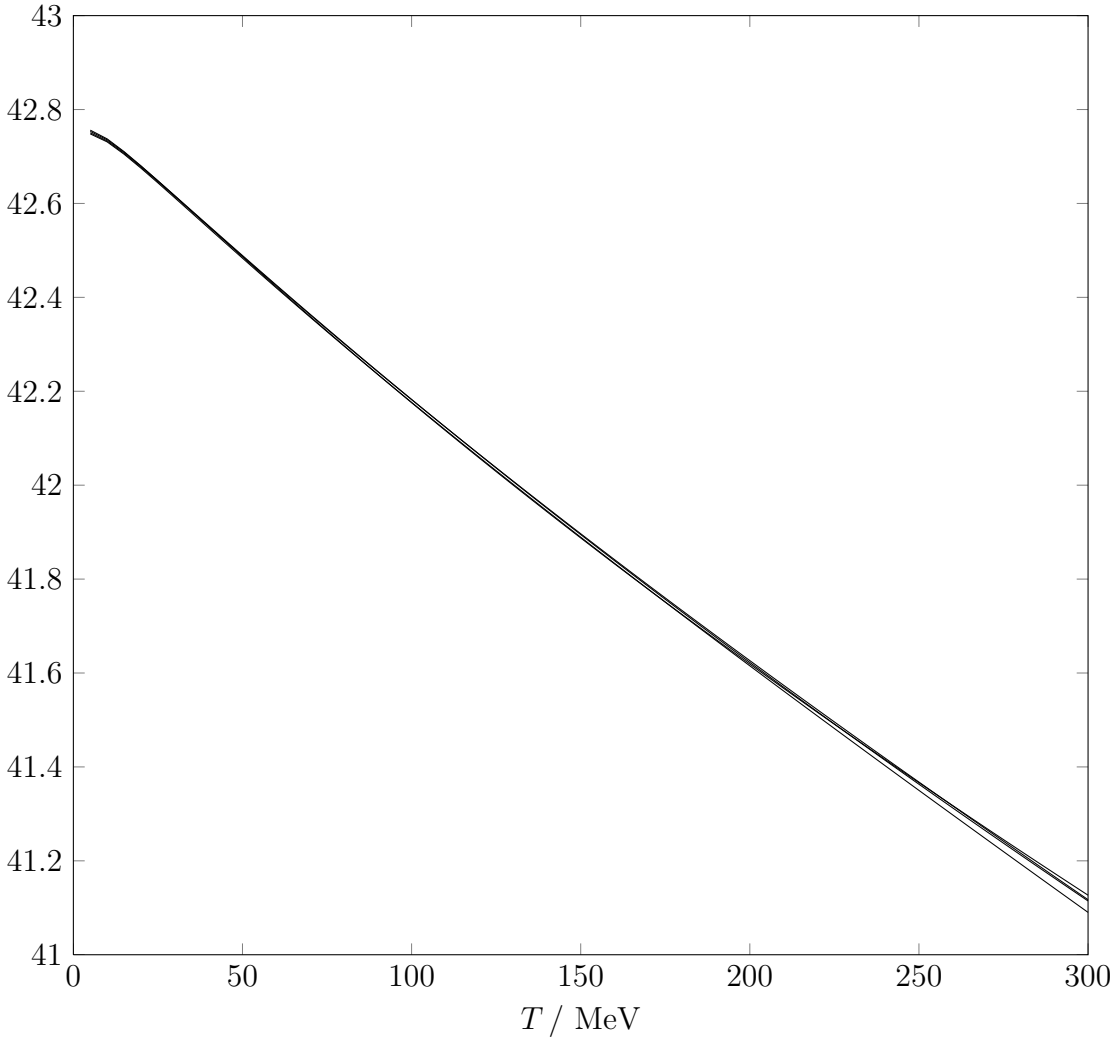

Figure 4.10: The residual interaction matrix element $\tilde{V}^{(4)}_{AA}(p)$, in fm^0, in the $^3S_1 - {}^3D_1$ channels, after the removal of OPE and TPE potentials up to order-Q^3 from four different Nijmegen phase shifts as a function of lab kinetic energy. We have used $a(^3S_1) = 5.420$ fm, and $R_0 = 0.3$ fm.

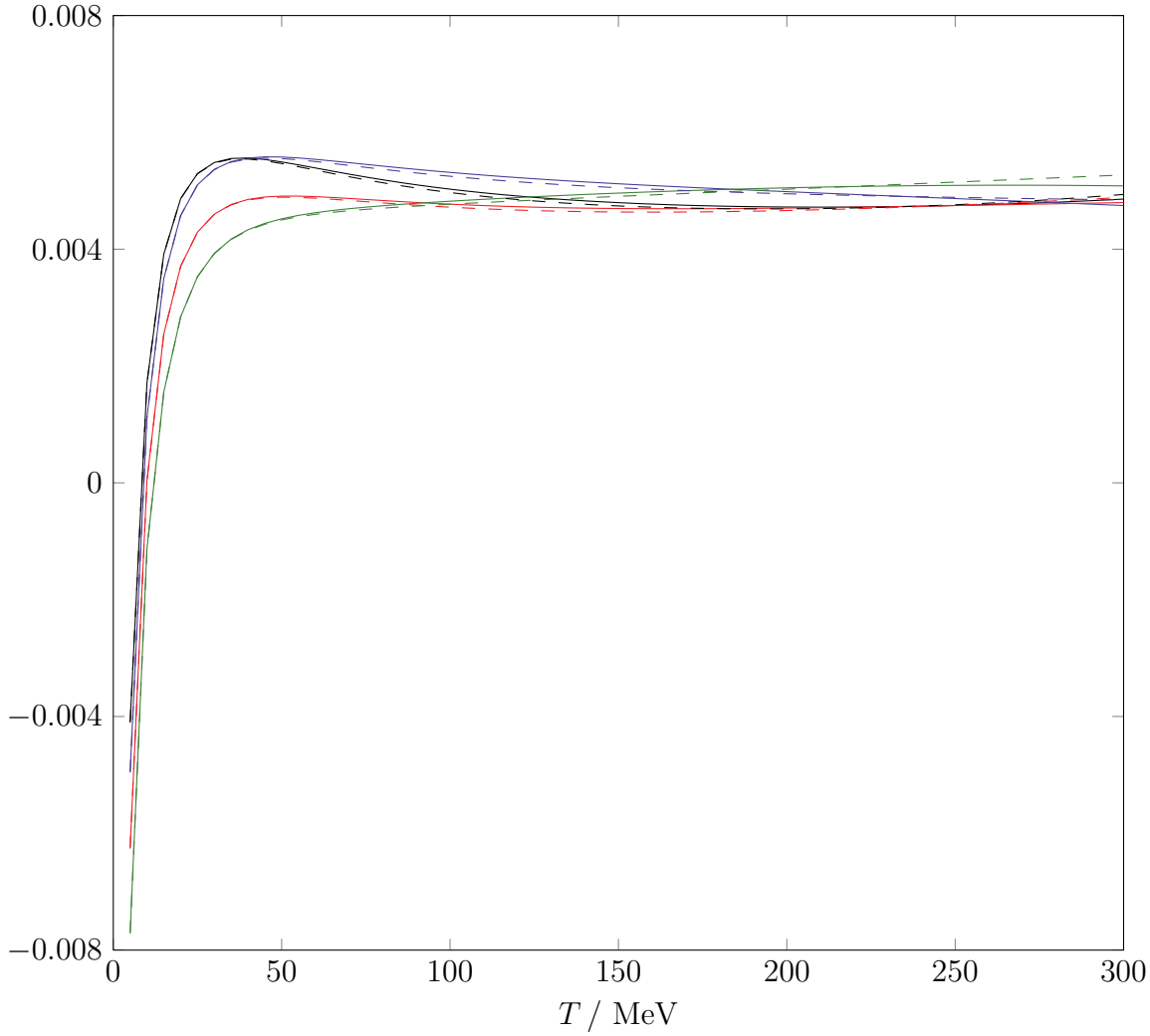

Figure 4.11: The residual interaction matrix elements $\tilde{V}^{(4)}_{AR}(p)$ (solid) and $\tilde{V}^{(4)}_{RA}(p)$ (dashed) in the ${}^3S_1 - {}^3D_1$ channels. See the caption to Fig. 4.10 for more details.

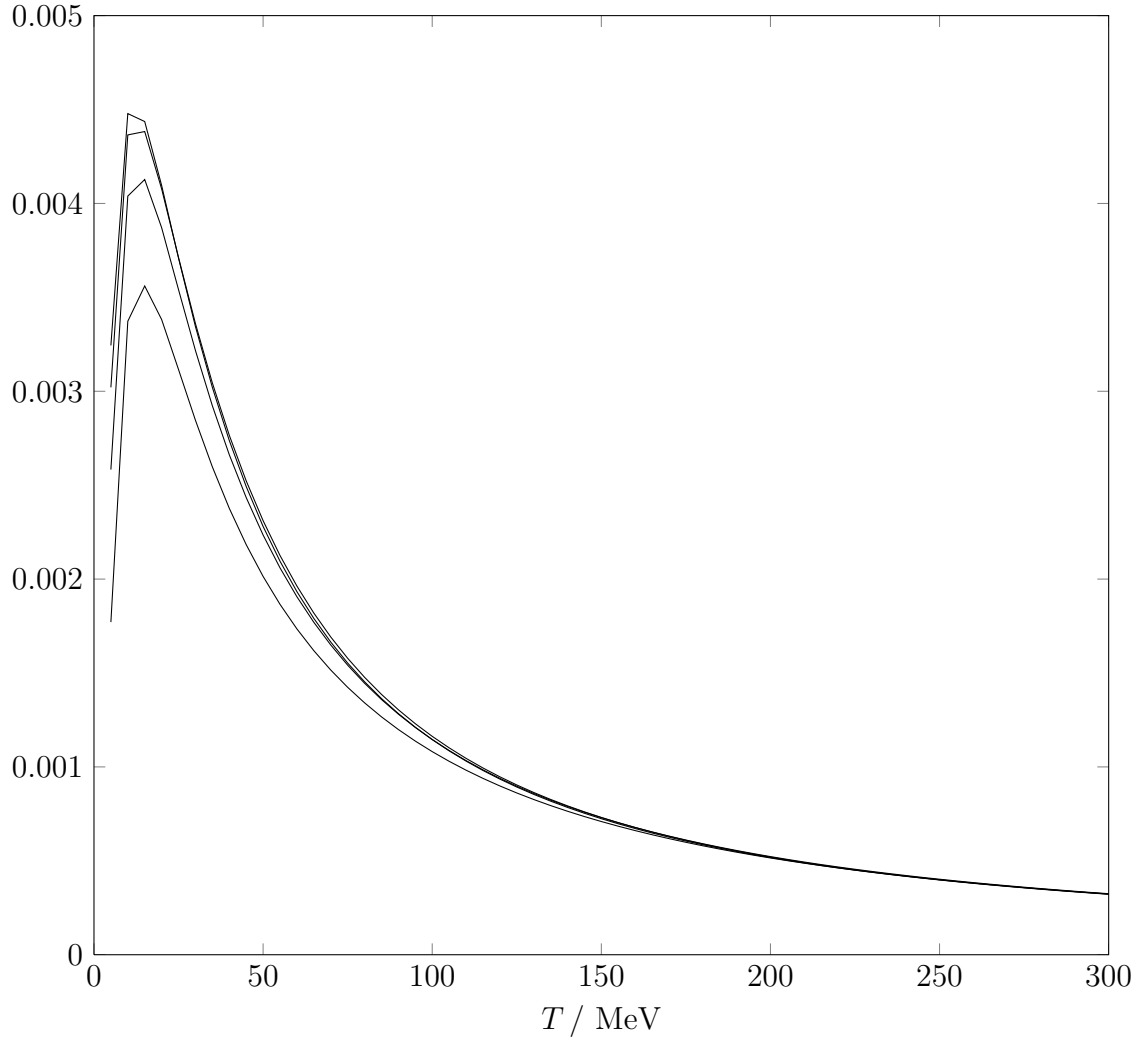

Figure 4.12: The residual interaction matrix element $\tilde{V}^{(4)}_{RR}(p)$ in the ${}^3S_1 - {}^3D_1$ channels. See the caption to Fig. 4.10 for more details.

4.2 Spin Triplet Waves: $^3P_2 - {}^3F_2$

The method used to extract a short-range effective interaction matrix in the $^3P_2 - {}^3F_2$ waves is (for the most part) the same as the method described above for the $^3S_1 - {}^3D_1$ waves. However, for completeness, we will briefly include here some of the most important equations that are specific to the $^3P_2 - {}^3F_2$ waves, which may be useful to the reader.

4.2.1 Distorted Eigen Waves

Setting $J = 2$ in Eqs. (4.1) and (4.2), we obtain the following coupled radial Schödinger equations describing NN scattering in the $^3P_2 - {}^3F_2$ coupled channels, interacting via the OPE potential,

$$\left(\frac{\mathrm{d}^2}{\mathrm{d}r^2} + p^2 - U_{\pi C}(r) + \frac{2}{5}U_{\pi T}(r) - \frac{2}{r^2}\right) u_l(r) = \frac{6\sqrt{6}}{5}U_{\pi T}(r)w_l(r) \tag{4.79}$$

and

$$\left(\frac{\mathrm{d}^2}{\mathrm{d}r^2} + p^2 - U_{\pi C}(r) + \frac{8}{5}U_{\pi T}(r) - \frac{12}{r^2}\right) w_l(r) = \frac{6\sqrt{6}}{5}U_{\pi T}(r)u_l(r), \tag{4.80}$$

where, as before $U_{\pi C}(r)$ and $U_{\pi T}(r)$ denote central and tensor OPE reduced potentials, defined in Eqs. (3.2) and (3.4), and we have remembered that the $^3P_2 - {}^3F_2$ waves have a total isospin of $I = 1$.

As usual, there are two regions of interest to investigate in the process of constructing the two pairs of distorted waves. Starting close to the origin, considering only the region where the $1/r^3$ part of the tensor potential is dominant, we can, after rewriting Eqs. (4.79) and (4.80) as a single matrix equation, use the operator

$$\hat{U} = \sqrt{\frac{3}{5}}\begin{pmatrix} \sqrt{\frac{2}{3}} & -1 \\ 1 & \sqrt{\frac{2}{3}} \end{pmatrix} \tag{4.81}$$

to perform a unitary transformation, which diagonalises the matrix equation into an attractive-repulsive basis, giving

$$\begin{pmatrix} -\frac{\mathrm{d}^2}{\mathrm{d}r^2} - \frac{8R}{3r^3} & 0 \\ 0 & -\frac{\mathrm{d}^2}{\mathrm{d}r^2} + \frac{4R}{3r^3} \end{pmatrix} \begin{pmatrix} u_A(r) \\ u_R(r) \end{pmatrix} = \begin{pmatrix} 0 \\ 0 \end{pmatrix} \tag{4.82}$$

where we have defined the following

$$\begin{pmatrix} u_A(r) \\ u_R(r) \end{pmatrix} = \sqrt{\frac{3}{5}} \begin{pmatrix} \sqrt{\frac{2}{3}} & -1 \\ 1 & \sqrt{\frac{2}{3}} \end{pmatrix} \begin{pmatrix} u_l(r) \\ w_l(r) \end{pmatrix}. \tag{4.83}$$

Applying the same method as previously described in section 4.1.1 which culminated in Eqs. (4.21) and (4.22) to the ${}^3P_2 - {}^3F_2$ waves, results in the following equations for the short-distance wave functions

$$\begin{pmatrix} u_l(r) \\ w_l(r) \end{pmatrix} = \begin{pmatrix} \sqrt{\frac{2}{3}} F_A(r) & F_R(r) \\ -G_A(r) & \sqrt{\frac{2}{3}} G_R(r) \end{pmatrix} \begin{pmatrix} C_A \\ C_{2R} \end{pmatrix}, \tag{4.84}$$

where

$$\begin{aligned} F_A(r) &= 2\sqrt{\frac{3}{5}} \left(\frac{r}{R}\right)^{3/4} [f_{1A}^{Re}(r) \cos(4\sqrt{2R/3r} - \psi) + f_{1A}^{Im} \sin(4\sqrt{2R/3r} - \psi)] \\ G_A(r) &= 2\sqrt{\frac{3}{5}} \left(\frac{r}{R}\right)^{3/4} [g_{1A}^{Re}(r) \cos(4\sqrt{2R/3r} - \psi) + g_{1A}^{Im} \sin(4\sqrt{2R/3r} - \psi)] \\ F_R(r) &= \sqrt{\frac{3}{5}} \left(\frac{r}{R}\right)^{3/4} f_{2R}(r) e^{-4\sqrt{R/3r}} \\ G_R(r) &= \sqrt{\frac{3}{5}} \left(\frac{r}{R}\right)^{3/4} g_{2R}(r) e^{-4\sqrt{R/3r}}, \end{aligned} \tag{4.85}$$

whose functions, f_{1A}, g_{1A}, f_{2R} and g_{2R}, are defined in Appendix D. C_A, C_{2R} and ψ are defined in the same way as they are in Eqs. (4.21) and (4.22).

The process used to construct the two pairs of distorted eigen waves also involves examining the large-r region (where the centrifugal potential is dominant), because it is in this region where the various phase shifts and normalisation constants can be extracted. This was shown in section 4.1.1 for general coupled waves with total angular momentum J so it does not need to be repeated here. However, to fix the short-distance phase shift parameter, ψ, we used Eq. (4.1.1)

to fix the S-wave eigen phase shift to the ${}^3S_1$ np scattering length at zero energy, this is obviously specific to that channel. For the ${}^3P_2 - {}^3F_2$ waves, therefore, we determine ψ by fixing the P-wave eigen phase shift to the to the ${}^3P_2$ np scattering volume at zero energy, which are related by

$$a = -\frac{\tan(\delta)}{p^3}. \tag{4.86}$$

4.2.2 Effective Residual Interaction Matrix

To obtain an effective residual interaction matrix in the ${}^3P_2 - {}^3F_2$ coupled channels after firstly the removal of leading-order OPE, then secondly, after the removal of the pion-exchange forces that appear at chiral orders $Q^{2,3}$, we use Eqs. (4.75) and (4.76), respectively. However, for the channels under consideration here, we use the following matrix for the wave functions at small-r

$$\begin{aligned} \mathbf{u}_l(p,r) &= \begin{pmatrix} u_{l,\alpha}(p,r) & u_{l,\beta}(p,r) \\ w_{l,\alpha}(p,r) & w_{l,\beta}(p,r) \end{pmatrix} \\ &\xrightarrow{r\to 0} \begin{pmatrix} \sqrt{\frac{2}{3}}F_A(r) & F_R(r) \\ -G_A(r) & \sqrt{\frac{2}{3}}G_R(r) \end{pmatrix} \begin{pmatrix} C_{A\alpha}(p) & C_{A\beta}(p) \\ C_{R\alpha}(p) & C_{R\beta}(p) \end{pmatrix}, \end{aligned} \tag{4.87}$$

which in turn provide the definition for $\mathbf{F_0} = \mathbf{F}(0, R_0)$ which also appears in Eqs. (4.75) and (4.76), since Eq. (4.87) can be written as $\mathbf{u}_l(p,r) \to \mathbf{F}(p,r)\mathbf{C}(p)$.

Now, unlike when obtaining the interaction matrix in the ${}^3S_1 - {}^3D_1$ coupled channels, it should be mentioned that more thought is required when interpreting the results of Eqs. (4.75) and (4.76) in the ${}^3P_2 - {}^3F_2$ channels. This is because the 'AR','RA' and 'RR' matrix elements (see Eq. (4.74)) are misleadingly large compared to the 'AA' element, when in fact, with further examination, it actually appears that only the 'AA' element matters in this channel. This is discussed further in the next section.

4.2.3 Results and Discussion

Here we present the results for the ${}^3P_2 - {}^3F_2$ coupled waves. In generating our results we set the short-distance phase parameter to $\psi = -28.9012°$, which corresponds to a ${}^3P_2$ np scattering volume of $a({}^3P_2) = -0.2844$ fm^3 (this particular value for the scattering volume comes from Valderrama and Arriola who performed a fit to the NijmII phase shifts in Ref. [102]). Note that this differs from the closely related work of both Valderrama [85] and Long and Yang [86]. Valderrama chooses to fit to a much lower scattering volume of -0.04 fm^3, whereas Long and Yang fit the phase shift to the Nijmegen ones at 50 MeV.

Starting with Fig. 4.14, we show the ${}^3P_2$ phase shifts due to iterated OPE as a function of lab kinetic energy compared to the Nijm1 phase shifts for both bar and eigen parametrisations. One can see that if one fixes ψ to the scattering volume that gives the correct behaviour at zero energy then the ${}^3P_2$ phase shift experiences a resonance at higher energies. Alternatively, as also shown Fig. 4.14, whilst fixing the value of the scattering volume to approximately half that of the Nijm1 one gives a better overall description of the Nijmegen phases, it fails at the lowest energies.

In a similar way we show in Figs. 4.15 and 4.16 the ${}^3F_2$ phase shifts and ϵ_2 mixing angles respectively. In these cases it is interesting to see how different the bar and eigen phase shifts look from each other. Fitting to different scattering volumes only starts to show differences in the bar phase shifts above about 40 MeV, whereas for the eigen phase shifts it is a completely different story, as they diverge from each other almost immediately.

Our main results for the ${}^3P_2 - {}^3F_2$ coupled waves are shown in Figs. 4.17 and 4.18. As mentioned previously, there is a redundancy between the short-distance phase parameter ψ and the leading (energy-independent) contact interaction. This means that any change in ψ should be compensated by a corresponding shift in the leading contact interaction, provided that the resulting change in the wave function is small enough to be treated perturbatively. As a check on this we have therefore also used the slightly different value of $\psi = -31°$, which corresponds to $a({}^3P_2) = -0.2554$ fm^3.

Fig. 4.17 shows the residual interaction matrix element $\tilde{V}^{(2)}_{AA}(p)$ as a function of lab kinetic energy after the removal of iterated OPE from four different Nijmegen phase shifts. For both data sets $\tilde{V}^{(2)}_{AA}(p)$ exhibits a strong energy-dependence, indicating the presence of other long-range forces.

After further removing TPE (order-$Q^{2,3}$) and recoil OPE (order-Q^2), however, as shown in Fig. 4.18 we obtain smooth energy-dependences that look like they could be fitted with low-order polynomials. In other words, the results show that to this order all the relevant long-range forces have indeed been removed, and therefore what remains can be parametrised by short-range contact interactions. The results also do indeed demonstrate the redundancy between ψ and the leading energy-independent contact interaction, as a change in ψ has just led to a corresponding shift in the constant terms.

By fitting quadratic (quartic) polynomials (separately) to the two sets of data in Fig. 4.18, in the range 50 - 150 MeV, we obtain scales, from the slopes of the data, of $\sim$ 865 (878) MeV for $a(^3P_2) = -0.2844$ fm^3 and 861 (884) MeV for $a(^3P_2) = -0.2554$ fm^3.

Lastly, an important point to mention is that, unlike for the $^3S_1 - ^3D_1$ coupled channels, the interaction strengths we have presented here for the $^3P_2 - ^3F_2$ channels have been extracted (from the $^3P_2$ eigen phase shift) assuming a single attractive interaction (which is also why we have only presented results for the 'AA' interaction). Our reasoning behind this assumption can be explained by examining the residual interaction matrix elements for this channel extracted in the 'normal' way, i.e. using the $^3P_2 - ^3F_2$ versions of Eqs. (4.75) and (4.76) with all elements (defined in Eq. 4.74) present, as shown in Fig. 4.19. As can be seen in this figure, although at first glance elements $\tilde{V}^{(4)}_{AR}(p)$, $\tilde{V}^{(4)}_{RA}(p)$ and $\tilde{V}^{(4)}_{RR}(p)$ appear larger than $\tilde{V}^{(4)}_{AA}(p)$, especially below 50 MeV, in the region where we are interested in extracting a scale these elements actually pass through zero, whilst $\tilde{V}^{(4)}_{AA}(p)$ is tending to a constant $\sim$ 100 fm^0.

Alternatively, the dominance of the 'AA' element over the other elements can be seen by first rearranging Eq. (4.76) to give

$$\begin{aligned} &\tilde{\mathbf{K}}(p) - \left\langle \mathbf{u}_l^\top(p) | \mathbf{V}^{(2)}_{1\pi} + \mathbf{V}^{(2,3)}_{2\pi} | \mathbf{u}_l(p) \right\rangle \\ &\qquad = \mathbf{u}_l^\top(p, R_0) \left(\mathbf{F_0}^\top\right)^{-1} \tilde{\mathbf{V}}^{(4)}_{(AR)}(p) \mathbf{F_0}^{-1} \mathbf{u}_l(p, R_0), \end{aligned} \tag{4.88}$$

and examining the individual contributions of the four elements of $\tilde{V}^4(p)$ on the RHS of this equation. In Fig. 4.20 we present the contributions to the element that involves the $\tilde{K}_{\alpha\alpha}(p)$ quantity (the other elements show a similar picture). As can be seen in the plot the matrix element with $\tilde{V}^{(4)}_{AA}(p) = 105$ fm^0 does rather

well at reproducing the same quantity that involves the sum of all the matrix elements. This reinforces that our assumption is indeed reasonable.

Looking at Table 2.2 helps to explain the situation. There are two critical momenta for coupled spin-triplet waves. The critical momenta define the point above which the tensor OPE potential needs to be treated non-perturbatively (the higher the energy the more likely to overcome centrifugal barrier and "see" the tensor OPE potential). The ${}^3S_1$-${}^3D_1$ values are both within the energy range of our EFT - implying that both waves will be able to overcome the centrifugal barrier and experience the tensor OPE potential. However, with the ${}^3P_2$-${}^3F_2$ waves this is not the case. Only the ${}^3P_2$ wave is (just) within the the energy range of our EFT. The enhanced power counting mentioned in [65] therefore only applies to the one attractive channel.

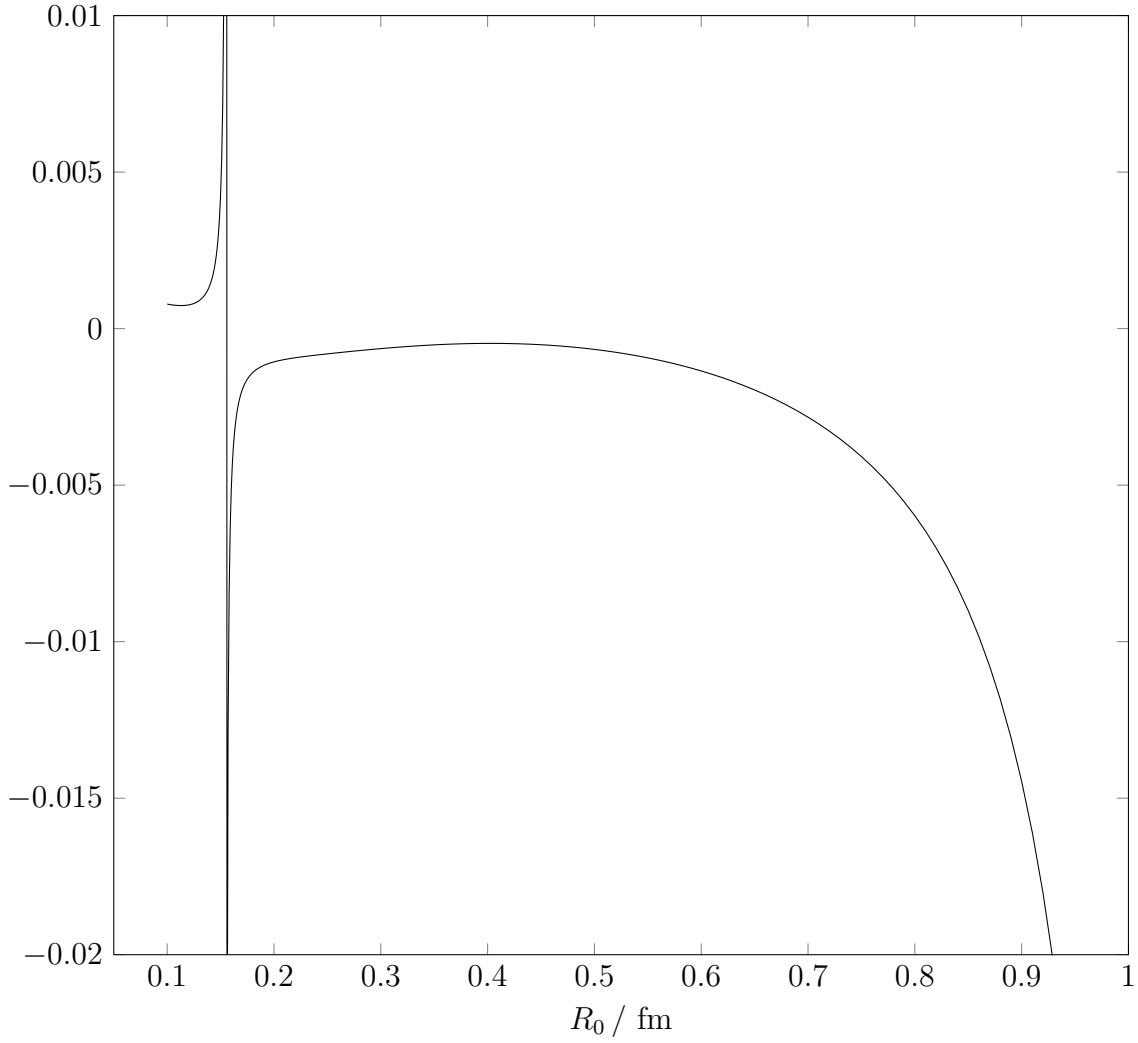

Figure 4.13: The variation of the upper off-diagonal element in the matrix $\mathbf{F_0}^\top \left(\mathbf{F}^\top\right)^{-1}(p, R_0)$ (the ${}^3P_2 - {}^3F_2$ version of Eq. (4.78)) as a function of R_0 ($T = 5$ MeV).

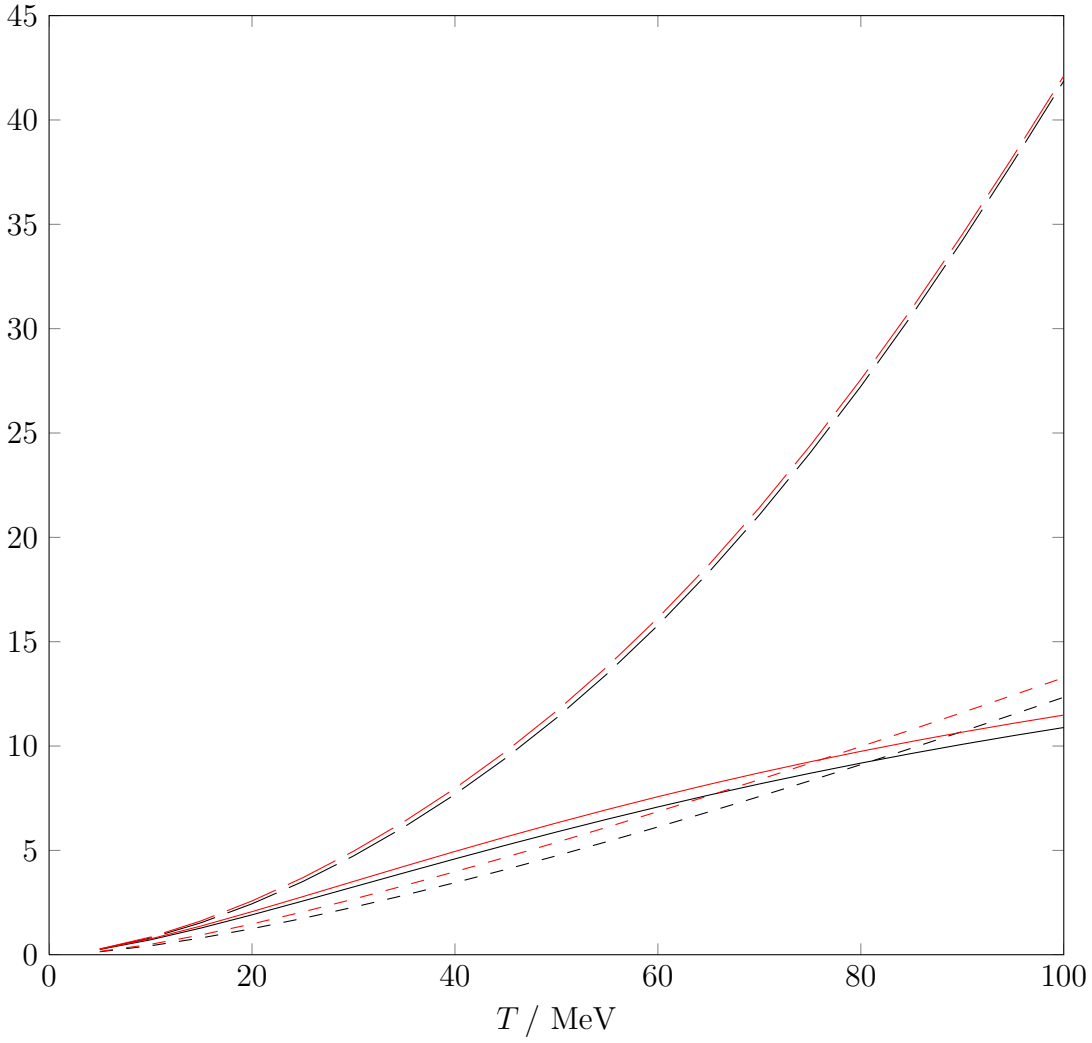

Figure 4.14: ${}^3P_2$ bar (black) and eigen (red) phase shifts (in degrees). The solid curves are from the Nijm1 PWA, the long (short) -dashed curves are due to iterated OPE with a scattering volume fixed at -0.2844 (-0.1448) fm^3.

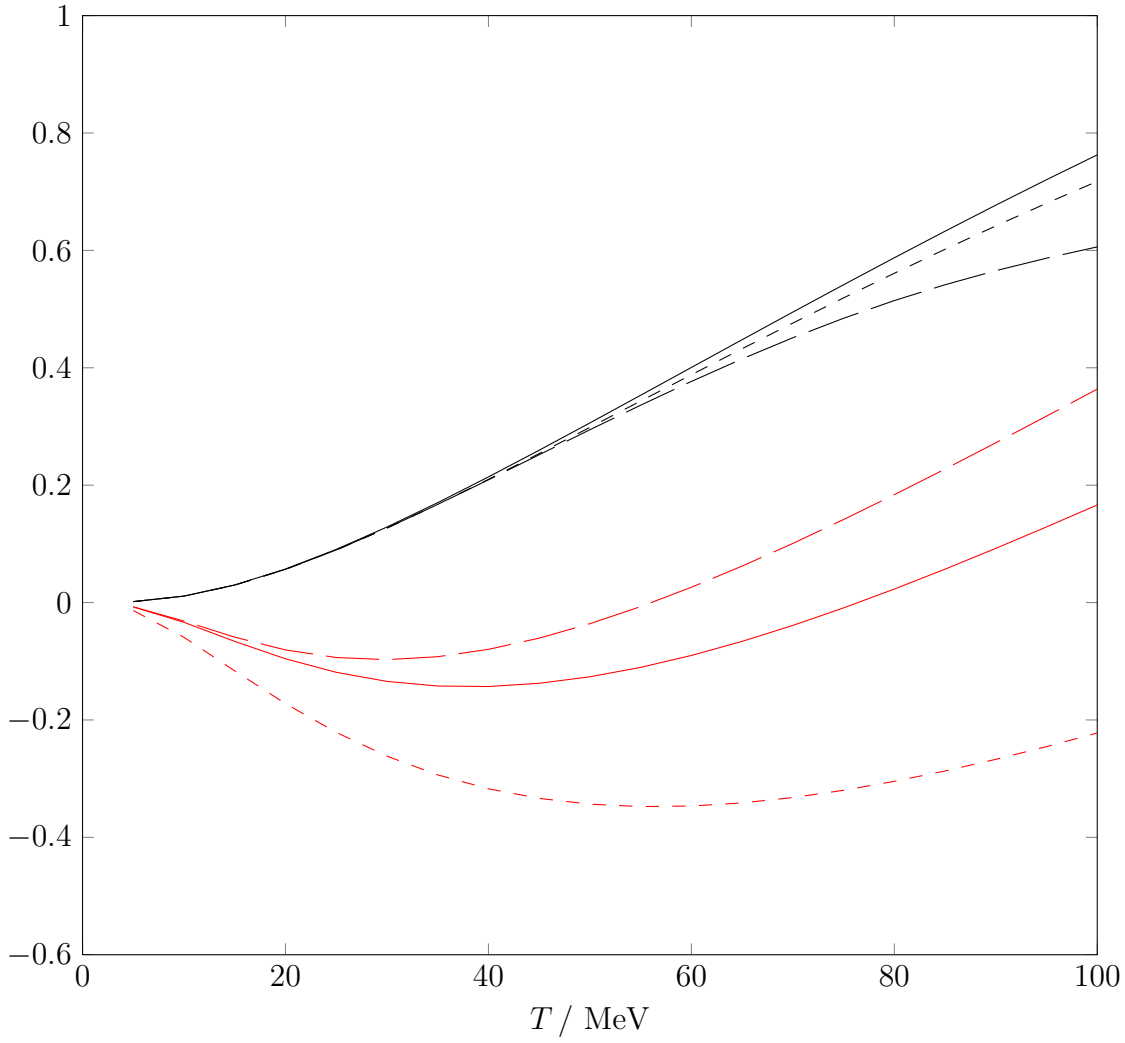

Figure 4.15: ${}^3F_2$ bar and eigen phase shifts (in degrees). See the caption to Fig. 4.14 for further details.

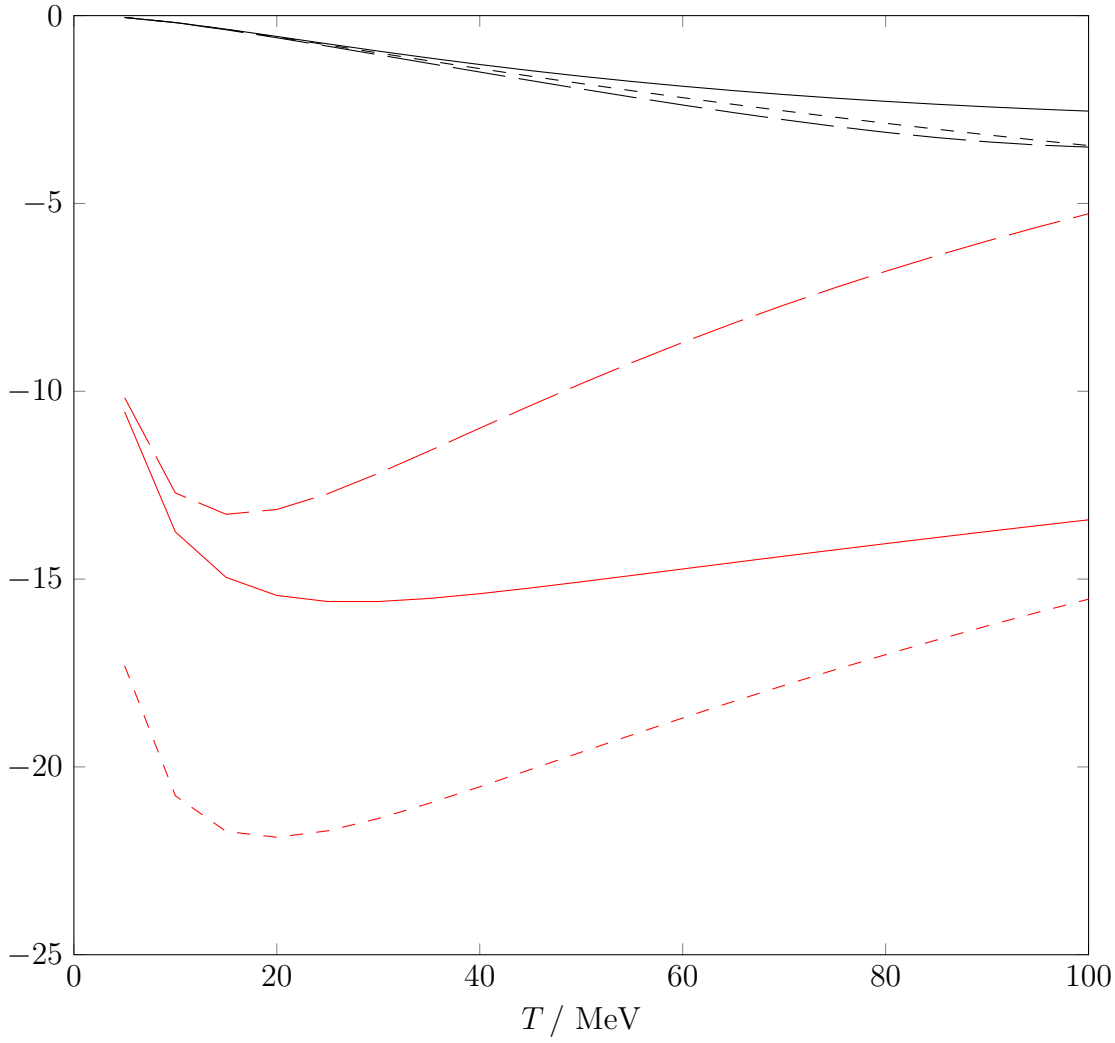

Figure 4.16: ϵ_2 bar and eigen mixing angles (in degrees). See the caption to Fig. 4.14 for further details.

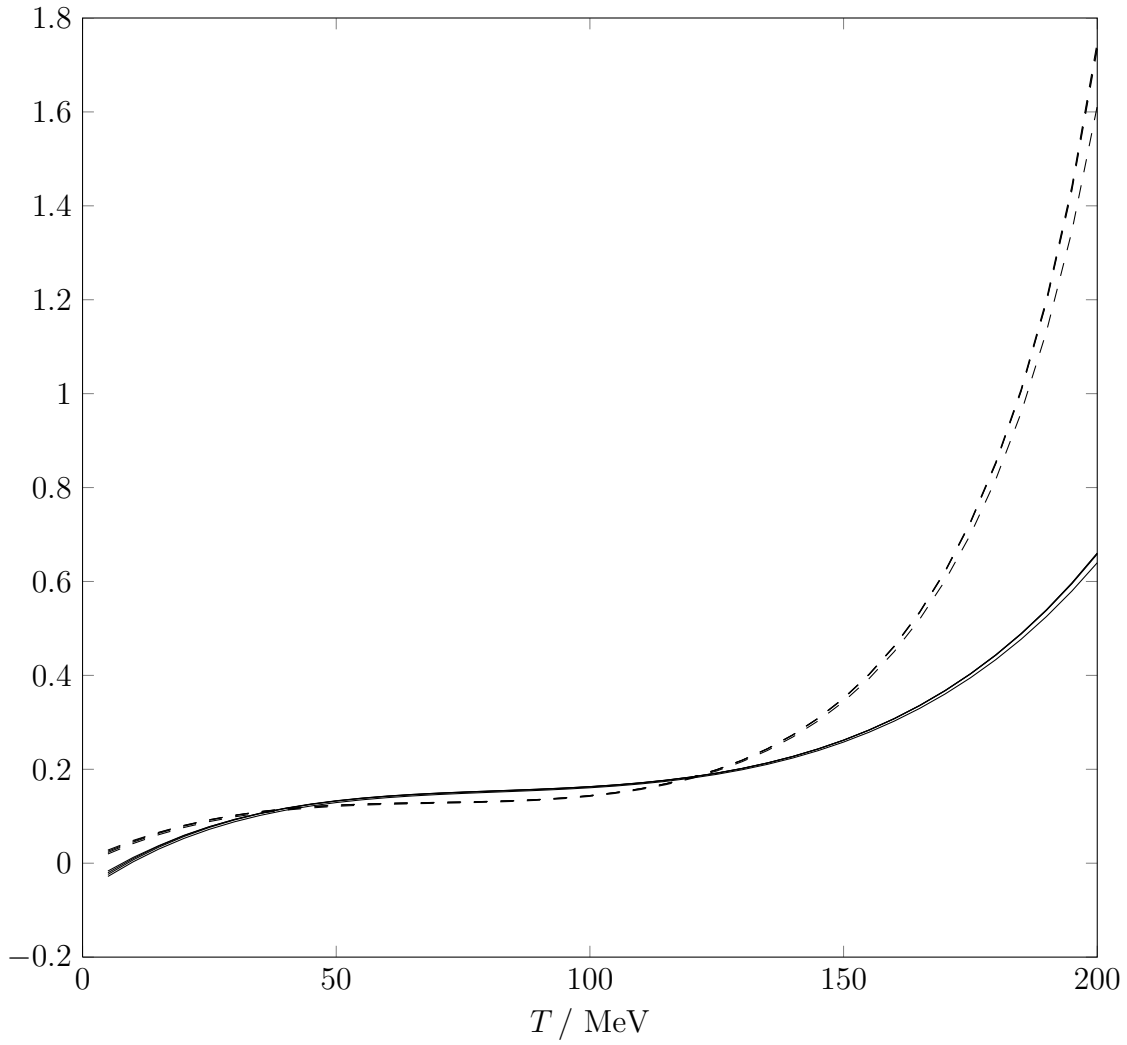

Figure 4.17: The residual interaction matrix element $\tilde{V}^{(2)}_{AA}(p)$, in fm^0, in the ${}^3P_2$−${}^3F_2$ channels, assuming a single attractive interaction, after the removal of iterated OPE from four different Nijmegen phase shifts as a function of lab kinetic energy. We show results for $a({}^3P_2) = -0.2844$ fm^3 (dashed) and -0.2554 fm^3 (solid), both with $R_0 = 0.3$ fm.

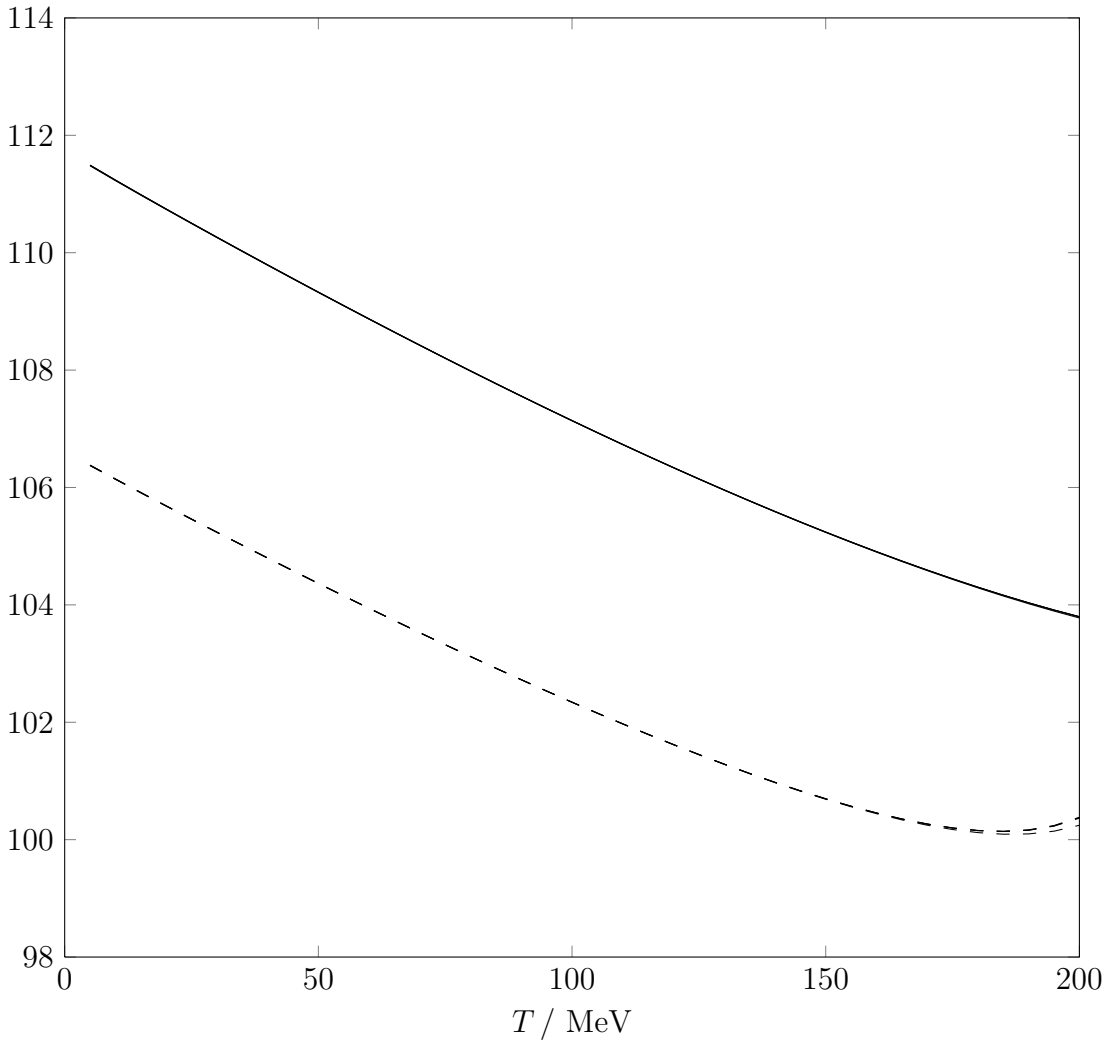

Figure 4.18: The residual interaction matrix element $\tilde{V}^{(4)}_{AA}(p)$, in fm^0, in the ${}^3P_2 - {}^3F_2$ channels, assuming a single attractive interaction, after the removal of OPE and TPE potentials up to order-Q^3 from four different Nijmegen phase shifts as a function of lab kinetic energy. We show results for $a({}^3P_2) = -0.2844$ fm^3 (dashed) and -0.2554 fm^3 (solid), both with $R_0 = 0.3$ fm.

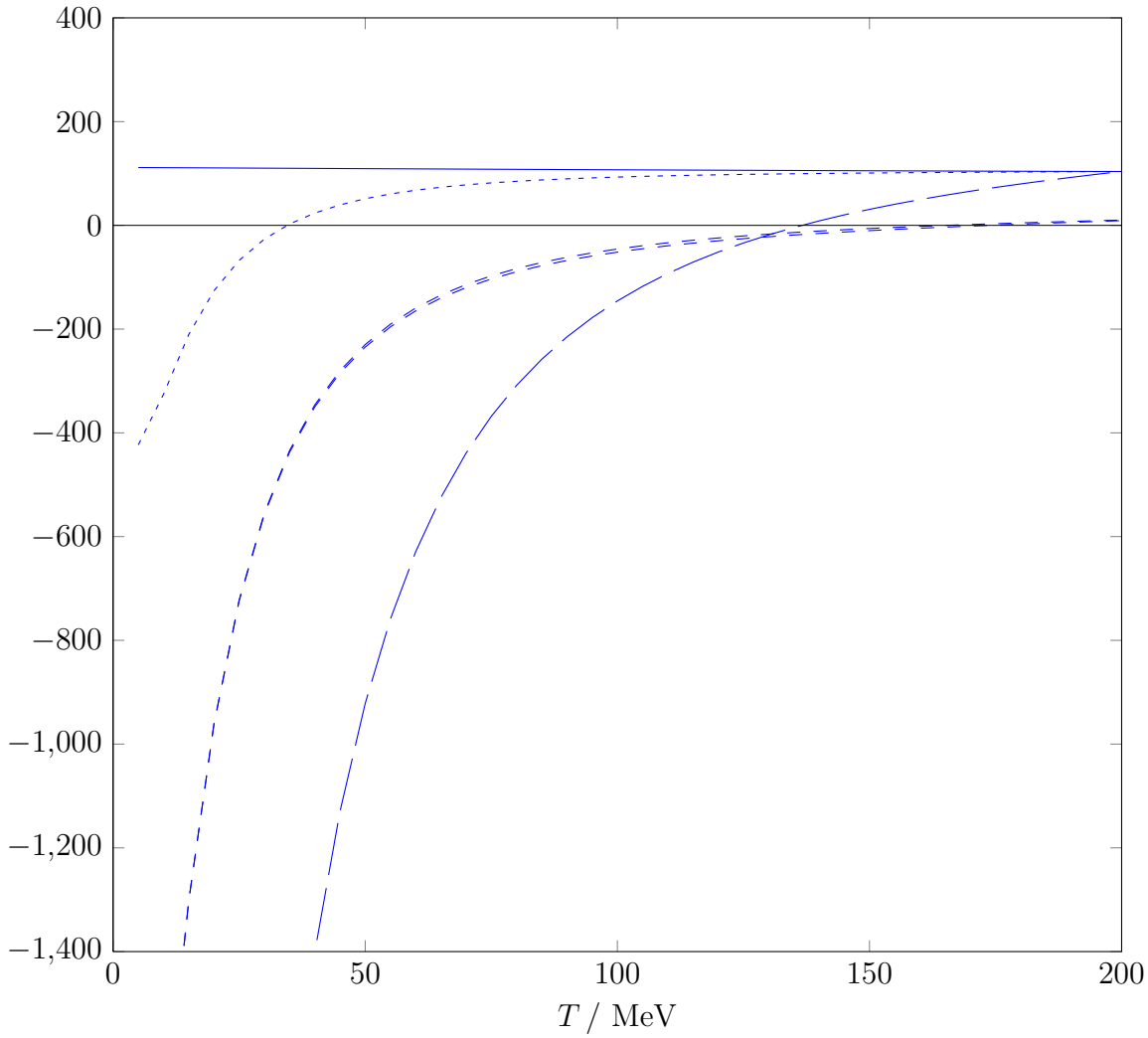

Figure 4.19: The residual interaction matrix elements $\tilde{V}^{(4)}_{AA}(p)$ (short-dashed), $\tilde{V}^{(4)}_{AR}(p)$ and $\tilde{V}^{(4)}_{RA}(p)$ (dashed) and $\tilde{V}^{(4)}_{RR}(p)$ (long-dashed), in fm^0, in the ${}^3P_2 - {}^3F_2$ channels, after the removal of OPE and TPE potentials up to order-Q^3. Also shown, for comparison, is the $\tilde{V}^{(4)}_{AA}(p)$ interaction element extracted assuming a single attractive interaction (solid). All residual interactions have been extracted from the 'Nijm1' phase shifts, and are fit to $a({}^3P_2) = -0.2554$ fm^3, and have a delta-shell radius of $R_0 = 0.3$ fm.

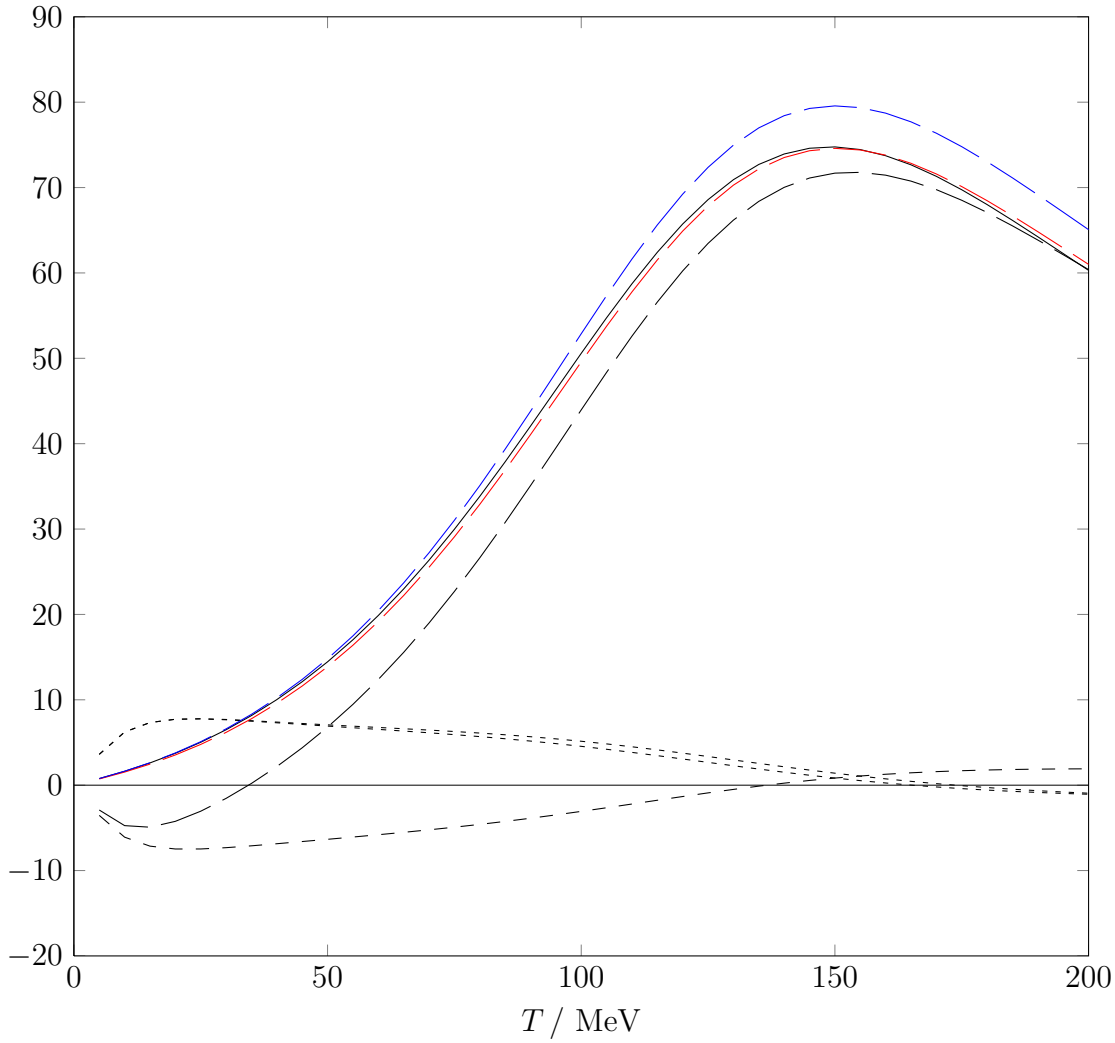

Figure 4.20: Contributions of the individual matrix elements of $\tilde{V}^{(4)}(p)$ on the RHS of Eq. (4.88), in fm^2, that form the quantity $\tilde{K}_{\alpha\alpha}(p)$ minus the relevant DWBA matrix element on the LHS of the equation. The black long-dashed, short-dashed and dashed curves correspond to the contributions involving elements $\tilde{V}^{(4)}_{AA}(p)$, $\tilde{V}^{(4)}_{AR}(p)$ and $\tilde{V}^{(4)}_{RA}(p)$ and $\tilde{V}^{(4)}_{RR}(p)$ respectively, while the solid black curve is the sum of these contributions. The red (blue) long-dashed curves correspond to setting $\tilde{V}^{(4)}_{AA}(p)$ to a constant value of 105 (112). We have used $a(^3P_2) = -0.2554$ fm^3 and $R_0 = 0.3$ fm.

Chapter 5

NN Bound State: the Deuteron

5.1 Introduction

The deuteron, the nucleus of deuterium (an isotope of hydrogen) was discovered by Harold Urey in 1932. It is the only stable bound state containing two nucleons. This makes it an ideal system in which to study the nuclear force, as it is the simplest case. It is loosely bound (it has the smallest binding energy/nucleon of any nuclide), so much so that it cannot support an excited state. The deuteron wave function is not completely spherically symmetric, it has a D-state admixture. The evidence for this is: (i) the magnetic moment is not simply equal to the sum of the magnetic moments of the neutron and proton and (ii) the quadrupole moment non-zero.

5.2 Zeroth-Order Deuteron Wave Functions

The zeroth-order[1] deuteron wave functions are obtained in a similar way to the distorted eigen wave functions in the previous chapter. As usual, the starting point is to solve a pair of coupled radial Schödinger equations, in this case given by

$$\left(\frac{\mathrm{d}^2}{\mathrm{d}r^2} - \gamma^2 - U_{\pi C}(r)\right) u_B^{(0)}(r) = 2\sqrt{2}U_{\pi T}(r) w_B^{(0)}(r) \tag{5.1}$$

and

[1]Zeroth-order here implies that the solutions result from iterated OPE and fixing the short-distance phase parameter, i.e. that they result from a leading-order calculation.

$$\left(\frac{\mathrm{d}^2}{\mathrm{d}r^2} - \gamma^2 - U_{\pi C}(r) + 2U_{\pi T}(r) - \frac{6}{r^2}\right) w_B^{(0)}(r) = 2\sqrt{2}U_{\pi T}(r)u_B^{(0)}(r), \qquad (5.2)$$

where the only differences between these and Eqs. (4.7) and (4.8) are that we have exchanged p for $i\gamma$,[2] so that $p^2 \to -\gamma^2$, implying that we are working at negative energies, and denote $u_B^{(0)}$ and $w_B^{(0)}$ to correspond to the bound state S and D solutions, respectively. This means, of course, that the short-distance wave functions in the bound state case here have exactly the same form as the short-distance wave functions in the scattering case defined in Eqs. (4.21) and (4.22), the only difference, as already stated, is that we replace p with $i\gamma$.

Now, the distorted eigen waves in the previous chapter were obtained by forming linear combinations of two independent pairs of solutions ((u_1, w_1) and (u_2,w_2)) in such a way that they had the required behaviour for large r (in that case so that the u and w eigen waves had the same phase as $r \to \infty$). We take the same approach here.

For large r (outside the range of the OPE potentials) the bound state solutions to Eqs. (5.1) and (5.2) are the spherical Hankel functions of the first kind, denoted $rh_0^{(1)}(i\gamma r)$ and $rh_2^{(1)}(i\gamma r)$, respectively[3] (see e.g. Ref. [88]). These solutions vanish for $r \to \infty$, as required for bound states. They are normalised to the following forms

$$\begin{aligned} u_B^{(0)}(r) &\to A_S e^{-\gamma r} \\ w_B^{(0)}(r) &\to A_D e^{-\gamma r}\left(1 + \frac{3}{\gamma r} + \frac{3}{(\gamma r)^2}\right), \end{aligned} \qquad (5.3)$$

where A_S and A_D are the asymptotic normalisations, whose ratio, called the d/s ratio is denoted by $\eta = A_D/A_S$, these are physical observables that are measurable. The wave functions in this region can be thought of as observable, similar to scattering waves extending out to infinity.

However, general solutions to Eqs. (5.1) and (5.2) contain contributions from

[2] $\gamma = \sqrt{MB}$ is the deuteron wave number, where M is the nucleon mass, and B is the deuteron binding energy. At the moment, we class it as an unspecified parameter that will be determined (its zeroth-order value anyway) by finding the bound state solutions to Eqs. (5.1) and (5.2).

[3] They have been multiplied by r since we are working with 'reduced' wave functions.

the spherical Hankel functions of the second kind, denoted $rh_0^{(2)}(i\gamma r)$ and $rh_2^{(2)}(i\gamma r)$, respectively, which blow up as $r \to \infty$. We therefore require that our two independent pairs of solutions are combined in such a way that the resulting solutions contain no such growing terms. To see how this is accomplished, we first write our two independent pairs of solutions, for $r \to \infty$, as

$$\begin{aligned} u_1 &\to r\left(-A_1 h_0^{(1)} + B_1 h_0^{(2)}\right) \\ w_1 &\to r\left(C_1 h_2^{(1)} + D_1 h_2^{(2)}\right) \end{aligned} \tag{5.4}$$

and

$$\begin{aligned} u_2 &\to r\left(-A_2 h_0^{(1)} + B_2 h_0^{(2)}\right) \\ w_2 &\to r\left(C_2 h_2^{(1)} + D_2 h_2^{(2)}\right), \end{aligned} \tag{5.5}$$

where the various coefficients A_1, B_1 etc. are obtained in the usual way by computing the logarithmic derivatives of the solutions and doing some algebra. The solutions in Eqs. (5.4) and (5.5) can then be linearly combined to give,

$$\begin{aligned} Cu_1 + Du_2 &= -r\left(CA_1 + DA_2\right) h_0^{(1)} + r\left(CB_1 + DB_2\right) h_0^{(2)} \\ &= -rA_u h_0^{(1)} + rB_u h_0^{(2)} \end{aligned} \tag{5.6}$$

and

$$\begin{aligned} Cw_1 + Dw_2 &= -r\left(CC_1 + DC_2\right) h_0^{(1)} + r\left(CD_1 + DD_2\right) h_0^{(2)} \\ &= -rC_w h_0^{(1)} + rD_w h_0^{(2)} \end{aligned} \tag{5.7}$$

where, as before for the distorted eigen waves, we want to find the values of C and D (remembering that only the ratio of these matters) that give us the required behaviour for large r. So, to remove the exponentially growing terms from the combined solutions, whose coefficients we have defined above as B_u and D_w, we

	NijmI	NijmII	Reid93	PWA93
B [MeV]	-2.224575	-2.224575	-2.224575	-2.224575
A_S [fm$^{1/2}$]	0.8841	0.8845	0.8853	0.8847
$\eta = A_D/A_S$	0.02534	0.02521	0.02514	0.02544
Q_d [fm^2]	0.2719	0.2707	0.2703	–
r_m [fm]	1.967	1.968	1.969	–
$P_D(\%)$	5.664	5.635	5.699	–

Table 5.1: Deuteron parameters for four different Nijmegen analyses [92].

can, for example,[4] set $D_w = 0$, implying that $CD_1 + DD_2 = 0$ and therefore that $D = -CD_1/D_2$. Thus, (arbitrarily) letting $C = 1$, we can obtain a value for D. Finally, one can use a method of choice (we used the 'secant' method in Ref. [103]) to vary γ until $B_u = 0$ (or at least zero to a desired accuracy). Only at this "special" energy can this be achieved. Since γ is related to the deuteron binding energy by $\gamma = \sqrt{MB}$, this means that, using this method, we have simultaneously obtained our leading-order estimate for the deuteron binding energy, which we denote $E_B^{(0)}$, and after normalising our solutions by requiring that

$$\int_0^\infty \left(u_B^{(0)}(r)^2 + w_B^{(0)}(r)^2 \right) \mathrm{d}r = 1 \tag{5.8}$$

we have obtained A_S, A_D (and therefore η), and the zeroth-order deuteron wave functions.

5.3 Deuteron Parameters

Once the properly normalised zeroth-order deuteron bound state wave functions have been obtained (along with the leading-order binding-energy $E_B^{(0)}$, the asymptotic normalisations A_S, A_D, and therefore η), they can be used to calculate other deuteron parameters, which can then be compared to parameters provided by the Nijmegen group (see Table 5.1). However, note that as discussed in Ref. [101], some of these parameters differ slightly from their experimentally measured values (mainly Q_D).

The quadrupole moment of the deuteron, Q_D, is given by

[4] This is how we did it but there are other slight alternative ways that produce the same result.

$$Q_D = \frac{1}{\sqrt{50}} \int_0^\infty r^2 w_B(r)(u_B(r) - \frac{1}{2\sqrt{2}} w_B(r))\,\mathrm{d}r, \tag{5.9}$$

whose (small) non-zero value provided the first experimental evidence that the nuclear force has a non-central component [104] [105]. It is a parameter that is related to the shape of a charge distribution, where, for example, a completely spherically symmetrical distribution would be indicated by zero quadrupole moment. The fact that for the deuteron it is non-zero but small, implies that it is nearly spherically symmetric. This further suggests that it is predominantly an S-state, with only a small admixture of the D-state.

The deuteron matter radius, r_m, is defined as

$${r_m}^2 = \frac{1}{4}\left\langle r^2 \right\rangle = \frac{1}{4}\int_0^\infty r^2(u_B(r)^2 + w_B(r)^2)\,\mathrm{d}r. \tag{5.10}$$

Both r_m and Q_d are observables. They get significant contributions from the (large r) tail ends of the wave functions (due to the r^2 factors in the integrals). At higher orders in an EFT, these variables strictly speaking need more care since there will be other short-distance contributions. For example, included in the definition of the quadrupole moment given in Eq. (5.9) is the coupling between the deuteron wave functions and a single photon. However, there are more terms that contribute, such as a photon coupling to a momentum-dependent contact operator, or a photon coupling to charged pion exchange (see e.g Ref. [106]). To properly calculate Q_D in an EFT these sorts of terms must be accounted for. N.B. we do not calculate the D-state probability, P_D, as it is not an observable.

Having calculated some deuteron properties at leading-order, the next logical step is to try to improve on things by including the influence of higher-order terms in the NN potential. This can be done, as we show below, by calculating deuteron wave functions at first-order in perturbation theory, in which the perturbing potential is the combination of TPE at order-$Q^{2,3}$, recoil OPE at order-Q^2 and the delta-shell potential at order-Q^4 (Eq. (4.73)) whose "strength" (as a function of energy) we extracted from the ${}^3S_1 - {}^3D_1$ eigen phase shifts in the previous chapter using Eq. (4.76) (shown in Figs. 4.10, 4.11 and 4.12). The first-order deuteron wave functions can then be used, in combination with the zeroth-order wave functions, to re-calculate the deuteron properties.

5.4 First-Order Wave Functions: the Dalgarno and Lewis Method

To determine deuteron wave functions to first-order in perturbation theory we use a method first developed by Dalgarno and Lewis in Ref. [107]. The method is described well in the standard text book on Quantum Mechanics by Schiff [108], however, we reproduce it here for ease of reference.

One begins with the standard result for the second-order energy correction for a non-degenerate system, given by[5]

$$E_0^{(2)} = \sum_{n\neq 0} \frac{\langle 0|H'|n\rangle \langle n|H'|0\rangle}{E_0^{(0)} - E_n^{(0)}}. \tag{5.11}$$

Now suppose we can define an operator, F, such that

$$\frac{\langle n|H'|0\rangle}{E_0^{(0)} - E_n^{(0)}} = \langle n|F|0\rangle\,, \tag{5.12}$$

then we can write Eq. (5.11) as

$$\begin{aligned} E_0^{(2)} &= \sum_{n\neq 0} \langle 0|H'|n\rangle \langle n|F|0\rangle \\ &= \langle 0|H'F|0\rangle - \langle 0|H'|0\rangle \langle 0|F|0\rangle \end{aligned} \tag{5.13}$$

where the $n = 0$ term has been added and subtracted out in order to use $\sum_n |n\rangle \langle n| = 1$. The evaluation of $E_0^{(2)}$ in its new form has been highly simplified (provided F can be determined), as the infinite summation has been replaced with integrals over the unperturbed state. This demonstrates the strength of the method because it can be used to calculate quantities to any order in perturbation theory exactly (i.e. no truncation of an infinite summation is necessary).

Proceeding further Eq. (5.12) can be rewritten as

$$\begin{aligned} \langle n|H'|0\rangle &= \left(E_0^{(0)} - E_n^{(0)}\right) \langle n|F|0\rangle \\ &= \left\langle n\right| \left[F, H^{(0)}\right] \left|0\right\rangle \end{aligned} \tag{5.14}$$

[5] See Appendix E for derivation.

where $H^{(0)}$ is the unperturbed Hamiltonian (see Eq. (E.1)). Now the above equation is valid if $\left[F, H^{(0)}\right] = H' + C$, where C is just a constant. Acting with this operator on the ket vector $|0\rangle$ gives

$$\left[F, H^{(0)}\right] |0\rangle = H' |0\rangle + C |0\rangle , \tag{5.15}$$

where further applying the bra vector $\langle 0|$, and using the easily proven relation that $\langle 0| \left[F, H^{(0)}\right] |0\rangle = 0$, it can be shown that $C = -\langle 0|H'|0\rangle = -E_0^{(1)}$, where $E_0^{(1)}$ is the first-order to correction to the bound state energy.

Defining a new ket vector given by $|0^{(1)}\rangle \equiv F |0\rangle$, Eq. (5.15) can be written in the form of an inhomogeneous equation,

$$\left(E_0^{(0)} - H^{(0)}\right) |0^{(1)}\rangle = \left(H' - E_0^{(1)}\right) |0\rangle . \tag{5.16}$$

Any admixture of $|0\rangle$ can be added to $|0^{(1)}\rangle$, because $|0\rangle$ is the solution of the unperturbed Hamiltonian. However, the choice is made such that $\langle 0|0^{(1)}\rangle = 0$. Thus if one can solve Eq. (5.16) for $|0^{(1)}\rangle$, then the equation for the second-order energy correction, Eq. (5.13) can be further simplified to give

$$E_0^{(2)} = \langle 0|H'|0^{(1)}\rangle , \tag{5.17}$$

and so we have overcome the need to calculate F. Finally, and most importantly for us, the first-order correction to the wave function, $\psi_0^{(1)}$, in Eq. (E.9) can be exactly related to $|0^{(1)}\rangle$ by writing

$$\begin{aligned} \psi_0^{(1)} &= \sum_{n\neq 0} |n\rangle \frac{\langle n|H'|0\rangle}{E_0^{(0)} - E_n^{(0)}} \\ &= \sum_{n\neq 0} |n\rangle \langle n|F|0\rangle \\ &= F |0\rangle - |0\rangle \langle 0|F|0\rangle \\ &= |0^{(1)}\rangle , \end{aligned} \tag{5.18}$$

where again we have used the trick to add and subtract the term with $n = 0$ to make the summation complete (including all values of n in the summation). Therefore, instead of evaluating the first-order correction to the wave function, $\psi_0^{(1)}$, by truncating the infinite summation in Eq. (E.9), the Dalgarno and Lewis approach has replaced this method by the more accurate method of solving an

inhomogeneous differential equation (Eq. (5.16)).

5.5 First-Order Deuteron Wave Functions

To obtain the deuteron wave functions at first-order in perturbation theory, we start by solving the following Schrödinger (matrix) equation for the first-order perturbation to the wave function $\mathbf{u_B^{(1)}}$ (c.f. Eq. (5.16)),

$$\left(\mathbf{E_B^{(0)}} - \mathbf{H_0}\right) \mathbf{u_B^{(1)}} = \left(\mathbf{H'} - \mathbf{E_B^{(1)}}\right) \mathbf{u_B^{(0)}}, \tag{5.19}$$

where $\mathbf{E_B^{(0)}}$, $\mathbf{H_0}$ and $\mathbf{u_B^{(0)}}$ denote the leading-order binding-energy, Hamiltonian and deuteron wave functions respectively (in matrix form),[6] and satisfy the leading-order Schrödinger (matrix) equation $\left(\mathbf{E_B^{(0)}} - \mathbf{H_0}\right) \mathbf{u_B^{(0)}} = \mathbf{0}$ used previously (i.e. Eqs. (5.1) and (5.2)). The perturbing Hamiltonian matrix, denoted $\mathbf{H'}$, is defined as

$$\mathbf{H'} = \mathbf{V}_{2\pi}^{(2,3)} + \mathbf{V}_{1\pi}^{(2)} + \mathbf{V}^s(\gamma, r), \tag{5.20}$$

where $\mathbf{V}_{2\pi}^{(2,3)}$ and $\mathbf{V}_{1\pi}^{(2)}$ are the usual TPE and recoil OPE potentials respectively, and $\mathbf{V}^s(\gamma, r)$ is the delta-shell potential defined in Eq. (4.73), whose elements $\tilde{V}_{AA}^{(4)}(\gamma)$, $\tilde{V}_{AR}^{(4)}(\gamma)$, $\tilde{V}_{RA}^{(4)}(\gamma)$, and $\tilde{V}_{RR}^{(4)}(\gamma)$ are obtained by extrapolating the curves in Figs. 4.10, 4.11 and 4.12 to the corresponding negative energy where our bound state is situated. We also have in Eq. (5.19), the first-order correction to the binding energy, $\mathbf{E_B^{(1)}} = E_B^{(1)}\mathbf{1}$, which is calculated using standard first-order perturbation theory,

$$E_B^{(1)} = \int_0^\infty \left(\mathbf{u_B^{(0)}}\right)^\top \mathbf{H'}\, \mathbf{u_B^{(0)}} \mathrm{d}r, \tag{5.21}$$

To solve Eq. (5.19) we treat it as an inhomogeneous differential matrix-equation. As usual there are two regions where we impose boundary conditions to match the numerical solutions onto known asymptotic forms.

Starting with the 'small-r' region, we use the same initial conditions that are used for the homogeneous (leading-order) differential equations, to again produce two sets of independent (first-order) wavefunctions, except that as our delta-shell

[6] Note that $\mathbf{u_B^{(0)}} = \begin{pmatrix} u_B^{(0)}(r) \\ w_B^{(0)}(r) \end{pmatrix}$ and $\mathbf{u_B^{(1)}} = \begin{pmatrix} u_B^{(1)}(r) \\ w_B^{(1)}(r) \end{pmatrix}$.

potential happens to be located at our matching radius, i.e. $R_0 = R_m = 0.3$ fm, we also take into account the discontinuity in the derivatives of the wave functions that it produces at this point (note that after we obtained our particular solutions we did check that they were independent of our boundary conditions).

In the 'large-r' region, we match the numerical solutions onto Hankel functions extracting the corresponding asymptotic coefficients in the process. Now as with the unperturbed deuteron wave functions, the two sets of independent first-order wave functions need to be combined in such a way that there are no growing Hankel terms for $r \to \infty$. For the unperturbed case, we chose to set the coefficient of the growing Hankel function in the w-wave (denoted D_w, see Eq. (5.7)) to zero, which implied that $D = -CD_1/D_2$, and therefore by arbitrarily setting $C = 1$, we obtained a value for D. We then varied γ until the growing Hankel function in the u-wave (denoted B_u, see Eq. (5.6)) became zero.

In the perturbed case, it is slightly different, as we have the constraint that $C^{(1)} + D^{(1)} = 1$, where $C^{(1)}$ and $D^{(1)}$ are the coefficients of the two-independent solutions of the inhomogeneous equation (Eq. (5.19)), i.e. any linear combination that satisfies the same equation must have $C^{(1)} + D^{(1)} = 1$, otherwise we would in effect be solving a different problem - this did not matter for the homogeneous case of course.

So, imposing this constraint, if we choose to set $D_w^{(1)}$ to zero, then we get

$$C^{(1)} = \frac{D_2^{(1)}}{D_2^{(1)} - D_1^{(1)}} \qquad D^{(1)} = \frac{-D_1^{(1)}}{D_2^{(1)} - D_1^{(1)}}, \tag{5.22}$$

and for the corresponding $B_u^{(1)}$ coefficient to be zero it is therefore required that the condition $B_1^{(1)}/B_2^{(1)} = D_1^{(1)}/D_2^{(1)}$ is true. Now this condition should be true, however, any numerical error in $E_B^{(1)}$ can lead to a growing Hankel function in the solution. Hence one might need to fine-tune the value of $E_B^{(1)}$ to avoid this (we used the secant method again).

Now, we are not quite finished yet, there is one last step to obtain the deuteron wave functions at first-order in perturbation theory. This is because in our inhomogeneous differential equation (Eq. (5.19)) the perturbed solutions contain an arbitrary admixture of the unperturbed (leading-order) bound state solutions, which need to be removed so that we obtain the so-called 'particular' solutions.

To achieve this we impose the condition that the first-order perturbation to the wave function should be orthogonal to the unperturbed (zeroth-order) wave

	$R_m = 0.3$ fm, $\psi = -60.1391°$	$R_m = 0.35$ fm, $\psi = -60.1393°$
$E_B^{(0)}$ [MeV]	-2.138954	-2.138939
$A_S^{(0)}$ [fm$^{1/2}$]	0.855181	0.855179
$A_D^{(0)}$ [fm$^{1/2}$]	0.02178720	0.02178704
$\eta^{(0)} = A_D^{(0)}/A_S^{(0)}$	0.02547671	0.02547658
$Q_d^{(0)}$ [fm^2]	0.2783252	0.2783290
$r_m^{(0)}$ [fm]	1.963928	1.963934

Table 5.2: Leading-order deuteron parameters for two different matching radii R_m (the corresponding short-distance phases ψ are both fit to $a(^3S_1)$ =5.420 fm).

function. We write our inhomogeneous solution as $\mathbf{u_B^{(1)}} = A\mathbf{u_B^{(0)}} + \tilde{\mathbf{u}}_\mathbf{B}^{(1)}$, where $\tilde{\mathbf{u}}_\mathbf{B}^{(1)}$ is the particular solution we want, and A is the overlap of $\mathbf{u_B^{(1)}}$ with the lowest-order wave function, i.e.

$$\left\langle \mathbf{u_B^{(0)}} | \mathbf{u_B^{(1)}} \right\rangle = A, \tag{5.23}$$

since $\left\langle \mathbf{u_B^{(0)}} | \mathbf{u_B^{(0)}} \right\rangle = 1$ and $\left\langle \mathbf{u_B^{(0)}} | \tilde{\mathbf{u}}_\mathbf{B}^{(1)} \right\rangle = 0$. The particular solution we want $\tilde{\mathbf{u}}_\mathbf{B}^{(1)}$, is therefore simply given by

$$\tilde{\mathbf{u}}_\mathbf{B}^{(1)} = \mathbf{u_B^{(1)}} - \left\langle \mathbf{u_B^{(0)}} | \mathbf{u_B^{(1)}} \right\rangle \mathbf{u_B^{(0)}}. \tag{5.24}$$

5.6 Results and Discussion

We present our deuteron results here. Starting with the leading-order calculations, we show the deuteron wave functions in Fig. 5.1 and more importantly the deuteron properties in Table 5.2. In Table 5.2, we show results for two different matching radii (with the short-distance phase parameters for both fixed to give $a(^3S_1) = 5.420$ fm), to give some measure to the kind of errors we might have, especially as we were concerned in the previous chapter that there was a slight dependence of the asymptotic quantities on the matching radius. Comparing our values to those in Table 5.1 one can see that just iterated OPE and fixing the phase of the short-distance parameter does quite an unexpectedly good job, especially for η and r_m.

For use in the first-order deuteron calculations, the elements of the delta-shell interaction matrix in Figs. 4.10, 4.11 and 4.12 needed to be extrapolated to the deuteron binding energy. For $\tilde{V}^{(4)}_{AA}$ we fitted polynomials of different orders to the data to allow us to properly extrapolate to the deuteron binding energy. Table 5.3 shows the results of the fits, demonstrating a good convergence as more terms are added to the polynomials (as usual keeping clear of the lowest and highest energy regions). Therefore for our results we set $\tilde{V}^{(4)}_{AA} = 42.84441$ fm^0. For the off-diagonal elements $\tilde{V}^{(4)}_{AR} = \tilde{V}^{(4)}_{RA}$ we estimate a value of 0.005 fm^0 extrapolated from the region where the extracted values are roughly constant. Finally for the $\tilde{V}^{(4)}_{RR}$ element it looks like values in the range $0.001 - 0.004$ fm^0 are all plausible. However, this does depend on whether the rather strong looking energy-dependence is real physics and not just artefacts of the Nijmegen fits.

By fitting this element to the deuteron binding energy, we obtained a value of $\tilde{V}^{(4)}_{RR} = 0.00354$ fm^0, which is in good agreement with the visual impression of the range we get from the plot. To get an indication of the sensitivities the deuteron observables experience with regards to the values of these short-distance elements, we looked at three different cases. The first case includes only the V_{AA} matrix element, the second case includes the off-diagonal elements V_{AR}, V_{RA} as well, and in the third case all elements are present (the final case being also fit to the deuteron binding energy as mentioned).

In Fig. 5.2 we show the first-order deuteron wave functions for the three different cases we are dealing with, as described in the caption. It should be stated that the region below about 1 fm should not be taken too seriously of course, as an EFT can not expected to be able to describe this region, and observables should not depend on it significantly. However, importantly the different cases do converge as r gets larger, suggesting that observables that get their significant contributions from larger-r may agree for the three cases, even though they look substantially different at smaller radii. For the three cases in the figure to tend to zero as $r \to \infty$ the first-order energy corrections required for this, imply that the deuteron energies are given by those in Table 5.4. For the $\tilde{V}_{AA}$ element alone, the energy correction is under predicted, and for the case including the off-diagonal elements, it is over predicted. However, one has some freedom to vary the values of elements in the delta-shell potential to fix to the deuteron binding energy, but we found that this did not impact things greatly in terms of the values of the observables.

Polynomial	$\tilde{V}_{AA}^{(4)}(\gamma)$ [fm^0]
Linear	42.78191
Quadratic	42.83512
Cubic	42.84481
Quartic	42.84441

Table 5.3: Values of $\tilde{V}_{AA}^{(4)}$ extrapolated to the LO deuteron binding energy using different orders of polynomials fit to the data in Fig. 4.10 in the lab kinetic energy range 50 - 200 MeV.

	A_S [fm$^{1/2}$]	η	E_B [MeV]
LO	0.8552	0.02548	-2.1389
V_{AA}	0.9097	0.02276	-2.1602
V_{AA}, V_{AR}, V_{RA}	0.8728	0.02217	-2.3463
All	0.8952	0.02325	-2.224575
NijmI	0.8841	0.02534	-2.224575
NijmII	0.8845	0.02521	-2.224575

Table 5.4: Asymptotic normalisation of the deuteron A_S, $\eta = A_D/A_S$, and the deuteron binding energy E_B, to lowest and first order in perturbation theory. We also show empirical values from two Nijmegen fits for comparison.

	$0 \to 30$ fm	$0 \to 10$ fm	$0.8 \to 30$ fm
LO	0.27833		
V_{AA}	0.27538	0.27511	0.27695
V_{AA}, V_{AR}, V_{RA}	0.25290	0.25803	0.25479
All	0.27695	0.27774	0.27840
NijmI	0.2719		
NijmII	0.2707		

Table 5.5: Quadrupole moment of the deuteron Q_d (in fm^2) to lowest and first order in perturbation theory, for three different integration limits for the perturbation integral.

Now to the first-order deuteron properties we obtained. We extracted the asymptotic normalisations (and therefore the d/s ratio) given in Table 5.4. These were extracted at $r = 10$ fm, a relatively small value (compared to the 30 fm - the upper limit we take for our integrals). This was because we also extracted the asymptotic normalisations at slightly different values, to compare, which revealed a linear dependence on these coefficients. We believe this is due to secular perturbations (which we have not accounted for in our calculations). These secular perturbations have the form of r times the exponential of our LO wave function, and therefore lead to a small term linear in r in the coefficients of our asymptotic waves. To ensure as little 'contamination' as possible from this (i.e. to keep the secular term as small as possible), we therefore extract our asymptotic coefficients at the smallest radius possible, whilst ensuring that we do not cut off the potential. To be able to do this, it is important that our first-order shifts in energy are small (which they are). The A_S values have all improved from the leading-order value. The A_D on the other hand is too well described at leading-order, there must be cancellations between the corrections to it. Therefore it is not surprising that A_D (and therefore η) are less well described at higher orders.

We also show in Tables 5.5 and 5.6 the values of the quadrupole moment and the matter radius to first order. As with the first-order wave functions in Fig. 5.2, we calculated values for three cases (four for Q_d), for the inclusion of the different elements in the delta-shell potential. Whilst the $Q_d^{(1)}$ values have all moved in the correct direction from our leading-order value towards the Nijmegen values, some have moved too far, and others not enough.

The r_m values we have in Table 5.6 are all consistently on the large side. This probably means that our leading-order wave function has too long a tail

	$0 \to 30$ fm	$0 \to 10$ fm	$0.8 \to 30$ fm
LO	1.9639		
V_{AA}	2.0763	2.0584	2.0781
V_{AA}, V_{AR}, V_{RA}	2.0134	2.0262	2.0151
All	2.0526	2.0457	2.0543
NijmI	1.967		
NijmII	1.968		

Table 5.6: Deuteron matter radius r_m (in fm) to lowest and first order in perturbation theory, for three different integration limits for the perturbation integral.

(due to the fact that the leading-order deuteron is not quite bound enough). If our leading-order values had been smaller, the correction would bring the values towards to Nijmegen data, instead of away from it.

It should finally be mentioned that we also examined the normalisations of the particular wave functions (in Fig.5.2). As can be guessed at from the plots, the normalisations (with no cutoff applied to the integral) were quite large. The 'worst' one was for the red curves, which was ~ 2. However, by cutting off the region below 0.8 fm, the value reduced to 0.03, implying that the large normalisations originate from the unphysical growth of the wave functions at small r. However, the observables we calculated (see Tables 5.5 and 5.6) are much less sensitive to this region (due to the r^2 factors in the integrals).

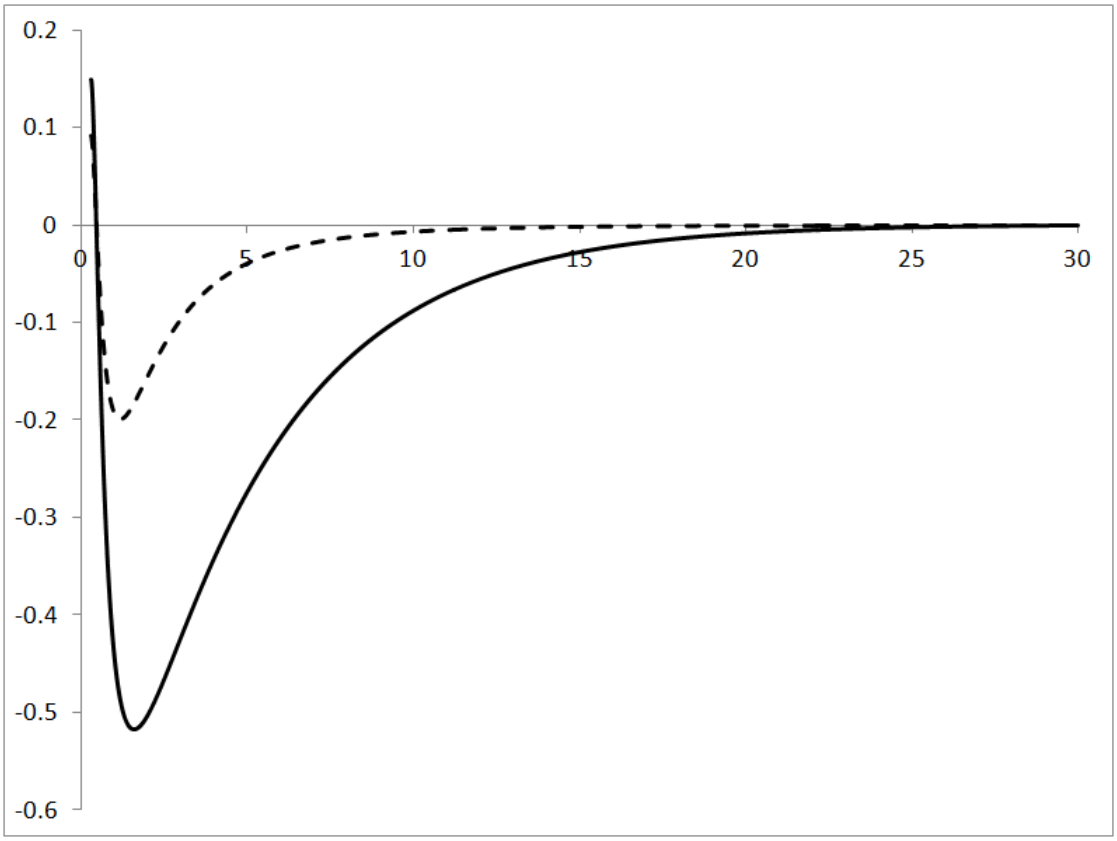

Figure 5.1: Leading-order deuteron wave functions $u_B^{(0)}$ (solid) and $w_B^{(0)}$ (dashed) (in $\mathrm{fm}^{-1/2}$), as a function of distance r (in fm), due to iterated OPE and fixing the short distance phase parameter.

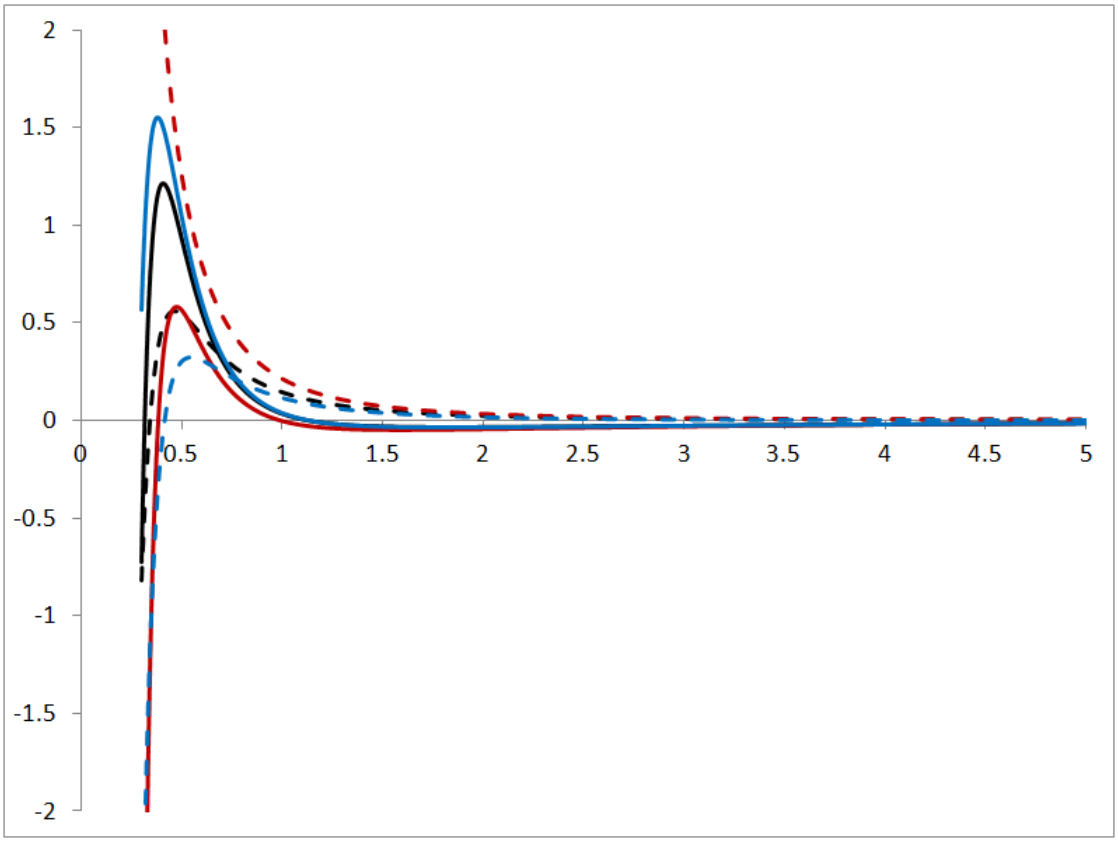

Figure 5.2: First-order deuteron wave functions $\tilde{u}_B^{(1)}$ (solid) and $\tilde{w}_B^{(1)}$ (dashed) (in $\text{fm}^{-1/2}$), as a function of distance r (in fm). The black curves correspond to a delta-shell potential (defined in Eq. (4.73)) with $\tilde{V}_{AA}^{(4)} = 42.8444$ fm^0 only, red curves with aforementioned $\tilde{V}_{AA}^{(4)}$ and $\tilde{V}_{AR}^{(4)} = \tilde{V}_{RA}^{(4)} = 0.005$ fm^0, and the blue curves correspond to all four elements present, with the additional $\tilde{V}_{RR}^{(4)} = 0.00354$ fm^0.

Chapter 6

Conclusions

Following the suggestion of Weinberg in the 1990's that nuclear forces could be derived in a consistent, model-independent way, using the tools of effective field theory, much effort has gone into realising this goal. However, even today various aspects of the theory are disagreed upon, namely the power counting of the short-range interactions and which parts of the long-range interaction should be treated nonperturbatively.

In this thesis we respect the power counting determined by the renormalisation group. We only iterate terms that are relevant, treating the rest as perturbations. This allows us to decrease our radial cutoff beyond the range of the effective field theory, minimising the artefacts of the cutoff, leaving effective interaction strengths that are governed by the strength of the missing physics (and not by the artificial cutoff).

We use a distorted-wave approach to "deconstruct" phase shifts, to obtain effective interactions after the removal of known long-range forces. The benefit of this method is that one can actually view the energy-dependence of short-range potential, and see in which region it may be appropriate to fit a polynomial. It also enables us to see clearly where the Nijmegen analyses are in agreement, and where the results may or may not be reliable.

In chapter 3 we "deconstructed" the $^1P_1$ phase shift. The single divergence that appeared in this channel was renormalised by the counterterm that is available in Weinberg power counting. The resulting rather low expansion scale we obtained from the resulting interaction strength, suggests that other long-range physics is present, such as the Δ-resonance.

We then turned to the coupled spin-triplet waves, with particular focus on

the ${}^3S_1$-${}^3D_1$ waves, which contain the deuteron. We were able to extract a breakdown scale of around 440 MeV, suggesting that all long-range physics has been accounted for, and that the theory is converging. We also found that only two counterterms (not three as predicted by Birse in [65]) were needed to obtain finite results, in agreement with Valderrama [84].

For the ${}^3P_2$-${}^3F_2$ waves, we found that only one element of the potential is well determined. This is due to the fact that only the P-wave is able to probe the nonperturbative region dominated by the $1/r^3$ tensor potential, whereas the F-wave could not, at least at the energies considered here. We extracted estimates for the scales of the underlying physics in the range 860 - 890 MeV, implying that the theory has good convergence,

To obtain results for deuteron at leading-order, we treated both OPE and one energy-independent short-distance phase parameter (nonperturbatively) to all orders. This was done by solving the (coupled) Schrodinger equation with OPE and fixing the value of the phase parameter to the ${}^3S_1$ scattering length. The leading-order results we obtained are in remarkably good agreement with the data.

With the aim to improve the results even further, we treated recoil OPE (order-Q^2), TPE (order-$Q^{2,3}$) and the effective interaction matrix (needed to renormalise the TPE matrix elements) to first order in perturbation theory. However, due to the accidentally good agreement at leading-order (especially with regards to the deuteron observables η and r_m) the perturbation we applied tended to move the results away from the data slightly. We tried fitting our less well determined short-distance interaction matrix elements to the deuteron binding energy, however, this did not seem to make much difference to the values of the observables we obtained, or even if it did make an impact on one observable, it did not improve other observables simultaneously.

Future directions of the work we suggest are first to improve the Dalgarno-Lewis method we used for calculating the correction to the wave function. More specifically, this would probably involve finding a method to resum the secular perturbation, which hopefully might correct the tails of the wave functions. Once that is accomplished, one can then look to going to higher orders in the chiral expansion. Other scope for future work could be to apply it to three-body systems, such as triton and helium-3.

Bibliography

[1] J. Chadwick, Proc. R. Soc. A **136**, 692 (1932).

[2] K. S. Krane, *Introductory Nuclear Physics*, John Wiley and Sons, Inc., 1988.

[3] H. Yukawa, Proc. Phys. Math. Soc. (Japan) **17**, 48 (1935).

[4] S. Taketani, M. Machida and S. O-numa, Prog. Theor. Phys. **7**, 45 (1952).

[5] K. A. Brueckner and K. M. Watson, Phys. Rev. **90**, 699 (1953).

[6] K. A. Brueckner and K. M. Watson, Phys. Rev. **92**, 1023 (1953).

[7] K. Holinde and R. Machleidt, Nucl. Phys. A **256**, 479 (1976).

[8] A. D. Jackson, D. O. Riska, and B. Verwest, Nucl. Phys. A **249**, 397 (1975).

[9] G. E. Brown and A. D. Jackson, *The Nucleon-Nucleon Interaction*, North-Holland, 1976.

[10] R. V. Mau, *in Mesons in Nuclei, Vol I, edited by M. Rho and D. H. Wilkinson*, North-Holland, 1979.

[11] M. Lacombe et al., Phys. Rev. C **21**, 861 (1980).

[12] R. Machleidt, K. Holinde, and C. Elster, Phys. Rep. **149**, 1 (1987).

[13] R. Machleidt, arXiv:nucl-th/9809069 .

[14] V. G. J. Stoks, R. A. M. Klomp, C. P. F. Terheggen, and J. J. de Swart, Phys. Rev. C **49**, 2950 (1994).

[15] R. Machleidt, Phys. Rev. C **63**, 024001 (2001).

[16] R. B. Wiringa, V. G. J. Stoks, and R. Schiavilla, Phys. Rev. C **51**, 38 (1995).

[17] V. G. J. Stoks, R. A. M. Klomp, M. C. M. Rentmeester, and J. J. de Swart, Phys. Rev. C **48**, 792 (1993).

[18] H. A. Bethe, Phys. Rev. **76**, 38 (1949).

[19] J. M. Blatt and J. D. Jackson, Phys. Rev. **76**, 18 (1949).

[20] S. Weinberg, Physica A **96**, 327 (1979).

[21] J. Gasser and H. Leutwyler, Annals Phys. **158**, 142 (1984).

[22] J. Gasser and H. Leutwyler, Nucl. Phys. B **250**, 465 (1985).

[23] S. Scherer and M. R. Schindler, *A Primer for Chiral Perturbation Theory*, Springer Berlin Heidelberg, 2012.

[24] J. Goldstone, Nuovo Cim. **19**, 154 (1961).

[25] J. Goldstone, A. Salam, and S. Weinberg, Phys. Rev. **127**, 965 (1962).

[26] P. F. Bedaque and U. van Kolck, Ann. Rev. Nucl. Part. Sci. **52**, 339 (2002).

[27] S. R. Beane, P. F. Bedaque, W. C. Haxton, D. R. Phillips, and M. J. Savage, arXiv:nucl-th/0008064 .

[28] E. Epelbaum, H.-W. Hammer, and U.-G. Meißner, Rev. Mod. Phys. **81**, 1773 (2009).

[29] S. Weinberg, Phys. Lett. B **251**, 288 (1990).

[30] S. Weinberg, Nucl. Phys. B **363**, 3 (1991).

[31] C. Ordonez and U. van Kolck, Phys. Lett. B **291**, 459 (1992).

[32] C. Ordonez, L. Ray, and U. van Kolck, Phys. Rev. Lett. **72**, 1982 (1994).

[33] C. Ordonez, L. Ray, and U. van Kolck, Phys. Rev. C **53**, 2086 (1996).

[34] E. Epelbaum, W. Glöckle, and U.-G. Meißner, Nucl. Phys. A **637**, 107 (1998).

[35] E. Epelbaum, W. Glöckle, and U.-G. Meißner, Nucl. Phys. A **671**, 295 (2000).

[36] J. L. Friar and S. A. Coon, Phys. Rev. C **49**, 1272 (1994).

[37] N. Kaiser, R. Brockmann, and W. Weise, Nucl. Phys. A **625**, 758 (1997).

[38] N. Kaiser, S. Gerstendorfer, and W. Weise, Nucl. Phys. A **637**, 395 (1998).

[39] N. Kaiser, Phys. Rev. C **64**, 057001 (2001).

[40] N. Kaiser, Phys. Rev. C **65**, 017001 (2001).

[41] D. R. Entem and R. Machleidt, Phys. Rev. C **68**, 041001 (2003).

[42] E. Epelbaum, W. Glöckle, and U.-G. Meißner, Nucl. Phys. A **747**, 362 (2005).

[43] E. Epelbaum, H. Krebs, and U.-G. Meißner, Eur. Phys. J. A **51**, 53 (2015).

[44] E. Epelbaum, H. Krebs, and U.-G. Meißner, Phys. Rev. Lett. **115**, 122301 (2015).

[45] D. R. Entem, N. Kaiser, R. Machleidt, and Y. Nosyk, Phys. Rev. C **91**, 014002 (2015).

[46] D. R. Entem, N. Kaiser, R. Machleidt, and Y. Nosyk, Phys. Rev. C **92**, 064001 (2015).

[47] R. Machleidt and D. R. Entem, Physics Reports **503**, 1 (2011).

[48] M. C. Birse, In Proc. of the 6th Int. Workshop on Chiral Dynamics, Bern, July 2009 (2009).

[49] E. Epelbaum and J. Gegelia, Eur. Phys. J. **A41**, 341 (2009).

[50] D. R. Phillips, PoS **CD12**, 013 (2013).

[51] U. van Kolck, Nucl. Phys. A **645**, 273 (1999).

[52] J. Gegelia, Physics Letters B **429**, 227 (1998).

[53] J. Gegelia, Journal of Physics G: Nuclear and Particle Physics **25**, 1681 (1999).

[54] D. B. Kaplan, M. J. Savage, and M. B. Wise, Phys. Lett. B **424**, 390 (1998).

[55] D. B. Kaplan, M. J. Savage, and M. B. Wise, Nucl. Phys. B **534**, 329 (1998).

[56] P. F. Bedaque, H.-W. Hammer, and U. van Kolck, Phys. Rev. Lett. **82**, 463 (1999).

[57] P. Bedaque, H.-W. Hammer, and U. van Kolck, Nuclear Physics A **676**, 357 (2000).

[58] E. Braaten and H. W. Hammer, Physics Reports **428**, 259 (2006).

[59] E. Braaten and H. W. Hammer, Annals of Physics **322**, 120 (2007).

[60] S. Fleming, T. Mehen, and I. W. Stewart, Phys. Rev. C **61**, 044005 (2000).

[61] S. Fleming, T. Mehen, and I. W. Stewart, Nucl. Phys. A **677**, 313 (2000).

[62] T. D. Cohen and J. M. Hansen, Phys. Rev. C **59**, 13 (1999).

[63] T. D. Cohen and J. M. Hansen, Phys. Rev. C **59**, 3047 (1999).

[64] S. R. Beane, D. B. Kaplan, and A. Vuorinen, Phys. Rev. C **80**, 011001 (2009).

[65] M. C. Birse, Phys. Rev. C **74**, 014003 (2006).

[66] G. P. Lepage, How to renormalize the Schrodinger equation, in *Nuclear physics. Proceedings, 8th Jorge Andre Swieca Summer School, Sao Jose dos Campos, Campos do Jordao, Brazil, January 26-February 7, 1997*, pages 135–180, 1997.

[67] E. Epelbaum and U.-G. Meißner, nucl-th/0609037 (2006).

[68] A. Nogga, R. G. E. Timmermans, and U. van Kolck, Phys. Rev. C **72**, 054006 (2005).

[69] K. G. Wilson and J. Kogut, Physics Reports **12**, 75 (1974).

[70] K. G. Richardson, M. C. Birse, and J. A. McGovern, hep-ph/9708435 (1997).

[71] M. C. Birse, J. A. McGovern, and K. G. Richardson, hep-ph/9808398 (1998).

[72] M. C. Birse, J. A. McGovern, and K. G. Richardson, Phys. Lett. B **464**, 169 (1999).

[73] K. G. Richardson, Ph. D. thesis, University of Manchester (2000).

[74] T. Barford and M. C. Birse, Phys. Rev. C **67**, 064006 (2003).

[75] T. Barford, Ph. D. thesis, University of Manchester (2004).

[76] T. Barford and M. C. Birse, J. Phys. A: Math. Gen. **38**, 697 (2005).

[77] M. C. Birse, hep-ph/0709.2865 (2007).

[78] M. C. Birse, Phil. Trans. Roy. Soc. A **369**, 2662 (2011).

[79] B. Gao, Phys. Rev. A **59**, 2778 (1999).

[80] M. C. Birse and J. A. McGovern, Phys. Rev. C **70**, 054002 (2004).

[81] M. C. Birse, Phys. Rev. C **76**, 034002 (2007).

[82] M. Birse, Eur. Phy. J. A **46**, 231 (2010).

[83] K. L. Ipson, K. Helmke, and M. C. Birse, Phys. Rev. C **83**, 017001 (2011).

[84] M. Pavón Valderrama, Phys. Rev. C **83**, 024003 (2011).

[85] M. Pavón Valderrama, Phys. Rev. C **84**, 064002 (2011).

[86] B. Long and C.-J. Yang, Phys. Rev. C **84**, 057001 (2011).

[87] B. Long and C.-J. Yang, Phys. Rev. C **85**, 034002 (2012).

[88] G. B. Arfken and H. J. Weber, *Mathematical Methods for Physicists*, Elsevier Academic Press, 2005.

[89] M. C. M. Rentmeester, R. G. E. Timmermans, J. L. Friar, and J. J. de Swart, Phys. Rev. Lett. **82**, 4992 (1999).

[90] M. C. M. Rentmeester, R. G. E. Timmermans, and J. J. de Swart, Phys. Rev. C **67**, 044001 (2003).

[91] J. L. Friar, Phys. Rev. C **60**, 034002 (1999).

[92] NN-Online, Radboud University Nijmegen, http://nn-online.org/.

[93] H. Krebs, E. Epelbaum, and U.-G. Meißner, Eur. Phys. J. A **32**, 127 (2007).

[94] W. Rarita and J. Schwinger, Phys. Rev. **59**, 436 (1941).

[95] W. Rarita and J. Schwinger, Phys. Rev. **59**, 556 (1941).

[96] M. Pavón Valderrama and E. Ruiz Arriola, Phys. Rev. C **72**, 054002 (2005).

[97] D. W. L. Sprung et al., Phys. Rev. C **49**, 2942 (1994).

[98] J. M. Blatt and L. C. Biedenharn, Phys. Rev. **86**, 399 (1952).

[99] H. P. Stapp, T. J. Ypsilantis, and N. Metropolis, Phys. Rev. **105**, 302 (1957).

[100] L. S. Rodberg and R. M. Thaler, *Introduction to the Quantum Theory of Scattering*, Academic Press, 1967.

[101] J. de Swart, C. Terheggen, and V. Stoks, (1995).

[102] M. P. Valderrama and E. R. Arriola, Phys. Rev. C **72**, 044007 (2005).

[103] W. H. Press, S. A. Teukolsky, W. T. Vetterling, and B. P. Flannery, *Numerical Recipes in C*, Cambridge University Press, 1992.

[104] J. M. B. Kellogg, I. I. Rabi, N. F. Ramsey, and J. R. Zacharias, Phys. Rev. **55**, 318 (1939).

[105] J. M. B. Kellogg, I. I. Rabi, N. F. Ramsey, and J. R. Zacharias, Phys. Rev. **57**, 677 (1940).

[106] D. R. Phillips and T. D. Cohen, Nuclear Physics A **668**, 45 (2000).

[107] A. Dalgarno and J. T. Lewis, Proc. Roy. Soc. A **233**, 70 (1955).

[108] L. I. Schiff, *Quantum Mechanics*, McGraw-Hill, 1968.

[109] A. P. French, *Vibrations and Waves*, CRC Press, 1971.

Appendix A

Superposition of Two Simple Harmonic Motions: a Geometrical Method

To determine the coefficients C and D that are used to form linear combinations of two independent pairs of solutions that build the u eigen wave in Eq. (4.27) and w eigen wave in Eq. (4.28), we can apply a geometrical method described by French [109]. French uses this method to superimpose two simple harmonic motions (SHMs), whose angular frequencies are the same, and determine the resulting amplitude and phase. The starting point is to write the two SHMs in the usual way as

$$\begin{aligned} x_1 &= A_1 \cos(\omega t + \alpha_1) \\ x_2 &= A_2 \cos(\omega t + \alpha_2). \end{aligned} \tag{A.1}$$

Combining the two, the resulting motion can be written as

$$x = x_1 + x_2 = A_1 \cos(\omega t + \alpha_1) + A_2 \cos(\omega t + \alpha_2) = A \cos(\omega t + \alpha). \tag{A.2}$$

These equations can be represented pictorially (see part (a) of Fig. A.1) in terms of rotating vectors, and can used to form a vector triangle (see part (b) of Fig. A.1). Applying the cosine rule to this triangle one can obtain the amplitude of the resulting motion, A, given by

$$A^2 = A_1^2 + A_2^2 + 2A_1 A_2 \cos(\alpha_2 - \alpha_1). \tag{A.3}$$

To determine the resulting phase, α, we notice that $A\sin\beta = A_2\sin\theta$, which in terms of the original phases, α_1, α_2 and α gives

$$A\sin(\alpha - \alpha_1) = A_2\sin(\alpha_2 - \alpha_1). \tag{A.4}$$

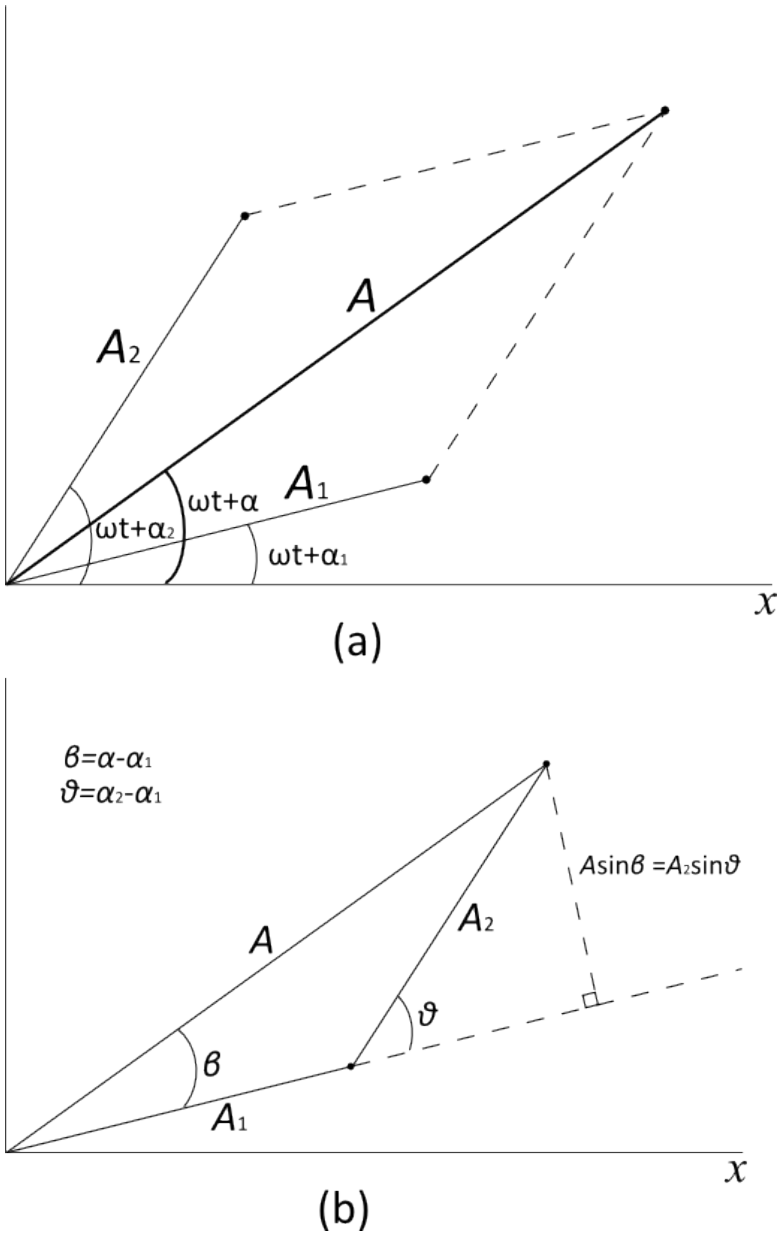

Figure A.1: (a) Superposition of two rotating vectors with the same angular frequency, ω. (b) Vector triangle used to construct resultant rotating vector [109].

Appendix B

Residual Scattering Matrix, $\tilde{S}$

In the 'eigen-basis' [98] the scattering matrix due to OPE alone is given by

$$S_l = {U_l}^{-1} e^{2i\Delta_l} U_l, \tag{B.1}$$

where

$$e^{2i\Delta_l} = \begin{pmatrix} e^{2i\delta_{\alpha,l}} & 0 \\ 0 & e^{2i\delta_{\beta,l}} \end{pmatrix} \tag{B.2}$$

and

$$U_l = \begin{pmatrix} \cos\epsilon_l & \sin\epsilon_l \\ -\sin\epsilon_l & \cos\epsilon_l \end{pmatrix}. \tag{B.3}$$

The total scattering matrix, S, can be written in a similar form

$$S = U^{-1} e^{2i\Delta} U = {U_l}^{-1} e^{i\Delta_l} \tilde{S} e^{i\Delta_l} U_l. \tag{B.4}$$

with quantities U and $e^{2i\Delta}$ defined in the same way as U_l and $e^{2i\Delta_l}$, respectively (without the subscripts of course).

Rearranging Eq. (B.4) for the residual scattering matrix, $\tilde{S}$, gives

$$\tilde{S} = e^{-i\Delta_l} U_l U^{-1} e^{2i\Delta} U {U_l}^{-1} e^{-i\Delta_l}, \tag{B.5}$$

which can be written out in full to give

$$\tilde{S} = \tag{B.6}$$

$$\begin{pmatrix} \cos^2\Delta\epsilon e^{2i\Delta_{\alpha\alpha}} + \sin^2\Delta\epsilon e^{2i\Delta_{\beta\alpha}} & \cos\Delta\epsilon\sin\Delta\epsilon(e^{2i\Delta_{\alpha\alpha}}e^{2i\Delta_{\alpha\beta}} - e^{2i\Delta_{\beta\alpha}}e^{2i\Delta_{\beta\beta}}) \\ \cos\Delta\epsilon\sin\Delta\epsilon(e^{2i\Delta_{\alpha\alpha}}e^{2i\Delta_{\alpha\beta}} - e^{2i\Delta_{\beta\alpha}}e^{2i\Delta_{\beta\beta}}) & \sin^2\Delta\epsilon e^{2i\Delta_{\alpha\beta}} + \cos^2\Delta\epsilon e^{2i\Delta_{\beta\beta}} \end{pmatrix}$$

where $\Delta\epsilon = \epsilon - \epsilon_l$, $\Delta_{\alpha\alpha} = \delta_\alpha - \delta_{\alpha,l}$, $\Delta_{\alpha\beta} = \delta_\alpha - \delta_{\beta,l}$ and so on.

The residual scattering matrix $\tilde{S}$ in Eq. (B.6) can be related to the Wronskian in the LHS of Eq. (4.61) evaluated at $r \to \infty$. To do this the wave functions $\mathbf{u}_l$ and $\mathbf{u}$ are normalised to have the following forms,

$\mathbf{u}_l \xrightarrow{r\to\infty}$

$$\frac{1}{p}\begin{pmatrix} e^{i\delta_{\alpha,l}}\cos\epsilon_l\sin(pr+\delta_{\alpha,l}) & -e^{i\delta_{\beta,l}}\sin\epsilon_l\sin(pr+\delta_{\beta,l}) \\ e^{i\delta_{\alpha,l}}\sin\epsilon_l\sin(pr-\pi+\delta_{\alpha,l}) & e^{i\delta_{\beta,l}}\cos\epsilon_l\sin(pr-\pi+\delta_{\beta,l}) \end{pmatrix} \tag{B.7}$$

and

$\mathbf{u} \xrightarrow{r\to\infty}$

$$\frac{1}{p}\begin{pmatrix} e^{i\delta_\alpha}\cos\epsilon\sin(pr+\delta_\alpha) & -e^{i\delta_\beta}\sin\epsilon\sin(pr+\delta_\beta) \\ e^{i\delta_\alpha}\sin\epsilon\sin(pr-\pi+\delta_\alpha) & e^{i\delta_\beta}\cos\epsilon\sin(pr-\pi+\delta_\beta) \end{pmatrix}. \tag{B.8}$$

Now, as Eqs. (B.7) and (B.8) have similar forms as those in the uncoupled spin-singlet waves in Eqs. (4.41) and (4.42), which on evaluating the Wronksian in the limit $r \to \infty$ resulted in a residual T-matrix structure, we expect a similar result on evaluating the Wronskian here.

We know that in the uncoupled channels the T-matrix and S-matrix are defined as $T_L = e^{i\delta_L}\sin\delta_L$ and $S_L = e^{2i\delta_L}$, respectively. Therefore, by rewriting the T-matrix in an equivalent form given by $T_l = \frac{1}{2i}\left(e^{2i\delta_L} - 1\right)$ we know S_L and T_L are related via $T_L = \frac{1}{2i}(S_L - 1)$. It is with this equation that we want to connect $\tilde{S}$ to our Wronskian at $r \to \infty$.

So, inserting Eqs. (B.7) and (B.8) into Eq. (4.61) gives:

$$\int_0^\infty \mathbf{u}_l^\dagger \mathbf{V}^s \mathbf{u}\, \mathrm{d}r =$$

$$-\frac{1}{Mp}\begin{pmatrix} e^{i\Delta_{\alpha\alpha}}\cos(\Delta\epsilon)\sin(\Delta_{\alpha\alpha}) & -e^{i\Delta_{\beta\alpha}}\sin(\Delta\epsilon)\sin(\Delta_{\beta\alpha}) \\ e^{i\Delta_{\alpha\beta}}\sin(\Delta\epsilon)\sin(\Delta_{\alpha\beta}) & e^{i\Delta_{\beta\beta}}\cos(\Delta\epsilon)\sin(\Delta_{\beta\beta}) \end{pmatrix}, \tag{B.9}$$

and defining $\tilde{W}$ as:

$$\tilde{W} = \begin{pmatrix} e^{i\Delta_{\alpha\alpha}}\cos(\Delta\epsilon)\sin(\Delta_{\alpha\alpha}) & -e^{i\Delta_{\beta\alpha}}\sin(\Delta\epsilon)\sin(\Delta_{\beta\alpha}) \\ e^{i\Delta_{\alpha\beta}}\sin(\Delta\epsilon)\sin(\Delta_{\alpha\beta}) & e^{i\Delta_{\beta\beta}}\cos(\Delta\epsilon)\sin(\Delta_{\beta\beta}) \end{pmatrix}, \tag{B.10}$$

we can relate it to the residual S-matrix via the following transformations:

$$\frac{\tilde{S}-1}{2i} = e^{i\Delta_l}\left(-Mp\tilde{W}\right)UU_l^{-1}e^{-i\Delta_l}. \tag{B.11}$$

Appendix C

Coefficients for the $^3S_1 - {}^3D_1$ Short-Distance Wave Functions

In this appendix we present the coefficients for the power series representation of the $^3S_1 - {}^3D_1$ wave functions at short-distances. The terms up to and including order-$x^{7/2}$ ($x = r/R$) were first derived by Valderrama and Arriola [96]. We include extra terms up to order-$x^{11/2}$ for convergence reasons.

$$
\begin{aligned}
f_{1A} = 1 &- \frac{35i}{32}x^{\frac{1}{2}} - \frac{1811}{6144}x + \frac{2441i}{65536}x^{\frac{3}{2}} - \frac{34805}{8388608}x^2 \\
&+ \left(\frac{-333725i}{268435456} - \frac{i}{15}m^3R^3 + \frac{i}{10}p^2R^2 \right) x^{\frac{5}{2}} \\
&+ \left(\frac{9873675}{17179869184} + \frac{m^2R^2}{36} - \frac{m^3R^3}{32} + \frac{3p^2R^2}{64} \right) x^3 \\
&+ \left(\frac{193405905i}{549755813888} + \frac{353i}{24192}m^2R^2 - \frac{709i}{92160}m^3R^3 \right. \\
&\left. + \frac{i}{28}m^4R^4 + \frac{709i}{61440}p^2R^2 \right) x^{\frac{7}{2}} \\
&+ \left(\frac{-37373341005}{140737488355328} - \frac{6073m^2R^2}{663552} - \frac{16463p^2R^2}{1966080} \right. \\
&\left. + \frac{16463m^3R^3}{2949120} + \frac{m^4R^4}{128} \right) x^4 \\
&+ \left(\frac{-10681955553425i}{4503599627370496} - \frac{1851985i}{1337720832}m^2R^2 - \frac{462011i}{452984832}p^2R^2 \right. \\
&\left. + \frac{462011i}{679477248}m^3R^3 - \frac{i}{516096}m^4R^4 - \frac{i}{90}m^5R^5 \right) x^{\frac{9}{2}} \\
&+ \left(\frac{70323174947025}{288230376151711744} - \frac{967587491m^2R^2}{171228266496} - \frac{81029761p^2R^2}{14495514624} \right. \\
&\left. + \frac{81029761m^3R^3}{21743271936} - \frac{110959m^4R^4}{49545216} - \frac{p^4R^4}{200} + \frac{m^5R^5}{2880} + \frac{m^3p^2R^5}{150} - \frac{m^6R^6}{450} \right) x^5 \\
&+ \left(\frac{2615165793615375i}{9223372036854775808} - \frac{1315262054875i}{180817049419776}m^2R^2 \right. \\
&- \frac{208172142595i}{30614526885888}p^2R^2 + \frac{208172142595i}{45921790328832}m^3R^3 + \frac{390217139i}{69759664128}m^4R^4 \\
&+ \frac{i}{360}m^2p^2R^4 - \frac{51i}{14080}p^4R^4 + \frac{5417i}{6082560}m^5R^5 + \frac{17i}{3520}m^3p^2R^5 \\
&\left. + \frac{29i}{31680}m^6R^6 \right) x^{\frac{11}{2}} + \mathcal{O}(x^6)
\end{aligned}
\tag{C.1}
$$

$$
f_{2A}(x) = f_{1A}^*(x) \tag{C.2}
$$

$$
\begin{aligned}
f_{2R} = 1 &+ \frac{67}{32\sqrt{2}}x^{\frac{1}{2}} + \frac{7763}{12288}x + \left(\frac{8873}{131072\sqrt{2}} - \frac{m^2R^2}{3\sqrt{2}}\right)x^{\frac{3}{2}} \\
&+ \left(\frac{-105845}{33554432} - \frac{55m^2R^2}{192}\right)x^2 \\
&+ \left(\frac{881405}{1073741824\sqrt{2}} - \frac{10807m^2R^2}{184320\sqrt{2}} + \frac{m^3R^3}{15\sqrt{2}} - \frac{p^2R^2}{10\sqrt{2}}\right)x^{\frac{5}{2}} \\
&+ \left(\frac{-23360715}{137438953472} - \frac{332899m^2R^2}{11796480} + \frac{47m^3R^3}{960} + \frac{m^4R^4}{36} - \frac{47p^2R^2}{640}\right)x^3 \\
&+ \left(\frac{419268465}{4398046511104\sqrt{2}} + \frac{30559591m^2R^2}{31708938240\sqrt{2}} + \frac{2141m^3R^3}{1290240\sqrt{2}}\right. \\
&\left. + \frac{229m^4R^4}{8064} - \frac{2141p^2R^2}{860160\sqrt{2}}\right)x^{\frac{7}{2}} \\
&+ \left(\frac{-75461951565}{2251799813685248} + \frac{35380837879m^2R^2}{6088116142080} + \frac{291127p^2R^2}{55050240}\right. \\
&\left. - \frac{291127m^3R^3}{82575360} - \frac{113927m^4R^4}{15482880} - \frac{m^5R^5}{90} + \frac{m^2p^2R^4}{60}\right)x^4 \\
&+ \left(\frac{2033578371825}{72057594037927936\sqrt{2}} - \frac{1883643668951m^2R^2}{100192997081088\sqrt{2}} - \frac{32085701p^2R^2}{1811939328\sqrt{2}}\right. \\
&\left. + \frac{32085701m^3R^3}{2717908992\sqrt{2}} + \frac{258379m^4R^4}{14155776\sqrt{2}} + \frac{13m^2p^2R^4}{1152\sqrt{2}} - \frac{97m^5R^5}{8640\sqrt{2}} - \frac{m^6R^6}{324\sqrt{2}}\right)x^{\frac{9}{2}} \\
&+ \left(\frac{-127405625972625}{9223372036854775808} + \frac{927914845251175m^2R^2}{44886462692327424}\right. \\
&+ \frac{16142747431p^2R^2}{811748818944} - \frac{16142747431m^3R^3}{1217623228416} + \frac{956945261m^4R^4}{1902536294400} \\
&\left. - \frac{13439m^2p^2R^4}{2867200} + \frac{p^4R^4}{400} + \frac{51511m^5R^5}{38707200} - \frac{m^3p^2R^5}{300} + \frac{4007m^6R^6}{3628800}\right)x^5 \\
&+ \left(\frac{4541619672564975}{2951479051793528256856\sqrt{2}} - \frac{13958580510534559007m^2R^2}{3792008368247820779 52\sqrt{2}}\right. \\
&- \frac{61868818299221p^2R^2}{1714413505609728\sqrt{2}} + \frac{61868818299221m^3R^3}{2571620258414592\sqrt{2}} \\
&- \frac{3909710495027m^4R^4}{287011189555200\sqrt{2}} + \frac{197051929m^2p^2R^4}{27249868800\sqrt{2}} + \frac{97p^4R^4}{140800\sqrt{2}} \\
&- \frac{188424569m^5R^5}{40874803200\sqrt{2}} - \frac{97m^3p^2R^5}{105600\sqrt{2}} + \frac{18639689m^6R^6}{7664025600\sqrt{2}} \\
&\left. - \frac{m^4p^2R^6}{360\sqrt{2}} + \frac{m^7R^7}{540\sqrt{2}}\right)x^{\frac{11}{2}} + \mathcal{O}(x^6)
\end{aligned}
\tag{C.3}
$$

$$
f_{1R}(x) = f_{2R}(e^{2\pi i}x) \tag{C.4}
$$

$$
\begin{aligned}
g_{1A} = 1 &- \frac{35i}{32}x^{\frac{1}{2}} - \frac{4883}{6144}x + \frac{82075i}{196608}x^{\frac{3}{2}} + \frac{1245195}{8388608}x^2 \\
&+ \left(\frac{-5136285i}{268435456} - \frac{i}{15}m^3R^3 + \frac{i}{10}p^2R^2 \right) x^{\frac{5}{2}} \\
&+ \left(\frac{42237195}{17179869184} - \frac{m^2R^2}{18} - \frac{m^3R^3}{32} + \frac{3p^2R^2}{64} \right) x^3 \\
&+ \left(\frac{494999505i}{549755813888} - \frac{65i}{12096}m^2R^2 + \frac{2363i}{92160}m^3R^3 \right. \\
&\left. + \frac{i}{28}m^4R^4 - \frac{2363i}{61440}p^2R^2 \right) x^{\frac{7}{2}} \\
&+ \left(\frac{-72613666125}{140737488355328} - \frac{1415m^2R^2}{331776} - \frac{1985p^2R^2}{131072} \right. \\
&\left. + \frac{1985m^3R^3}{196608} + \frac{m^4R^4}{128} \right) x^4 \\
&+ \left(\frac{-1755474145425i}{4503599627370496} - \frac{12135695i}{668860416}m^2R^2 - \frac{7558331i}{452984832}p^2R^2 \right. \\
&\left. + \frac{7558331i}{679477248}m^3R^3 - \frac{9217i}{516096}m^4R^4 - \frac{i}{90}m^5R^5 \right) x^{\frac{9}{2}} \\
&+ \left(\frac{103527725526225}{288230376151711744} + \frac{357002501m^2R^2}{12230590464} + \frac{407989631p^2R^2}{14495514624} \right. \\
&\left. - \frac{407989631m^3R^3}{21743271936} + \frac{47783m^4R^4}{7077888} - \frac{p^4R^4}{200} + \frac{m^5R^5}{2880} + \frac{m^3p^2R^5}{150} - \frac{m^6R^6}{450} \right) x^5 \\
&+ \left(\frac{3566523804418575i}{9223372036854775808} + \frac{3718928234 05i}{12915503529984}m^2R^2 \right. \\
&+ \frac{831191751677i}{30614526885888}p^2R^2 - \frac{831191751677i}{45921790328832}m^3R^3 - \frac{69989899i}{9965666304}m^4R^4 \\
&- \frac{i}{180}m^2p^2R^4 - \frac{51i}{14080}p^4R^4 + \frac{73001i}{6082560}m^5R^5 + \frac{17i}{3520}m^3p^2R^5 \\
&\left. + \frac{29i}{31680}m^6R^6 \right) x^{\frac{11}{2}} + \mathcal{O}(x^6)
\end{aligned}
\tag{C.5}
$$

$$
g_{2A}(x) = g_{1A}^*(x) \tag{C.6}
$$

$$
\begin{aligned}
g_{2R} = 1 &+ \frac{67}{32\sqrt{2}}x^{\frac{1}{2}} + \frac{13907}{12288}x + \left(\frac{307195}{393216\sqrt{2}} - \frac{m^2R^2}{3\sqrt{2}}\right)x^{\frac{3}{2}} \\
&+ \left(\frac{5075595}{33554432} - \frac{55m^2R^2}{192}\right)x^2 \\
&+ \left(\frac{19661565}{1073741824\sqrt{2}} - \frac{41527m^2R^2}{184320\sqrt{2}} + \frac{m^3R^3}{15\sqrt{2}} - \frac{p^2R^2}{10\sqrt{2}}\right)x^{\frac{5}{2}} \\
&+ \left(\frac{-143137995}{137438953472} - \frac{128033m^2R^2}{3932160} + \frac{47m^3R^3}{960} + \frac{m^4R^4}{36} - \frac{47p^2R^2}{640}\right)x^3 \\
&+ \left(\frac{1476620145}{4398046511104\sqrt{2}} - \frac{45736601m^2R^2}{31708938240\sqrt{2}} + \frac{45149m^3R^3}{1290240\sqrt{2}}\right. \\
&\left. + \frac{229m^4R^4}{8064} - \frac{45149p^2R^2}{860160\sqrt{2}}\right)x^{\frac{7}{2}} \\
&+ \left(\frac{-193175707725}{2251799813685248} - \frac{4787313973m^2R^2}{1217623228416} - \frac{54183p^2R^2}{3670016}\right. \\
&\left. + \frac{18061m^3R^3}{1835008} - \frac{101113m^4R^4}{15482880} - \frac{m^5R^5}{90} + \frac{m^2p^2R^4}{60}\right)x^4 \\
&+ \left(\frac{4234714909425}{72057594037927936\sqrt{2}} + \frac{6473431769887m^2R^2}{701350979567616\sqrt{2}} + \frac{96522397p^2R^2}{12683575296\sqrt{2}}\right. \\
&\left. - \frac{96522397m^3R^3}{19025362944\sqrt{2}} - \frac{454387m^4R^4}{99090432\sqrt{2}} + \frac{13m^2p^2R^4}{1152\sqrt{2}} - \frac{97m^5R^5}{8640\sqrt{2}} - \frac{m^6R^6}{324\sqrt{2}}\right)x^{\frac{9}{2}} \\
&+ \left(\frac{-229948053159825}{9223372036854775808} - \frac{56916172999007m^2R^2}{6412351813189632}\right. \\
&- \frac{994490399p^2R^2}{115964116992} + \frac{994490399m^3R^3}{173946175488} - \frac{6514588819m^4R^4}{1902536294400} \\
&\left. + \frac{31363m^2p^2R^4}{8601600} + \frac{p^4R^4}{400} - \frac{163529m^5R^5}{38707200} - \frac{m^3p^2R^5}{300} + \frac{4007m^6R^6}{3628800}\right)x^5 \\
&+ \left(\frac{7388318836673775}{2951479051793528256\sqrt{2}} + \frac{768207639422149591m^2R^2}{541715481178260111 36\sqrt{2}}\right. \\
&+ \frac{3443162966845p^2R^2}{244916215087104\sqrt{2}} - \frac{3443162966845m^3R^3}{367374322630656\sqrt{2}} \\
&+ \frac{19908518003611m^4R^4}{2009078326886400\sqrt{2}} - \frac{27664871m^2p^2R^4}{27249868800\sqrt{2}} + \frac{97p^4R^4}{140800\sqrt{2}} \\
&- \frac{39401849m^5R^5}{40874803200\sqrt{2}} - \frac{97m^3p^2R^5}{105600\sqrt{2}} + \frac{6812489m^6R^6}{7664025600\sqrt{2}} \\
&\left. - \frac{m^4p^2R^6}{360\sqrt{2}} + \frac{m^7R^7}{540\sqrt{2}}\right)x^{\frac{11}{2}} + \mathcal{O}(x^6)
\end{aligned}
\tag{C.7}
$$

$$
g_{1R}(x) = g_{2R}(e^{2\pi i}x) \tag{C.8}
$$

Appendix D

Coefficients for the ${}^3P_2 - {}^3F_2$ Short-Distance Wave Fuctions

Here we present the coefficients for the terms in the power series expansion of the ${}^3P_2 - {}^3F_2$ wave functions in the limit $r \to 0$. We include terms up to order-$x^{11/2}$, where $x = r/R$.

$$
\begin{aligned}
f_{1A} = 1 &- \frac{393i}{32\sqrt{6}}x^{\frac{1}{2}} - \frac{42195}{4096}x + \left(\frac{3544113i}{131072\sqrt{6}} - \frac{m^2R^2i}{3\sqrt{6}}\right)x^{\frac{3}{2}} \\
&+ \left(\frac{197067747}{33554432} - \frac{119m^2R^2}{112}\right)x^2 \\
&+ \left(-\frac{10552373931i}{5368709120\sqrt{6}} + \frac{50237m^2R^2i}{20480\sqrt{6}} + \frac{m^3R^3i}{15\sqrt{6}} + \frac{3p^2R^2i}{10\sqrt{6}}\right)x^{\frac{5}{2}} \\
&+ \left(\frac{34410615693}{687194767360} + \frac{3280931m^2R^2}{3932160} + \frac{37m^3R^3}{320} + \frac{333p^2R^2}{640} - \frac{m^4R^4}{108}\right)x^3 \\
&+ \left(-\frac{6146924518905i}{30786325577728\sqrt{6}} - \frac{258891735m^2R^2i}{234881024\sqrt{6}} - \frac{11603m^3R^3i}{28672\sqrt{6}}\right. \\
&\left. + \frac{677m^4R^4i}{8064\sqrt{6}} - \frac{104427p^2R^2i}{57344\sqrt{6}}\right)x^{\frac{7}{2}} \\
&+ \left(\frac{19106413543995721}{78812993478983680} - \frac{66403987523m^2R^2}{225485783040} - \frac{6242331p^2R^2}{18350080}\right. \\
&\left. - \frac{2080777m^3R^3}{27525120} + \frac{167123m^4R^4}{5160960} + \frac{m^2p^2R^4}{60} + \frac{m^5R^5}{270}\right)x^4 \\
&+ \left(\frac{10742151004316459461i}{7566047373982433280\sqrt{6}} - \frac{3283305136693m^2R^2i}{8658654068736\sqrt{6}}\right. \\
&+ \frac{1011229167p^2R^2i}{2348810240\sqrt{6}} + \frac{337076389m^3R^3i}{3523215360\sqrt{6}} - \frac{11309441m^4R^4i}{165150720\sqrt{6}} \\
&\left. - \frac{289m^5R^5i}{8640\sqrt{6}} - \frac{257m^2p^2R^4i}{1920\sqrt{6}} + \frac{m^6R^6i}{972\sqrt{6}}\right)x^{\frac{9}{2}} \\
&+ \left(\frac{-6446783768180133129529}{4842270319348757299200} + \frac{814785109319341m^2R^2}{1979120929996800}\right. \\
&- \frac{186330835983p^2R^2}{751619276800} - \frac{62110278661m^3R^3}{1127428915200} - \frac{13988412623m^4R^4}{211392921600} \\
&\left. - \frac{3p^4R^4}{400} - \frac{333577m^2p^2R^4}{8601600} - \frac{546377m^5R^5}{38707200} - \frac{m^3p^2R^5}{300} + \frac{7193m^6R^6}{10886400}\right)x^5 \\
&+ \left(\frac{-4070326908288034644854221i}{568159717470254189772800\sqrt{6}} + \frac{2842517437271004836 9m^2R^2i}{1300414392403230720 0\sqrt{6}}\right. \\
&- \frac{595854475542477p^2R^2i}{529139970867200\sqrt{6}} - \frac{66206052838053m^3R^3i}{264569985433600\sqrt{6}} - \frac{63147674559m^4R^4i}{8267812044800\sqrt{6}} \\
&+ \frac{6036021m^2p^2R^4i}{144179200\sqrt{6}} + \frac{7209p^4R^4i}{140800\sqrt{6}} + \frac{16240661m^5R^5i}{648806400\sqrt{6}} + \frac{801m^3p^2R^5i}{35200\sqrt{6}} \\
&\left. + \frac{1402597m^6R^6i}{364953600\sqrt{6}} - \frac{m^4p^2R^6i}{360\sqrt{6}} - \frac{m^7R^7i}{1620\sqrt{6}}\right)x^{\frac{11}{2}} + \mathcal{O}(x^6) \qquad \text{(D.1)}
\end{aligned}
$$

$$
f_{2A}(x) = f_{1A}^*(x) \qquad \text{(D.2)}
$$

$$
\begin{aligned}
f_{2R} = 1 &+ \frac{297}{32\sqrt{3}}x^{\frac{1}{2}} + \frac{24979}{2048}x + \frac{1680913}{65536\sqrt{3}}x^{\frac{3}{2}} + \frac{75513187}{8388608}x^2 \\
&+ \left(\frac{4195093259}{1342177280\sqrt{3}} - \frac{30p^2R^2}{10\sqrt{3}} - \frac{m^3R^3}{15\sqrt{3}} \right) x^{\frac{5}{2}} \\
&+ \left(\frac{-53635375079}{257698037760} - \frac{m^2R^2}{6} - \frac{79m^3R^3}{480} - \frac{237p^2R^2}{320} \right) x^3 \\
&+ \left(\frac{-1997317215933}{19241453486080\sqrt{3}} - \frac{895m^2R^2}{1344\sqrt{3}} - \frac{88093m^3R^3}{215040\sqrt{3}} \right. \\
&\left. + \frac{m^4R^4}{28\sqrt{3}} - \frac{264279p^2R^2}{143360\sqrt{3}} \right) x^{\frac{7}{2}} \\
&+ \left(\frac{3026368666736347}{14777436277309440} - \frac{113359m^2R^2}{258048} - \frac{2504251p^2R^2}{4587520} \right. \\
&\left. - \frac{2504251m^3R^3}{20643840} + \frac{71m^4R^4}{896} \right) x^4 \\
&+ \left(\frac{-179461406393491429}{472877960873902080\sqrt{3}} + \frac{624955m^2R^2}{8257536\sqrt{3}} - \frac{221765487p^2R^2}{587202560\sqrt{3}} \right. \\
&\left. - \frac{73921829m^3R^3}{880803840\sqrt{3}} + \frac{10027m^4R^4}{57344\sqrt{3}} - \frac{m^5R^5}{90\sqrt{3}} \right) x^{\frac{9}{2}} \\
&+ \left(\frac{-29525454179895513991}{151320947479648665600} - \frac{2704543m^2R^2}{1056964608} \right. \\
&+ \frac{8615800687p^2R^2}{93952409600} + \frac{8615800687m^3R^3}{422785843200} + \frac{1127471m^4R^4}{16515072} \\
&\left. + \frac{3p^4R^4}{200} - \frac{7m^5R^5}{320} + \frac{m^3p^2R^5}{150} + \frac{m^6R^6}{1350} \right) x^5 \\
&+ \left(\frac{158092305947676903954553}{532649735128363302912003\sqrt{3}} - \frac{138899189861m^2R^2}{206695301120\sqrt{3}} \right. \\
&+ \frac{13968012227443p^2R^2}{66142496358400\sqrt{3}} + \frac{13968012227443m^3R^3}{297641233612800\sqrt{3}} \\
&+ \frac{41374803m^4R^4}{234881024\sqrt{3}} + \frac{m^2p^2R^4}{20\sqrt{3}} + \frac{4041p^4R^4}{70400\sqrt{3}} \\
&\left. - \frac{6299m^5R^5}{184320\sqrt{3}} + \frac{449m^3p^2R^5}{17600\sqrt{3}} - \frac{751m^6R^6}{158400\sqrt{3}} \right) x^{\frac{11}{2}} + \mathcal{O}(x^6)
\end{aligned}
\tag{D.3}
$$

$$
f_{1R}(x) = f_{2R}(e^{2\pi i}x) \tag{D.4}
$$

$$
\begin{aligned}
g_{1A} = 1 &- \frac{393i}{32\sqrt{6}}x^{\frac{1}{2}} - \frac{52435}{4096}x + \left(\frac{6913073i}{131072\sqrt{6}} - \frac{m^2R^2i}{3\sqrt{6}}\right)x^{\frac{3}{2}} \\
&+ \left(\frac{854127587}{33554432} - \frac{119m^2R^2}{192}\right)x^2 \\
&+ \left(\frac{-269903004331i}{5368709120\sqrt{6}} + \frac{201911m^2R^2i}{61440\sqrt{6}} + \frac{m^3R^3i}{15\sqrt{6}} + \frac{3p^2R^2i}{10\sqrt{6}}\right)x^{\frac{5}{2}} \\
&+ \left(\frac{-19713578700121}{2061584302080} + \frac{19929193m^2R^2}{11796480} + \frac{37m^3R^3}{320} + \frac{333p^2R^2}{640} - \frac{m^4R^4}{108}\right)x^3 \\
&+ \left(\frac{1123819194147 91i}{30786325577728\sqrt{6}} - \frac{2171023237m^2R^2i}{704643072\sqrt{6}} - \frac{49145m^3R^3i}{86016\sqrt{6}}\right. \\
&\left. + \frac{677m^4R^4i}{8064\sqrt{6}} - \frac{147435p^2R^2i}{57344\sqrt{6}}\right)x^{\frac{7}{2}} \\
&+ \left(\frac{-75481274692695077}{236438980436951040} - \frac{292615160009m^2R^2}{676457349120} - \frac{25524251p^2R^2}{18350080}\right. \\
&\left. - \frac{25524251m^3R^3}{82575360} + \frac{859769m^4R^4}{15482880} + \frac{m^2p^2R^4}{60} + \frac{m^5R^5}{270}\right)x^4 \\
&+ \left(\frac{-62787384339305754 19i}{7566047373982433280\sqrt{6}} + \frac{1082646633625m^2R^2i}{2886218022912\sqrt{6}} + \frac{6254580207p^2R^2i}{2348810240\sqrt{6}}\right. \\
&+ \frac{2084860069m^3R^3i}{3523215360\sqrt{6}} - \frac{46165123m^4R^4i}{495452160\sqrt{6}} - \frac{289m^5R^5i}{8640\sqrt{6}} \\
&\left. - \frac{257m^2p^2R^4i}{1920\sqrt{6}} + \frac{m^6R^6i}{972\sqrt{6}}\right)x^{\frac{9}{2}} \\
&+ \left(\frac{3006381636116734147271}{4842270319348757299200} - \frac{364502713887059m^2R^2}{1979120929996800} + \frac{467950584817p^2R^2}{751619276800}\right. \\
&+ \frac{467950584817m^3R^3}{3382286745600} + \frac{5860496177m^4R^4}{211392921600} - \frac{3p^4R^4}{400} - \frac{230659m^2p^2R^4}{2867200} \\
&\left. - \frac{904777m^5R^5}{38707200} - \frac{m^3p^2R^5}{300} + \frac{7193m^6R^6}{10886400}\right)x^5 \\
&+ \left(\frac{5128449466895961053034137i}{17044791524107625693184 00\sqrt{6}} - \frac{3433560117621558289 3m^2R^2i}{3901243177209692160 0\sqrt{6}}\right. \\
&+ \frac{95701211011123p^2R^2i}{529139970867200\sqrt{6}} + \frac{95701211011123m^3R^3i}{2381129868902400\sqrt{6}} - \frac{796677378877m^4R^4i}{24803436134400\sqrt{6}} \\
&+ \frac{72738463m^2p^2R^4i}{432537600\sqrt{6}} + \frac{7209p^4R^4i}{140800\sqrt{6}} + \frac{13486087m^5R^5i}{216268800\sqrt{6}} + \frac{801m^3p^2R^5i}{35200\sqrt{6}} \\
&\left. + \frac{1391791m^6R^6i}{1094860800\sqrt{6}} - \frac{m^4p^2R^6i}{360\sqrt{6}} - \frac{m^7R^7i}{1620\sqrt{6}}\right)x^{\frac{11}{2}} + \mathcal{O}(x^6)
\end{aligned}
\tag{D.5}
$$

$$
g_{2A}(x) = g_{1A}^*(x) \tag{D.6}
$$

$$
\begin{aligned}
g_{2R} = 1 &+ \frac{297}{32\sqrt{3}}x^{\frac{1}{2}} + \frac{30099}{2048}x + \frac{3037713}{65536\sqrt{3}}x^{\frac{3}{2}} + \frac{300496227}{8388608}x^2 \\
&+ \left(\frac{82087138059}{1342177280\sqrt{3}} - \frac{m^3R^3}{15\sqrt{3}} - \frac{3p^2R^2}{10\sqrt{3}} \right) x^{\frac{5}{2}} \\
&+ \left(\frac{1900704675507}{8589934592} + \frac{m^2R^2}{4} - \frac{79m^3R^3}{480} - \frac{237p^2R^2}{320} \right) x^3 \\
&+ \left(\frac{167653311868227}{19241453486080\sqrt{3}} + \frac{1375m^2R^2}{896\sqrt{3}} - \frac{41311m^3R^3m^3R^3}{71680\sqrt{3}} \right. \\
&\left. + \frac{m^4R^4}{28\sqrt{3}} - \frac{371799p^2R^2}{143360\sqrt{3}} \right) x^{\frac{7}{2}} \\
&+ \left(\frac{-5808890946829751}{4925812092436480} + \frac{210319m^2R^2}{172032} - \frac{9851451p^2R^2}{4587520} \right. \\
&\left. - \frac{3283817m^3R^3}{6881280} + \frac{71m^4R^4}{896} \right) x^4 \\
&+ \left(\frac{426583331303256091}{472877960873902080\sqrt{3}} + \frac{7245295m^2R^2}{16515072\sqrt{3}} - \frac{2005890927p^2R^2}{587202560\sqrt{3}} \right. \\
&\left. - \frac{668630309m^3R^3}{880803840\sqrt{3}} + \frac{15147m^4R^4}{57344\sqrt{3}} - \frac{m^5R^5}{90\sqrt{3}} \right) x^{\frac{9}{2}} \\
&+ \left(\frac{2923303201030147029}{7205759403792793600} - \frac{33990871m^2R^2}{100663296} \right. \\
&\left. - \frac{14673083559p^2R^2}{13421772800} - \frac{4891027853m^3R^3}{20132659200} + \frac{158771m^4R^4}{786432} \right. \\
&\left. + \frac{3p^4R^4}{200} - \frac{7m^5R^5}{320} + \frac{m^3p^2R^5}{150} + \frac{m^6R^6}{1350} \right) x^5 \\
&+ \left(\frac{-76149834528852033691949}{17754991170945443430400\sqrt{3}} + \frac{713645987983m^2R^2}{413390602240\sqrt{3}} \right. \\
&\left. - \frac{98128715759757p^2R^2}{66142496358400\sqrt{3}} - \frac{10903190639973m^3R^3}{33071248179200\sqrt{3}} \right. \\
&\left. + \frac{19205203m^4R^4}{234881024\sqrt{3}} - \frac{3m^2p^2R^4}{40\sqrt{3}} + \frac{4041p^4R^4}{70400\sqrt{3}} \right. \\
&\left. - \frac{5513m^5R^5}{61440\sqrt{3}} + \frac{449m^3p^2R^5}{17600\sqrt{3}} - \frac{751m^6R^6}{158400\sqrt{3}} \right) x^{\frac{11}{2}} + \mathcal{O}(x^6)(x^6)
\end{aligned}
\tag{D.7}
$$

$$
g_{1R}(x) = g_{2R}(e^{2\pi i}x) \tag{D.8}
$$

Appendix E

Some Standard Results in Perturbation Theory

Consider the following equation describing an unperturbed non-degenerate system

$$H^{(0)}\psi_m^{(0)} = E_m^{(0)}\psi_m^{(0)}, \tag{E.1}$$

where the unperturbed eigenfunctions, $\psi_m^{(0)}$ form a complete orthonormal set, i.e. $\left\langle \psi_m^{(0)} | \psi_n^{(0)} \right\rangle = \delta_{mn}$, and the corresponding unperturbed eigenvalues are $E_m^{(0)}$.

Acting on the system with a small perturbation, H', generates a new eigenvalue problem,

$$H\psi_m = E_m\psi_m \tag{E.2}$$

where $H = H^{(0)} + \lambda H'$[1] and ψ_m and E_m are the new eigenfunctions and eigenvalues, respectively. For a small enough perturbation, one can write the eigenfunctions and eigenvalues as a power series,

$$\begin{aligned} \psi_m &= \psi_m^{(0)} + \lambda\psi_m^{(1)} + \lambda^2\psi_m^{(2)} + \cdots \\ E_m &= E_m^{(0)} + \lambda E_m^{(1)} + \lambda^2 E_m^{(2)} + \cdots . \end{aligned} \tag{E.3}$$

Inserting these into Eq. (E.2) one can write the following:

[1] λ has been introduced in the standard way to keep track of the order of perturbation, and is set to 1 at the end.

$$\begin{aligned}
\lambda^0&: \ \left(H^{(0)} - E_m^{(0)}\right)\psi_m^{(0)} = 0 \\
\lambda^1&: \ \left(H^{(0)} - E_m^{(0)}\right)\psi_m^{(1)} = \left(E_m^{(1)} - H'\right)\psi_m^{(0)} \\
\lambda^2&: \ \left(H^{(0)} - E_m^{(0)}\right)\psi_m^{(2)} = \left(E_m^{(1)} - H'\right)\psi_m^{(1)} + E_m^{(2)}\psi_m^{(0)}
\end{aligned} \tag{E.4}$$

The zeroth-order equation just corresponds to the original unperturbed system. Taking the inner product of the first-order equation with $\psi_m^{(0)}$ and using orthonormality one can derive the following well-known equation for the first-order correction to the energy:

$$E_m^{(1)} = \left\langle \psi_m^{(0)} | H' | \psi_m^{(0)} \right\rangle . \tag{E.5}$$

We are also interested in evaluating the first-order correction to the wave function, $\psi_m^{(1)}$. In the standard way we start by writing it in terms of a sum over the unperturbed eigenfunctions,

$$\psi_m^{(1)} = \sum_{n \neq m} c_n^{(1)} \psi_n^{(0)}. \tag{E.6}$$

Inserting this into the first-order equation in Eq. (E.4), taking the inner product with $\psi_k^{(0)}$, and using orthonormality one can show that

$$c_k^{(1)} = \frac{\left\langle \psi_k^{(0)} | H' | \psi_m^{(0)} \right\rangle}{E_m^{(0)} - E_k^{(0)}} \tag{E.7}$$

which gives the first-order correction to the wave function as

$$\psi_m^{(1)} = \sum_{n \neq m} \frac{\left\langle \psi_n^{(0)} | H' | \psi_m^{(0)} \right\rangle}{E_m^{(0)} - E_n^{(0)}} \psi_n^{(0)}. \tag{E.8}$$

This can be written using a more compact notation as

$$\psi_0^{(1)} = \sum_{n \neq 0} |n\rangle \frac{\langle n | H' | 0 \rangle}{E_0^{(0)} - E_n^{(0)}}. \tag{E.9}$$

Finally, to determine the second-order correction to the energy, $E_m^{(2)}$, one starts by taking the inner product of the second-order equation in Eq. (E.4) with $\psi_m^{(0)}$, and after applying orthonormality constraints we get

$$\begin{aligned} E_m^{(2)} &= \left\langle \psi_m^{(0)} | H' | \psi_m^{(1)} \right\rangle \\ &= \sum_{n \neq m} c_n^{(1)} \left\langle \psi_m^{(0)} | H' | \psi_n^{(0)} \right\rangle \\ &= \sum_{n \neq m} \frac{\left\langle \psi_m^{(0)} | H' | \psi_n^{(0)} \right\rangle \left\langle \psi_n^{(0)} | H' | \psi_m^{(0)} \right\rangle}{E_m^{(0)} - E_n^{(0)}}, \end{aligned} \tag{E.10}$$

which again can be written in a more compact form given by

$$E_0^{(2)} = \sum_{n \neq 0} \frac{\langle 0 | H' | n \rangle \langle n | H' | 0 \rangle}{E_0^{(0)} - E_n^{(0)}}. \tag{E.11}$$